

Design, Synthesis and Characterization of Organic π -
Conjugated Compounds Incorporating Group 14 and 15 Heavy
Elements

(14 および 15 族重元素を含む有機 π 共役化合物の設計、合成
および特性)

September 2024

WANG CONGHUAN

Hiroshima University

Contents

General Introduction	1
Chapter 1 Group 15 Element (As, Sb, Bi)-substituted Bibenzofurans with Noncovalent Conformational Locks for Enhanced Planarity	14
Chapter 2 Synthesis of Unsymmetrically Condensed Benzo- and Thienotriazolgermoles	46
Chapter 3 Preparation of Dithieno[3,2- <i>b</i> :4,5- <i>c'</i>]germole and Its Application as a Donor Unit in Conjugated D-A Oligomers.....	64
Conclusions.....	80
List of Publications	83
Acknowledgements.....	85

Non-covalent bonds can be categorized into the following groups based on their formation mechanisms and the types of interactions involved: Hydrogen bonds are weak charge-charge interactions between hydrogen atoms and interacting partners binding molecules, which include conventional hydrogen bonding ($X-H\cdots X$, $X = F, O, N$) and unconventional hydrogen bonding ($C_{SP^2}-H\cdots O$, $C_{SP^2}-H\cdots N$, $C-H\cdots\pi$, $O-H\cdots F-C$ and $N-H\cdots F-C$). It can regulate the orientation and packing mode of molecules and affect the optoelectronic properties of materials and their crystal structure. For example, in the recently reported two model compounds, the coplanarity of the main chain is induced by the presence of 6-membered hydrogen bond rings. The absorption/emission spectrum shown a smaller band gap and the enhancement of thermal stability which provide further evidence supporting the advantageous impact of hydrogen bonding. (Figure 2) [7] In organic solar cells, the molecular arrangement of photoelectric conversion materials is optimized by introducing the intermolecular interaction formed by hydrogen bonds to improve the efficiency of light absorption and electron transport. [8]

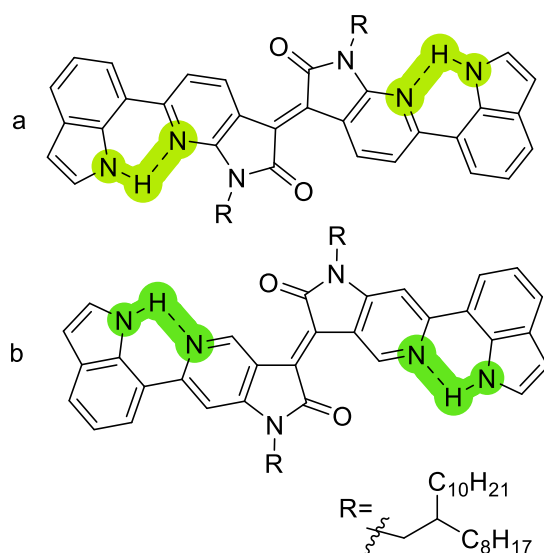


Figure 2. Schematic diagram of hydrogen bonded compounds.

π - π Stacking is a non-covalent π -electron cloud interaction between π -conjugated systems, which can regulate the electron energy level and molecule

packing mode and affect this carrier transport properties. [9] For example, by modifying the configuration and distance of side chains in π -conjugated molecules, organic solar cells achieve effective carrier transfer to improve the device performance. [10] π - π Stacking generally based on London dispersion force, dipole-dipole interaction and van der Waals attraction. Organic optoelectronic materials often exhibit numerous aromatic rings and conjugated structures, resulting in the generation of intermolecular accumulations or aggregations. Such aggregation can have a substantial influence on the material's charge transport performance, luminous efficiency, and stability. The molecular arrangement, morphology and photoelectric properties of materials can be controlled by adjusting the strength and scope of nonbonding. [11] In organic solar cells, OLEDs and other optoelectronic devices, noncovalent interactions can affect the formation of interfaces and the regulation of energy levels. For example, in OLEDs, through the interaction of van der Waals interactions between the organic light-emitting layer and the electron transport layer, the carrier injection, transfer and recombination processes can be optimized, thereby improving the performance and stability of the device. [12] The distinctive characteristics of noncovalent interactions offer a wide range of possibilities for utilization in various research fields, facilitating the creation of functional materials and the advancement of new technologies. It is essential to further expand the scope of non-covalent interactions. [13]

Introducing elements to construct new π -conjugated systems is an important research direction in the field of organic electronic materials. Incorporating main group elements in π -conjugated structure is an advanced method for modifying the essential traits of the primary conjugated π -systems, resulting in appealing optoelectronic features. [14, 15] A successful approach includes incorporating heteroatoms directly into the π -skeleton, with a focus on those belonging to groups 13–16.

Introduction of boron: The presence of the vacant p orbital in boron facilitates the introduction of additional electron deficiencies or holes into π -conjugated systems,

thereby modifying the band structure of the material. (Figure 3)

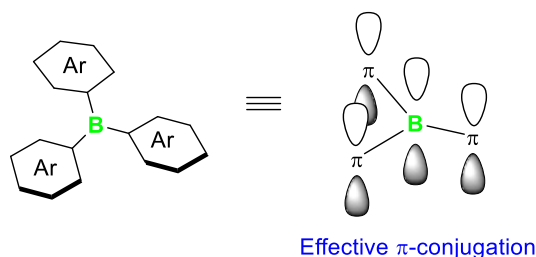


Figure 3. Schematic diagram of triarylborane and orbital interaction.

Boron (B) is commonly used as heteroatom doping to regulate the electronic structure and energy level alignment of materials by changing electron density and delocalizing electrons, improving carrier mobility and device performance. For example, incorporating a boron bridge into the thiophene-thiazole molecule and linking it to acceptor groups can lead to A- π -A molecules with the lowered LUMO energy level and enhanced environmental stability. (Figure 4) By incorporating these substances into the active layer of organic thin-film transistor devices, there is a possibility to improve the electrons mobility. [16]

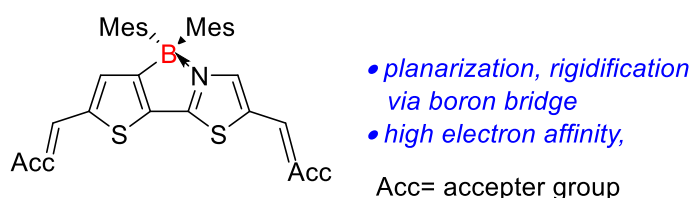


Figure 4. Structure of boron doped compounds.

Introduction of nitrogen: A nitrogen atom with three coordinated bonds possesses a single lone pair electron, which naturally complements a boron atom also with three coordinated bonds (and an empty p orbital). As a result, compounds containing this structural feature are of high significance. (Figure 5)

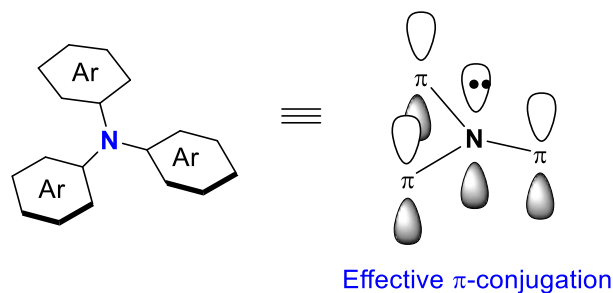


Figure 5. Schematic diagram of triarylamine and orbital interaction.

Nitrogen (N) doping can introduce additional electrons to affect the material's band structure and charge transport performance. This is often employed to enhance the electrical conductance and light absorption characteristics of organic semiconductors, giving them a wider range of potential applications in optoelectronic devices. For instance, the existence of a nitrogen atom in the π -electron increases by strategically positioning negative N atom with π -electron. The increases overlap of molecular orbitals between neighboring molecules, which effectively reduces molecular movement, resulting in improved atmospheric and structural stability, as well as enhanced capability for charge transport between the molecules. These n-type organic semiconductor compounds have made significant progress in advanced organic-based materials. (Figure 6) [17]

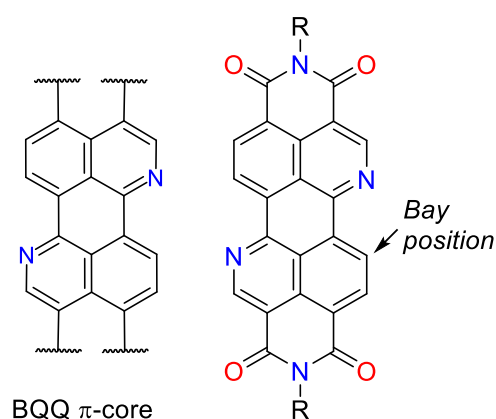


Figure 6. Examples of nitrogen-dope π -electron frameworks for n-type semiconductors.

Despite some commonalities, phosphorus-containing π -conjugated compounds exhibit distinctive structural and electronic characteristics when compared to nitrogen counterparts. The π system containing phosphorus typically assumes a fixed bowl or spiral structure, depending on the arrangement of the three aryl groups. This contrasts with nitrogen-centered analogues, which contain complete or quasi-planarization structures. (Figure 7) Due to its local electron lone pair, the phosphorus trivalent atom has electron donor property. In contrast, the phosphorus pentavalent group exhibits electron-accepting properties because of its heightened electronegativity, making it a crucial and practical building block in functional organic materials.

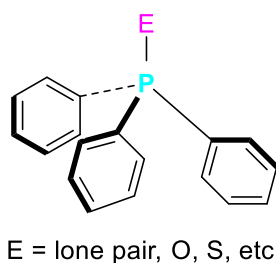


Figure 7. Schematic diagram of triphenylphosphine.

The introduction of sulfur and selenium can alter the optoelectronic properties of the material by forming thioconjugated or selenoconjugated bonds with carbon. For example, sulfides and selenides can be used to regulate the band structure to improve carrier mobility and photoelectric conversion efficiency. This presents possibilities for improving the photovoltaic efficiency of materials containing selenium. In addition, the substantial selenium atom potentially triggers significant spin-orbit coupling, facilitating the intersystem crossing from the singlet excited state (S1) to the triplet states (T1). (Figure 8) [18]

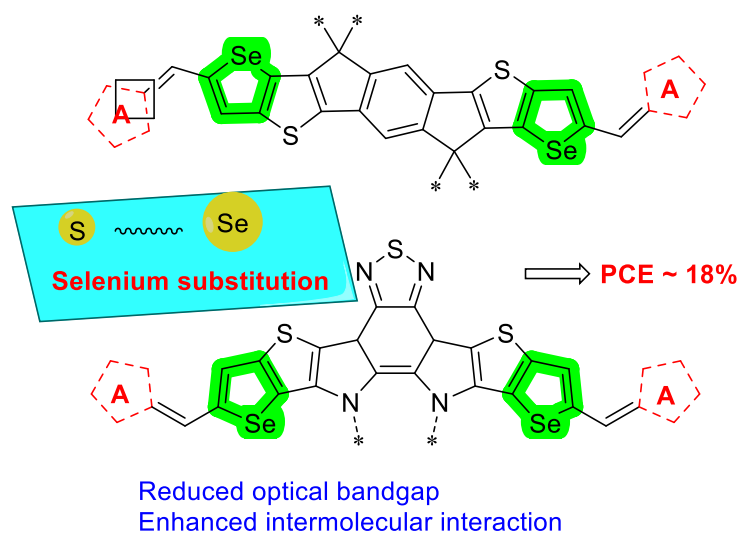


Figure 8. Schematic diagram of the selenium application.

Doping of other main group elements: The incorporation of light element centers into the extended π -conjugated compounds has facilitated the development of structurally new molecules and macromolecules. Doping of π -electron systems with heavier elements can also regulate the electronic and optical characteristics of materials for the development of excellent organic semiconductors and optoelectronic materials. [19]

31 Ga	32 Ge	33 As	34 Se			2 He
49 In	50 Sn	51 Sb	52 Te			10 Ne
	82 Pb	83 Bi				

Figure 9. Schematic diagram of the other main group elements.

The introduction of non-traditional elements: Boron- and nitrogen--embedded compounds have special electronic structures and chemical properties, and by

introducing these non-traditional elements to build new conjugated systems, the application field and performance characteristics of materials can be expanded. (Figure 10) [20]

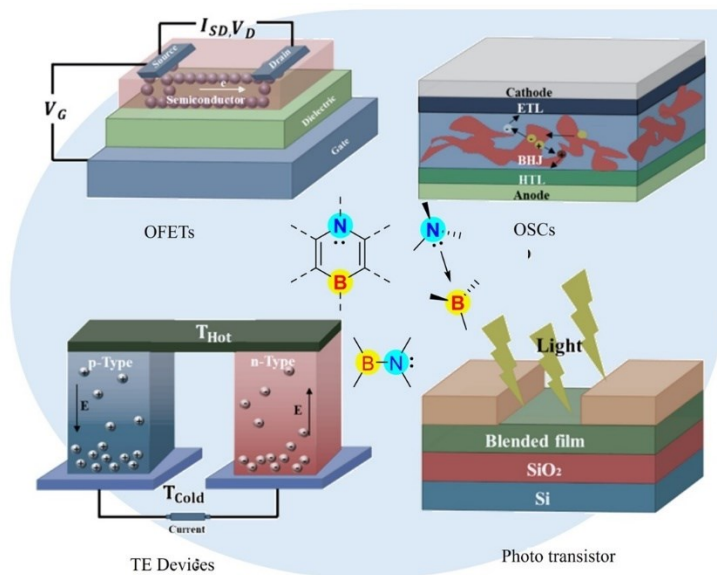


Figure 10. Schematic diagram of the boron- and nitrogen-embedded compounds and the application.

Triazoles are aromatic ring systems with a five-membered structure that consists of three nitrogen atoms in sequence and two double bonds. Apart from their distinctive structural characteristics, such as high dipole moments and molecular rigidity, triazoles have exceptional accessibility and ease of modification. Indeed, they have been extensively employed in creating functional materials for a wide range of uses. (Figure 11) [21]

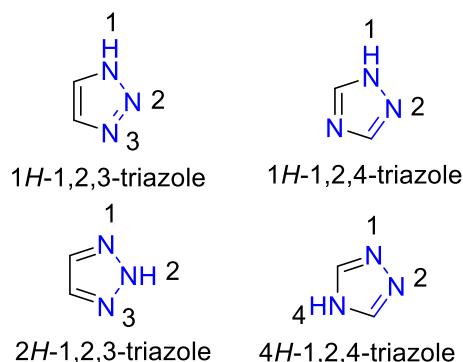


Figure 11. Schematic diagram of triazoles.

To attain outstanding photovoltaic performance, it is crucial to accurately fine-tune the inherent properties of conjugated compounds, including their absorption spectra, molecular energies, hole and electron mobility, and morphologies. Designing molecular structures and synthesizing Group 14-containing building blocks are efficient approach for constructing innovative π -conjugated structures. Many researchers have attempted to synthesize heavier Group 14 element-containing materials to delve deeper into their aromaticity and seek potentially advantageous optoelectronic properties. Group 14 metalloles, such as siloles and germoles are considered valuable components for the construction of functional compounds due to that the silane moiety interacts with the butadiene moiety to give rise to low-lying LUMO energies and relatively narrow band gaps. Dithienosilole serves as a typical silicon-based unit used in the creation of conjugated organic materials. [22, 23] However, most research efforts have been focused on the symmetrical condensated of dithienosiloles, with limited exploration into unsymmetrical dithienosiloles. (Figure 12) Wang and coworkers have successfully synthesized unsymmetrical dithienosiloles derivatives [24] and utilized them as monomers to prepare conjugated polymers. This unsymmetrical unit allows for the incorporation of one thiophene ring into the conjugated oligomer and polymer system, while introducing an additional functional group (R') on the other ring to finely adjust the electronic state of the dithienosiloles. (Figure 12)

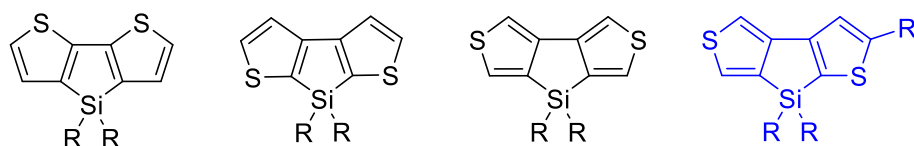


Figure 12. Structures of dithienosiloles reported.

In Chapter 1, due to the broad potential applications of extended-conjugated organic compounds in optoelectronic materials, increasing the flatness of the π -electron system can significantly raise the level of conjugation. In this scenario,

intramolecular non-covalent interactions provide a convenient method for enhancing the molecular planarity of organic semiconductors through conformational locks in their design. This approach effectively decreases the band gap, as evidenced by phospho-substituted bisbenzofuran derivatives (BFP) featuring non-covalent P \cdots O interactions. Additionally, inclusion of bulkier elements may lead to stronger noncovalent interactions. Consequently, bibenzofurans and bibenzothiophenes substituted with bismuth, antimony, and arsine have been synthesized by the author. An X-ray diffraction analysis of a single crystal indicated that Bi \cdots O, Sb \cdots O, and As \cdots O substances were involved in attractive noncovalent interactions that contributed to self-planarization and rigidification of the crystal. QTAIM analysis identified BCPs between Bi \cdots O, Sb \cdots O, and As \cdots O, corresponding to van der Waals interactions as revealed by the interaction region indicator. (Figure 13)

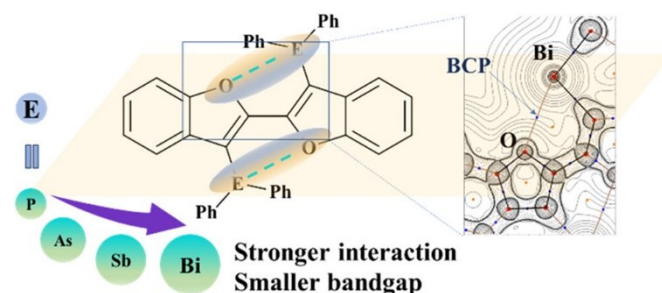


Figure 13. Schematic diagram of the structures, described in Chapter 1.

In Chapter 2, to develop a new building block of group 14 metalloles, A triazolgermole ring condensed with a benzene or thiophene ring was synthesized. The thienotriazolgermole was subjected to bromination to produce the corresponding bromide, which was then transformed using the palladium-catalyzed Stille coupling reaction to yield thienotriazolegermole substituted with triphenylamine, resulting in an enhanced extension of conjugation. A combination of optical measurements, electrochemical calculations, and density functional theory are used to examine the electronic states of these triazolgermole derivatives. In photoluminescence measurements, thienotriazolegermole substituted with triphenylamine demonstrated

clear solvatochromic properties. This indicates intramolecular charge transfer. This underscores the utility of the triazologermele unit as an acceptor in donor–acceptor compounds. Furthermore, the author explored potential applications of thienotriazologermele substituted with triphenylamine as a sensing material. (Figure 14)

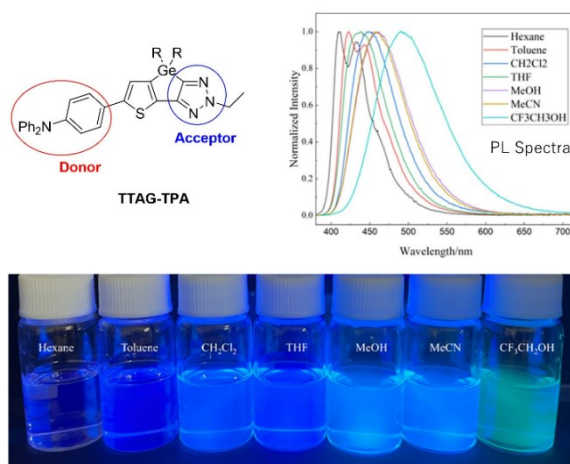


Figure 14. Schematic diagram of the structures, described in Chapter 2.

In Chapter 3, dithieno[3,2-*b*:4,5-*c'*]germole was prepared as a new unsymmetrically condensed germole. Benzo[4,5]thieno[2,3-*c*]germole was also prepared as the benzene-condensed analogue. The optical and electrochemical measurements were employed to analyze the electronic states and properties of these germoles, which are unsymmetrically condensed. This analysis was further supported by quantum chemical calculations on simplified model compounds. Stille cross coupling reactions of bromodithieno[3,2-*b*:4,5-*c'*]germole with di(stannylthienyl)- and di(stannylthiazolyl)benzothiadiazole provided conjugated donor-acceptor oligomers, which exhibited clear solvatochromic behaviors with respect to the photoluminescence spectra, indicating potential applications of the dithieno[3,2-*b*:4,5-*c'*]germole unit as an electron donor of donor-acceptor systems.

References

- [1] Khasbaatar, A.; Xu, Z.; Lee, J.; Campillo-Alvarado, G.; Hwang, C.; Onusaitis, B. *Chem. Rev.* **2023**, *123*, 8395-487.
- [2] Li, H.; Bredas, J. *Natl. Sci. Rev.* **2021**, *8*, nwaa167.
- [3] Li, G.; Matsuno, T.; Han, Y.; Wu, S.; Zou, Y.; Jiang, Q. *Angew. Chem. Int. Ed. Engl.* **2021**, *60*, 10326-10333.
- [4] Mateo-Alonso, A. *Chem. Mater.* **2023**, *35*, 1467-1469.
- [5] Stolte, M.; Schembri, T.; Süß, J.; Schmidt, D.; Krause, A.; Vysotsky, M.; *Chem. Mater.* **2020**, *32*, 6222-6236.
- [6] Zhang, G.; Lin, F.; Qi, F.; Heumuller, T.; Distler, A.; Egelhaaf, H. *Chem. Rev.* **2022**, *122*, 14180-14274.
- [7] Mu, A.; Kim, Y.; Miranda, O.; Vazquez, M.; Strzalka, M.; Xu, J. *ACS Mater. Lett.* **2022**, *4*, 270-278.
- [8] Li, M.; Sun, R.; Chang, J.; Dong, J.; Tian, Q.; Wang, H. *Nat. Commun.* **2023**, *14*, 573.
- [9] Singh, N. J.; Min, S. K.; Kim, D. Y.; Kim, K. S. *J. Chem. Theory. Comput.* **2009**, *5*, 515-529.
- [10] Luo, Z.; Gao, Y.; Lai, H.; Li, Y.; Wu, Z.; Chen, Z. *Energy Environ. Sci.* **2022**, *15*, 4601-4611.
- [11] Jamadar, A.; Singh, A. K.; Roy, L.; Das, A. *J. Mater. Chem. C* **2021**, *9*, 11893-11904.
- [12] Zhao, T.; Jiang, S.; Wang, Y.; Hu, J.; Lin, F. L.; Meng, L. *ACS Appl. Mater. Interfaces* **2023**, *15*, 30543-30552.
- [13] Chen, J.; Peng, Q.; Peng, X.; Zhang, H.; Zeng, H. *Chem. Rev.* **2022**, *122*, 14594-14678.
- [14] Scaccabarozzi, A. D.; Basu, A.; Anies, F.; Liu, J.; Zapata-Arteaga, O.; Warren, R. *Chem. Rev.* **2022**, *122*, 4420-4492.
- [15] Hirai, M.; Tanaka, N.; Sakai, M.; Yamaguchi, S. *Chem. Rev.* **2019**, *119*, 8291-8331.
- [16] Hecht, R.; Kade, J.; Schmidt, D.; Nowak-Krol, A. *Chem. Eur. J.* **2017**, *23*,

11620-11628.

[17] Okamoto, T.; Kumagai, S.; Fukuzaki, E.; Ishii, H.; Watanabe, G.; Niitsu, N.; Takeya, J. *Sci. adv.* **2020**, *6*, eaaz0632.

[18] Fan, B.; Lin, F.; Wu, X.; Zhu, Z.; Jen, A. K. *Acc. Chem. Res.* **2021**, *54*, 3906-3916.

[19] Parke, S. M.; Boone, M. P.; Rivard, E. *Chem. Commun.* **2016**, *52*, 9485-9505.

[20] Chen, C.; Zhang, Y.; Wang, X. Y.; Wang, J. Y.; Pei, J. *Chem. Mater.* **2023**, *35*, 10277-10294.

[21] Luo, Z.; Chen, X.; Hu, Y.; Chen, X.; Lin, W.; Wu, X. *Angew. Chem. Int.* **2023**, *62*, e202304875.

[22] Ohshita, J. *Macromol. Chem. Phys.* **2009**, *210*, 1360-1370.

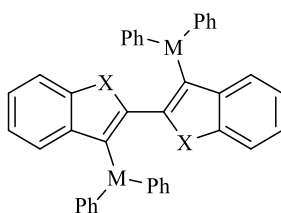
[23] Cai, Y.; Qin, A.; Tang, B. Z. *J. Mater. Chem. C* **2017**, *5*, 7375-7389.

[24] Liu, L.; Song, J.; Lu, H.; Wang, H.; Bo, Z. *Polym.* **2016**, *7*, 319-329.

Chapter 1 Group 15 Element (As, Sb, Bi)-substituted Bibenzofurans with Noncovalent Conformational Locks for Enhanced Planarity

Introduction

Organic compounds with extended π -conjugation are of current importance owing to their potential applications as optoelectronic materials. [1] The extent of conjugation is readily enhanced by increasing the planarity of the π -electron system. However, the high planarity of π -conjugated compounds often causes solubility problems. Intramolecular noncovalent interactions have been widely studied as fluxional conformational locks that can improve molecular planarity in the solid state while providing sufficient solubility for the processing of compounds, given moderate molecular flexibility in solution. For example, several organic semiconductors containing various intramolecular noncovalent interactions, such as $S\cdots O$, [2] $S\cdots N$, [3] and $X\cdots S$ [4] ($X = \text{halogen}$) interactions, have been designed for applications in the areas of organic field-effect transistors, [5] organic light-emitting diodes, [6] and organic solar cells, [7] showing excellent carrier mobility and good photovoltaic performance. In addition to the intramolecular interactions that enhance molecular planarity, intermolecular noncovalent interactions may also be formed, which improve molecular packing in the solid state through π - π interactions and provide semiconductors with excellent charge transport properties. Noncovalent interactions



BFP ($X = O, M = P$) BTP ($X = S, M = P$)
BFBi ($X = O, M = Bi$) BTBi ($X = S, M = Bi$)
BFSb ($X = O, M = Sb$) BTSb ($X = S, M = Sb$)
BFAs ($X = O, M = As$)

Chart 1.1. Structures of Group 15 element-substituted bibenzofurans and bibenzothiophenes

are also expected to introduce planar conjugated units without additional synthetic ring-bridging or fusion processes. In this context, the author envisioned that the proper incorporation of weak interactions with appropriate choice of elements will lead to a new design of conjugated optoelectronic materials.

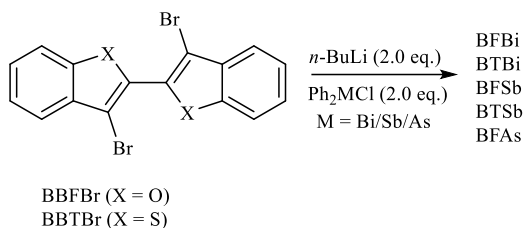
Interactions between electropositive thiophene sulfur and electronegative carbonyl oxygen atoms, or other heteroatoms, have been reported. Zhang and coworkers recently reported the preparation of bis(diphenylphosphino)bibenzofuran (BFP: Chart 1.1), which exhibited noncovalent P \cdots O interactions in the solid (crystalline) state. [8] However, no P \cdots S interaction was observed in the bithiophene congener BTP, suggesting that tuning of electronic states and interactions is possible when the conjugated system is switched from thiophene to furan. In this Chapter, to explore further the scope of Group 15 substituents for the introduction of noncovalent interactions, the author prepared bibenzofurans and bibenzothiophenes bearing bismuth and antimony, i.e., heavier Group 15 substituents. Bismuth is the heaviest abundant stable element with low toxicity. The heavy-atom effects of bismuth and antimony are expected to endow the compounds with phosphorescence properties by enhancing intersystem crossing. [9-12] Their crystal structures were determined by X-ray diffraction studies, revealing the formation of noncovalent Bi \cdots O and Sb \cdots O interactions. The observed optical and electrochemical properties were also in agreement with the enhanced conjugation arising from the noncovalent interactions. Arsine-substituted bibenzofuran was also found to show noncovalent interactions. These interactions were evaluated by DFT calculations and topological analysis of the electron density distribution (QTAIM analysis).

Result and discussion

Synthesis

Bismuth- and antimony-substituted bibenzofurans and bibenzothiophenes (BFBi, BTBi, BFSb, and BTSb) were prepared, as shown in Scheme 1.1. The low yields of these compounds are due to difficult purification by column chromatography and slow decomposition during column chromatography. Indeed, unsubstituted

bibenzofuran and bibenzothiophene were found to be formed together with many unidentified compounds in the case of BFSb and BTSb. Arsenic-substituted bibenzofuran BFAs was also synthesized in a similar fashion.



Scheme 1.1. Synthesis of BFBi, BFSb, BTBi, BTSb, and BFAs.

Single-crystal X-ray diffraction study

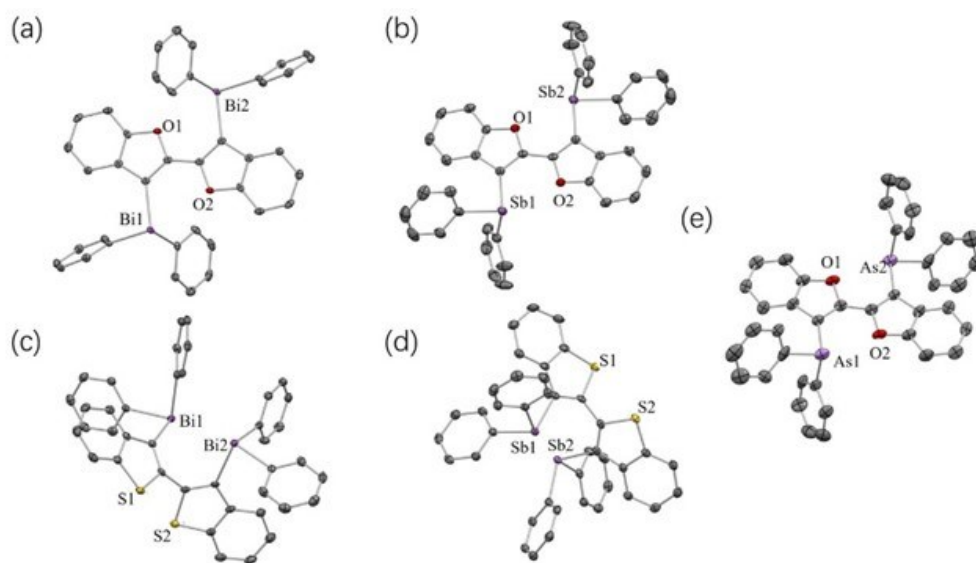


Figure 1.1. ORTEP of (a) BFBi, (b) BFSb, (c) BTBi, (d) BTSb, and (e) BFAs with thermal ellipsoids at 50% probability level. Hydrogen atoms are omitted for clarity.

Single crystals of BFBi, BTBi, BFSb, BTSb, and BFAs were obtained with good quality suitable for X-ray diffraction analysis were grown in a dichloromethane/ether mixed solvent at room temperature. ORTEP and crystallographic data are presented in Figure 1.1 and Table 1.10, respectively. The crystal structures confirmed the presence

of pyramidal Bi(III), Sb(III), and As(III) centers. In BFBi, the bibenzofuran core adopted a highly coplanar structure with an anti-configuration with respect to the central furan–furan C–C bond (torsion angle (O1–C–C–O2) = 180.0 (2)°), with the benzofuran groups oriented in such a way that the oxygen atoms were directed toward the bismuth atoms (Figure 1.1a). BFSb and BFAs showed similar planarity, as shown in Figures 1.1b and 1.1e. These observations were consistent with BFBi and the previously reported structure of BFP. [8] In marked contrast, the benzothiophene planes were twisted with torsion angles of 52.88(2)° and 52.56(2)° in BTBi and BTSb, respectively (Figures 1.1c and 1.1d), similar to BTP (torsion angle: 106°). [8] The intramolecular Bi···O, Sb···O, and As···O distances were 3.190(2) Å, 3.104(1) Å, and 3.003(8) Å, in BFBi, BFSb, and BFAs, respectively, which were shorter than the sums of the van der Waals radii of the respective atoms (Bi···O: 3.59 Å, Sb···O: 3.58 Å, As···O: 3.37 Å) by approximately 11%, 13%, and 11%, respectively, [13-14] suggesting that these noncovalent interactions contribute to the planarization and rigidification of the π -conjugated systems. BFP has also been reported to show a P···O distance that is shorter than the sum of the van der Waals radii of phosphorus and oxygen atoms by 9%. The central C–C bond distances (1.437(6) Å in BFBi and 1.440(4) Å in BFSb) were very close to that of BFP (1.434 Å), reported previously. [8] These C–C bond distances were shorter than those of BTBi (1.464(3) Å) and BTSb (1.473(3) Å), possibly owing to the noncovalent Bi···O and Sb···O interactions. BFAs showed a similar central C–C bond distance (1.454(2) Å) to those of BFBi and BFSb. However, the central C–C bonds of the substituted bibenzofurans (M = Bi, Sb, and As) are slightly longer than that of unsubstituted bibenzofuran (1.434 Å), reported previously. [15] This may be due to the steric repulsion concerning the sterically large Group 15 substituents, offsetting the M···O noncovalent interactions. The molecular packing of BFBi indicates intermolecular short contacts between the furan ring and the bismuth atom with Bi···C and Bi···O distances of 3.573(3) Å, 3.662(3) Å, and 3.339(2) Å, which are slightly shorter than the corresponding sums of the van der Waals radii (Figure 1.2).

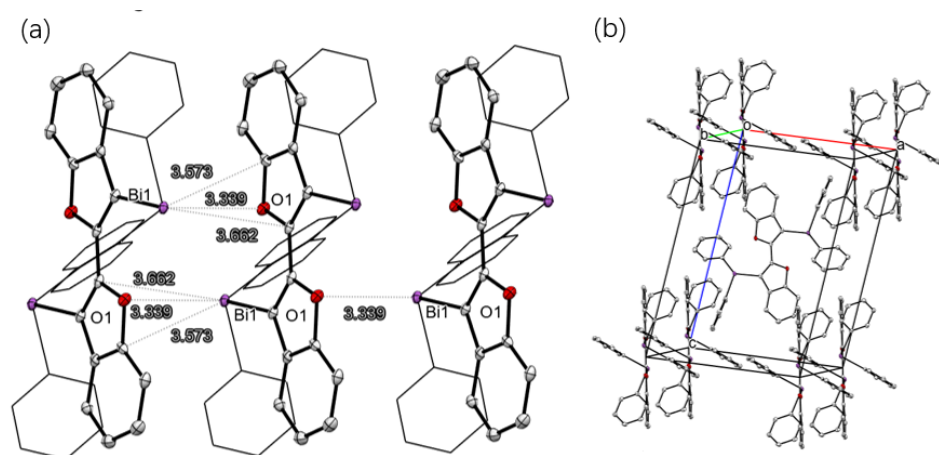


Figure 1.2. ORTEP drawing of BFBi with the thermal ellipsoids at 50% probability level. View of the crystallographic structure of BFBi packing structure.

Optoelectronic characterization

Table 1.1. Optical and electrochemical properties of BFBi, BFSb, BTBi, BTSb, BFAs, and Bibenzofuran.

Compound	UV abs. $\lambda_{\text{max}}^{\text{a}}/\text{nm}$ ($\epsilon/\text{L}(\text{mol cm})$)	PL $\lambda_{\text{max}}^{\text{a,b}}/\text{nm}$ (Φ_{f})		Phos. $\lambda_{\text{max}}^{\text{a}}/\text{nm}$	HOMO ^c /eV	LUMO ^d /eV
		in CH_2Cl_2	as solid			
BFBi	290, 328, 344, 363 (47800)	372, 392, 415 (-) ^e	407, 432, 573, 629 (0.1)	559, 610	-5.55	-2.22
BFSb	280, 334, 346, 364 (33700)	377, 398, 424 (-) ^e	460 (-) ^e	561, 610	-5.52	-2.25
BTBi	280, 296, 306 (32300)	362, 382, 408 (-) ^e	- ^e	441	-5.74	-2.05
BTSb	280, 298, 306 (18600)	359, 381, 402 (-) ^e	- ^e	442	-5.58	-2.08
BFAs	333 (12927)	384, 405 (-) ^e	414, 438 (-) ^e	- ^e	-5.71	-2.48
Bibenzofuran	323, 340 (55600)	362, 383 (-) ^f	408, 429 (-) ^f	- ^f	-5.74	-2.17

^a In CH_2Cl_2 at room temperature. ^b Excited at the absorption maximum. ^c Derived from CV anodic onset potential. ^d $E(\text{LUMO}) = E(\text{HOMO}) + E_{\text{g}}$. ^e Not observed or Φ_{f} too low to determine. ^f Not measured.

The electrochemical properties of BFBi, BFSb, BTBi, BTSb, and BFAs were evaluated by cyclic voltammetry (CV) in acetonitrile, as shown in Table 1.1 and Figure 1.3. From the onset potentials, HOMO energy levels were estimated to be -5.55 eV for BFBi, -5.52 eV for BFSb, -5.74 eV for BTBi and -5.58 eV for BTSb, which were higher than those of unsubstituted bibenzofuran (-5.74 eV) and bibenzothiophene (-6.15 eV). This was probably due to the electron donating character of antimony and bismuth as well as enhanced conjugation, which raised the HOMO energy levels. BFAs exhibited the HOMO energy level (-5.71 eV) deeper than BFBi and BFSb, but shallower than unsubstituted bibenzofuran.

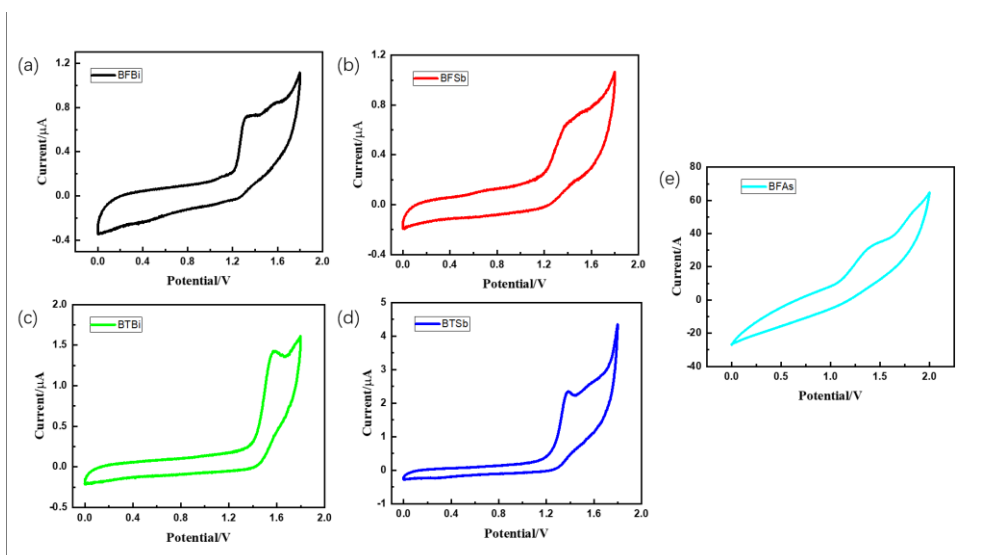


Figure 1.3 Cyclic voltammograms of (a) BFBi, (b) BFSb, (c) BTBi, (d) BTSb, (e) BFAs.

The optical properties of BFBi, BFSb, BTBi, BTSb, BFAs, and bibenzofuran are summarized in Table 1.1. The maximum absorptions (λ_{\max}) of substituted bibenzofurans were red-shifted than that of unsubstituted bibenzofuran. Those of BFBi and BTSb in CH_2Cl_2 were observed at 344 and 346 nm, respectively, which were red-shifted by approximately 25 nm relative to the λ_{\max} of BFP (319 nm) reported previously, [8] indicating that the effective conjugation is extended in solution when P is replaced by Bi or Sb. The absorption band of BFAs at 333 nm was

slightly red-shifted relative to that of BFP. On the other hand, BTBi and BTSb exhibited absorption bands with maxima at 290 and 280 nm, respectively (Figure 1.4). These observations are likely attributed to the enhanced noncovalent interactions serving as conformational locks to extend the lengths of effective conjugation with increasing planarity in the order of $\text{Bi}\cdots\text{S}/\text{Sb}\cdots\text{S} < \text{P}\cdots\text{O} < \text{As}\cdots\text{O} < \text{Bi}\cdots\text{O}/\text{Sb}\cdots\text{O}$. The absorption bands of BFAs, BTBi, and BTSb were broad, in contrast to those of BFBi and BFSb that showed vibrational splitting. It seems likely that this indicates the higher fluxionality, and hence, the weaker noncovalent interactions, in BFAs, BTBi, and BTSb.

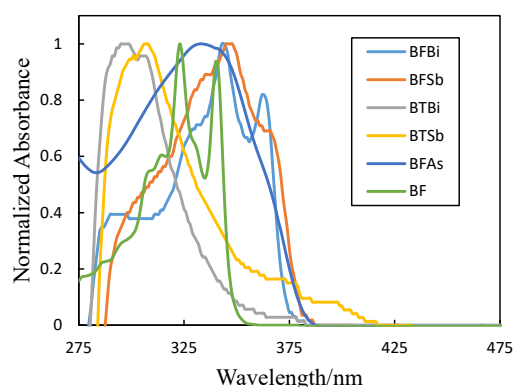


Figure 1.4. UV-vis absorption spectra of BFBi-, BFSb-, BTBi-, BTSb-, BFAs-, and BF (bibenzofuran) in dichloromethane at a concentration of 10 μM .

Although some other factors such as intramolecular donor-acceptor (D-A) interactions may also affect the absorption band broadening the shapes, these compounds showed no significant changes of the absorption and PL spectra depending on the solvent polarity (Figure 1.5). This indicates the lack of strong D-A interactions in these compounds. Bismuth-containing bibenzofuran BFBi can form a clear thin solid film on a quartz plate by spin-coating, whose absorption maxima were red-shifted from those in solution by 5-7 nm, indicating some intermolecular interactions in the film state (Figure 1.6).

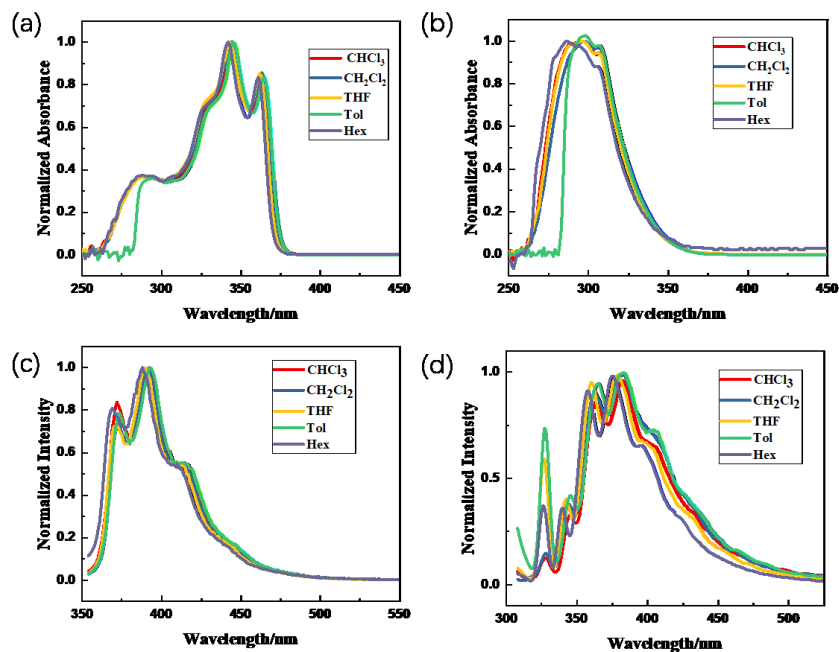


Figure 1.5. UV-vis absorption spectra and Normalized fluorescence spectra of (a)(c) for BFBi and (b)(d) for BTBi in various solvents at a concentration of 10 μ M. (Excited at the absorption maximum)

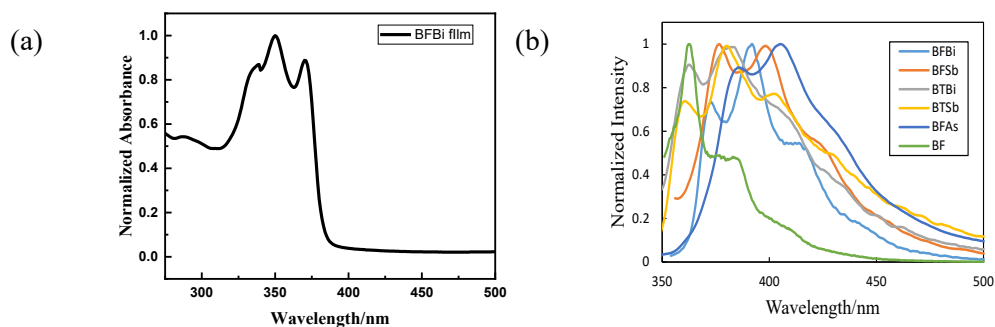


Figure 1.6. (a). UV-vis absorption spectra of the BFBi film after spin coating at 1000 rpm for 45s. (b). PL spectra of BFBi-, BFSb, BTBi, BTSb, BFAs, and BF (bibenzofuran) in dichloromethane at a concentration of 10 μ M.

The bismuth-, antimony-, and arsenic-substituted compounds examined in the present study exhibited photoluminescence (PL) bands centered at 400–425 nm in

solution (Figure 1.6b), which were comparable or slightly red-shifted relative to the PL λ_{max} of BFP (408 nm). [8] BFBi and BFSb, but not BTBi and BTSb, in the solid states emitted PL when excited at the absorption maximum (Figures 1.7). BTBi showed PL from the solid likely due to phosphorescence when irradiated at 365 nm. Although some thiophene derivatives are known to show low fluorescence quantum yields, possibly because of the sulfur heavy atom effects, [16] the reason for non-emissive properties of BTBi and BTSb in the solid state are not clearly understood yet. Similarly, BTP emitted no PL in solution or in the solid state. [8]

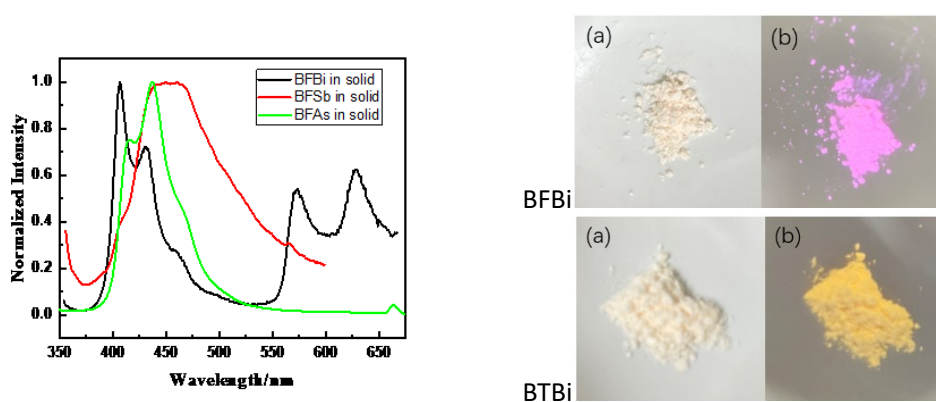


Figure 1.7. PL spectra of BFBi, BFSb, and BFAs as solid (left), and Photos of BFBi and BTBi solid in air at room temperature: (a)under room light, (b)under UV at 365nm (right).

As shown in Figure 1.8, BFBi, BFSb, BTBi and BTSb showed phosphorescence in CH_2Cl_2 . The sharp, largely red-shifted phosphorescence bands of BFBi and BFSb are likely due to the noncovalent $\text{Bi}\cdots\text{O}$ and $\text{Sb}\cdots\text{O}$ interactions serving as conformational locks to enhance both conjugation and molecular rigidity in these molecules. Interestingly, BFSb in the solid state showed a broad PL band centered at 442 nm (Figure 1.7), which was similar to the phosphorescence bands of BTBi and BTSb in solution (Figure 1.8). However, this peak was too weak to investigate its origin in detail. BFAs did not exhibit phosphorescence.

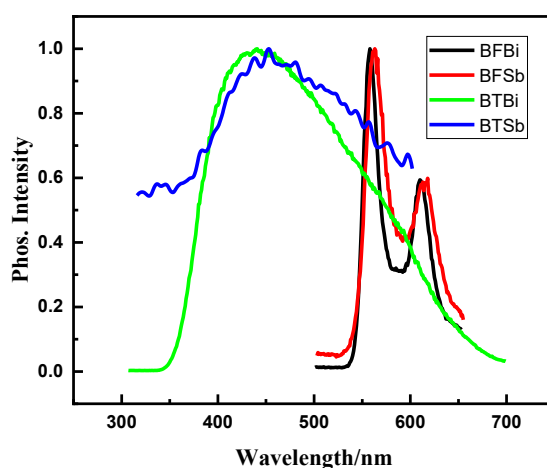


Figure 1.8. Phosphorescence spectra of BFBi, BFSb, BTBi and BTSb in dichloromethane at a concentration of 10 μM .

DFT calculations

The crystallographic data supported the formation of intramolecular noncovalent $\text{Bi}\cdots\text{O}$, $\text{Sb}\cdots\text{O}$, and $\text{As}\cdots\text{O}$ interactions in the crystal structures, as described above. To evaluate these weak interactions, DFT calculations were performed. Gas phase geometries were optimized using Gaussian 16 program packing based on the BP86 [17-18] functional in conjunction with cc-pVTZ-PP pseudopotential (Bi, Sb, and As)¹⁹⁻²³ and 6-31G(d) (other elements) basis sets. The Multiwfn 3.8 [24] program was used for the topological analysis of the electron density with QTAIM, [25] the electron localized function (ELF), [26-27] and the interaction region indicator (IRI). [28] Visualization of chemical structures for the IRI results was done with the VMD program. [29] The QTAIM analysis of model structures revealed the presence of bond critical points (3, -1) for intermolecular weak interactions in BFBi, as shown in Figure 1.9a and Table 1.2. The low magnitude of the electron density $\rho(\mathbf{r})$, the positive values of the Laplacian of the electron density $\nabla^2\rho(\mathbf{r})$, and the close to zero energy density H_b in these BCPs are typical of weak interactions in the range suggested for H-bonds. [30-31]

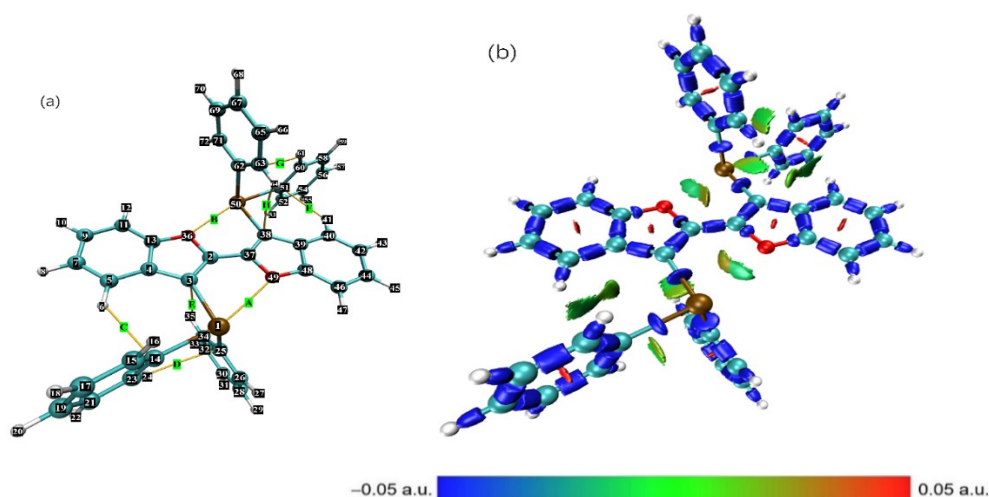


Figure 1.9. (a) Bond critical points (BCPs) (b) and $\text{sign}(\lambda^2)$ ρ -mapped IRI isosurface for BFBi, indicating bonding (covalent) interactions in blue, weak noncovalent van der Waals interactions in green, and repulsive interactions in orange.

Table 1.2. Values of the density of all electrons $\rho(\mathbf{r})$, Laplacian of the electron density $\nabla^2\rho(\mathbf{r})$, energy density H_b , potential energy $V(\mathbf{r})$, and Lagrangian kinetic energy $G(\mathbf{r})$ (in a.u.) at the bond critical points (3, -1) in BFBi.

BCP	$\rho(\mathbf{r})$	$\nabla^2\rho(\mathbf{r})$	H_b	$V(\mathbf{r})$	$G(\mathbf{r})$
A (Bi50...O36)	0.01289	0.0360	0.000297	-0.008409	0.008706
B (Bi1...O49)	0.01289	0.0360	0.000297	-0.008410	0.008707
C (H6...C14)	0.00847	0.0280	0.001408	-0.001408	0.005467
D (H24...C25)	0.00714	0.0244	0.001351	-0.001351	0.004748
E (H35...C3)	0.00730	0.0241	0.001291	-0.001291	0.004739
F (H41...C51)	0.00847	0.0280	0.001408	-0.001408	0.005468
G (H61...C62)	0.00714	0.0244	0.001351	-0.001351	0.004748
H (H72...C38)	0.00730	0.0241	0.001291	-0.001291	0.004740

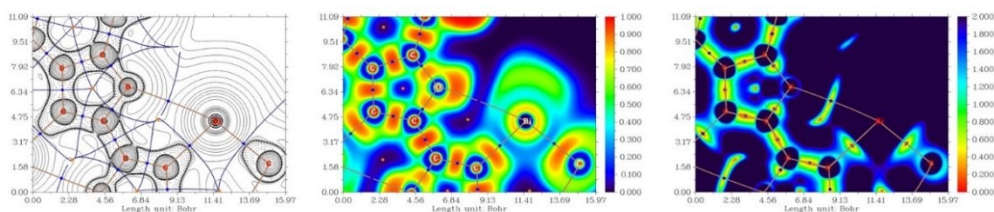


Figure 1.10. Contour line diagram of the Laplacian of the electron density distribution $\nabla^2 \rho(\mathbf{r})$, the bond paths, and the selected zero-flux surfaces (top); visualization of ELF (center); and IRI map (bottom) referring to noncovalent interactions in BFBi. Bond critical points (3, -1) are shown in blue, nuclear critical points (3, -3) in pale brown, and ring critical points (3, +1) in orange. Bond paths are shown as pale brown lines. Length is given in Å, and color scales for the ELF and IRI map are given in a.u.

The balance between the Lagrangian kinetic energy $G(\mathbf{r})$ and the potential energy density $V(\mathbf{r})$ at the BCPs (3, -1) reveals the nature of these interactions: the bonding is purely noncovalent if $-G(\mathbf{r})/V(\mathbf{r}) > 1$; if it is < 1 , some covalent character is involved. [22], [32-33] On the basis of these criteria, the author concluded that the points labeled A–H in Figure 1.9a (listed in Table 1.2) are akin to the range proposed in the criteria for the characterization of weak interactions, with points A and B being stronger than the others. [30-32] The IRI provides a qualitative picture of areas where weak interactions and chemical bonds are identified by different colors. The $\text{sign}(\lambda_2) \rho$ -mapped IRI isosurface shown in Figure 1.9b revealed covalent and noncovalent interactions in one chemical system. The contour line diagram of the Laplacian of the electron density distribution $\nabla^2 \rho(\mathbf{r})$, the bond paths, and the selected zero-flux surfaces; the visualization of ELF; and a color-filled map of the IRI for Bi \cdots O in BFBi are shown in Figure 1.10. The noncovalent Sb \cdots O, As \cdots O, and P \cdots O interactions in BFSb, BFAs, and BFP, respectively, were also evaluated in a similar manner, as shown in Figures 1.11 to 1.13, 1.16 and Tables 1.3 to 1.5. Weak

interactions in BTBi and BTSb were investigated by BCP analysis, and $\text{sign}(\lambda_2)$ ρ -mapped IRI isosurfaces are shown in Figures 1.14 to 1.16 and Tables 1.6 and 1.7.

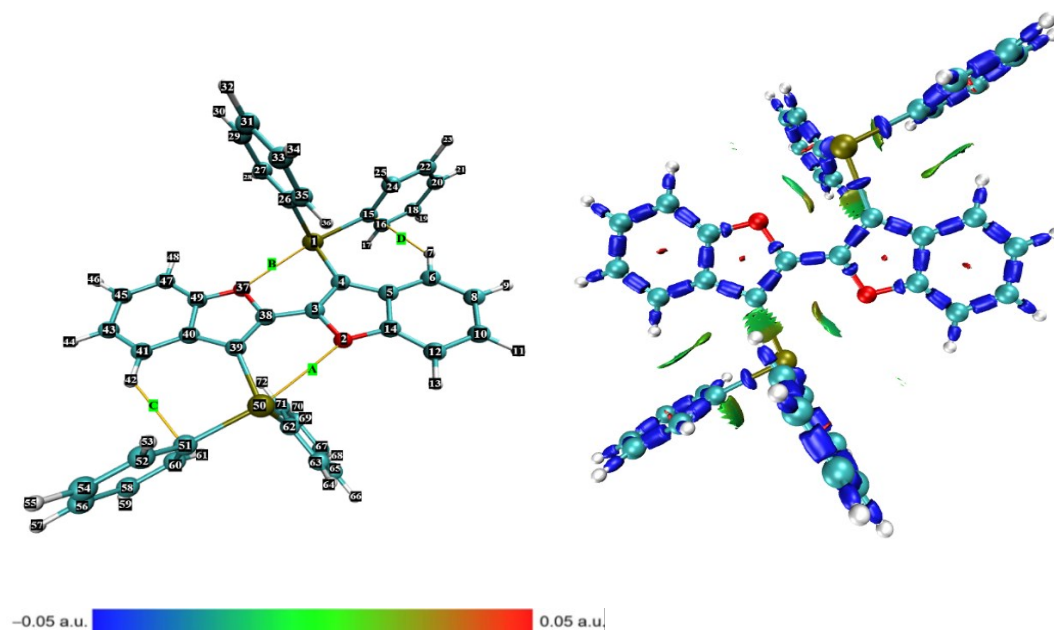


Figure 1.11. Bond critical points (BCPs) in BFSb; $\text{Sign}(\lambda_2)$ ρ -mapped IRI isosurface for BFSb.

Table 1.3. Values of the Density of All Electrons $\rho(\mathbf{r})$, Laplacian of Electron Density $\nabla^2\rho(\mathbf{r})$, Energy Density H_b , Potential Energy $V(\mathbf{r})$, and Lagrangian Kinetic Energy $G(\mathbf{r})$ (in a.u.) at the bond critical (3, -1), corresponding to $\text{Sb}\cdots\text{O}$ and other weak interaction in BFSb.

BCP	$\rho(\mathbf{r})$	$\nabla^2\rho(\mathbf{r})$	H_b	$V(\mathbf{r})$	$G(\mathbf{r})$
A (Sb50...O2)	0.01272	0.0342	0.000208	-0.008136	0.008345
B (Sb1...O37)	0.01272	0.0342	0.000208	-0.008136	0.008344
C (H7...C15)	0.00909	0.0302	0.001514	-0.004511	0.006025
D (H42...C51)	0.00909	0.0302	0.001514	-0.004511	0.006025

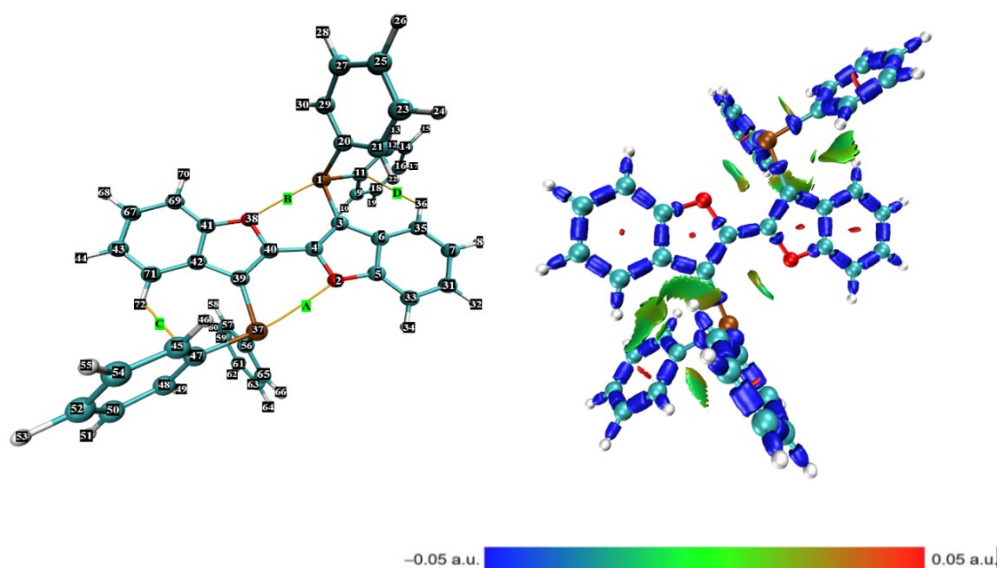


Figure 1.12. Bond critical points (BCPs) in BFAs; $\text{Sign}(\lambda_2)$ ρ -mapped IRI isosurface for BFAs.

Table 1.4. Values of the Density of All Electrons $\rho(\mathbf{r})$, Laplacian of Electron Density $\nabla^2\rho(\mathbf{r})$, Energy Density H_b , Potential Energy $V(\mathbf{r})$, and Lagrangian Kinetic Energy $G(\mathbf{r})$ (in a.u.) at the bond critical (3, -1), corresponding to $\text{As}\cdots\text{O}$ and other weak interaction in BFAs.

BCP	$\rho(\mathbf{r})$	$\nabla^2\rho(\mathbf{r})$	H_b	$V(\mathbf{r})$	$G(\mathbf{r})$
A (As37...O2)	0.01221	0.0339	0.000371	-0.007722	0.008093
B (As1...O38)	0.01221	0.0339	0.000371	-0.007721	0.008092
C (H72...C47)	0.00869	0.0294	0.001564	-0.004213	0.005776
D (H36...C11)	0.00869	0.0294	0.001564	-0.004216	0.005781

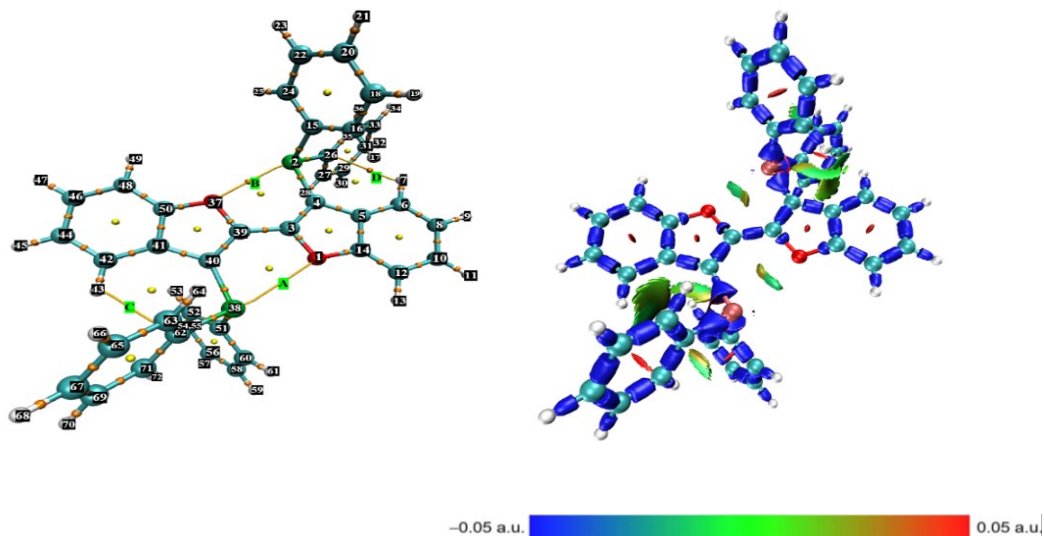


Figure 1.13. Bond critical points (BCPs) in BFP; $\text{Sign}(\lambda_2)$ ρ -mapped IRI isosurface for BFP.

Table 1.5. Values of the Density of All Electrons $\rho(\mathbf{r})$, Laplacian of Electron Density $\nabla^2\rho(\mathbf{r})$, Energy Density H_b , Potential Energy $V(\mathbf{r})$, and Lagrangian Kinetic Energy $G(\mathbf{r})$ (in a.u.) at the bond critical (3, -1), corresponding to $\text{P}\cdots\text{O}$ and other weak interaction in BFP.

BCP	$\rho(\mathbf{r})$	$\nabla^2\rho(\mathbf{r})$	H_b	$V(\mathbf{r})$	$G(\mathbf{r})$
A (P2...O37)	0.01254	0.0361	0.000349	-0.008333	0.008682
B (P38...O1)	0.01254	0.0361	0.000349	-0.008333	0.008682
C (H43...C62)	0.00896	0.0303	0.001552	-0.004467	0.006019
D (H7...C26)	0.00896	0.0303	0.001552	-0.004467	0.006019

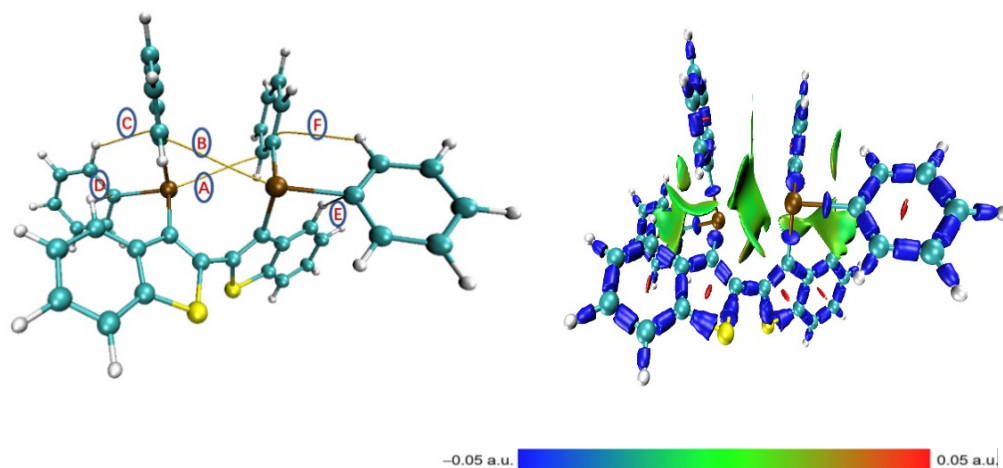


Figure 1.14. Bond critical points (BCPs) in BTBi; $\text{Sign}(\lambda_2)$ ρ -mapped IRI isosurface for BTBi.

Table 1.6. Values of the Density of All Electrons $\rho(\mathbf{r})$, Laplacian of Electron Density $\nabla^2\rho(\mathbf{r})$, Energy Density H_b , Potential Energy $V(\mathbf{r})$, and Lagrangian Kinetic Energy $G(\mathbf{r})$ (in a.u.) at the bond critical (3, -1), corresponding to some weak interaction in BTBi.

BCP	$\rho(\mathbf{r})$	$\nabla^2\rho(\mathbf{r})$	H_b	$V(\mathbf{r})$	$G(\mathbf{r})$
A (Bi...C)	0.00318	0.0074	0.000379	-0.001095	0.001473
B (Bi...C)	0.00318	0.0074	0.000379	-0.001095	0.001474
C (H...C)	0.00693	0.0219	0.001187	-0.003096	0.004283
D (H...C)	0.00663	0.0211	0.001204	-0.002890	0.004093
E (H...C)	0.00663	0.0211	0.001204	-0.002890	0.004093
F (H...C)	0.00693	0.0219	0.001187	-0.003096	0.004282

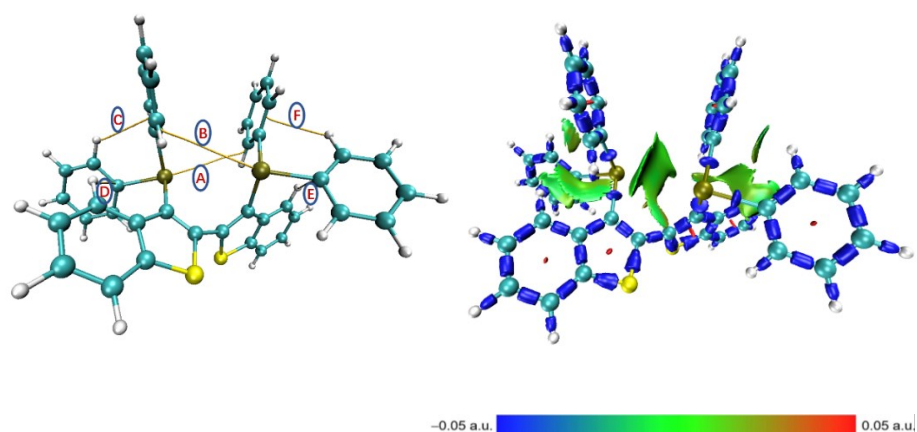


Figure 1.15. Bond critical points (BCPs) in BTSb; $\text{Sign}(\lambda_2)$ ρ -mapped IRI isosurface for BTSb.

Table 1.7. Values of the Density of All Electrons $\rho(\mathbf{r})$, Laplacian of Electron Density $\nabla^2\rho(\mathbf{r})$, Energy Density H_b , Potential Energy $V(\mathbf{r})$, and Lagrangian Kinetic Energy $G(\mathbf{r})$ (in a.u.) at the bond critical (3, -1), corresponding to some weak interaction in BTSb.

BCP	$\rho(\mathbf{r})$	$\nabla^2\rho(\mathbf{r})$	H_b	$V(\mathbf{r})$	$G(\mathbf{r})$
A (Sb...C)	0.00267	0.0062	0.000344	-0.000884	0.001228
B (Sb...C)	0.00240	0.0063	0.000359	-0.000861	0.001219
C (H...C)	0.00779	0.0248	0.001331	-0.003532	0.004684
D (H...C)	0.00673	0.0218	0.001237	-0.002977	0.004215
E (H...C)	0.00673	0.0218	0.001238	-0.002890	0.004216
F (H...C)	0.00779	0.0248	0.001332	-0.003533	0.004864

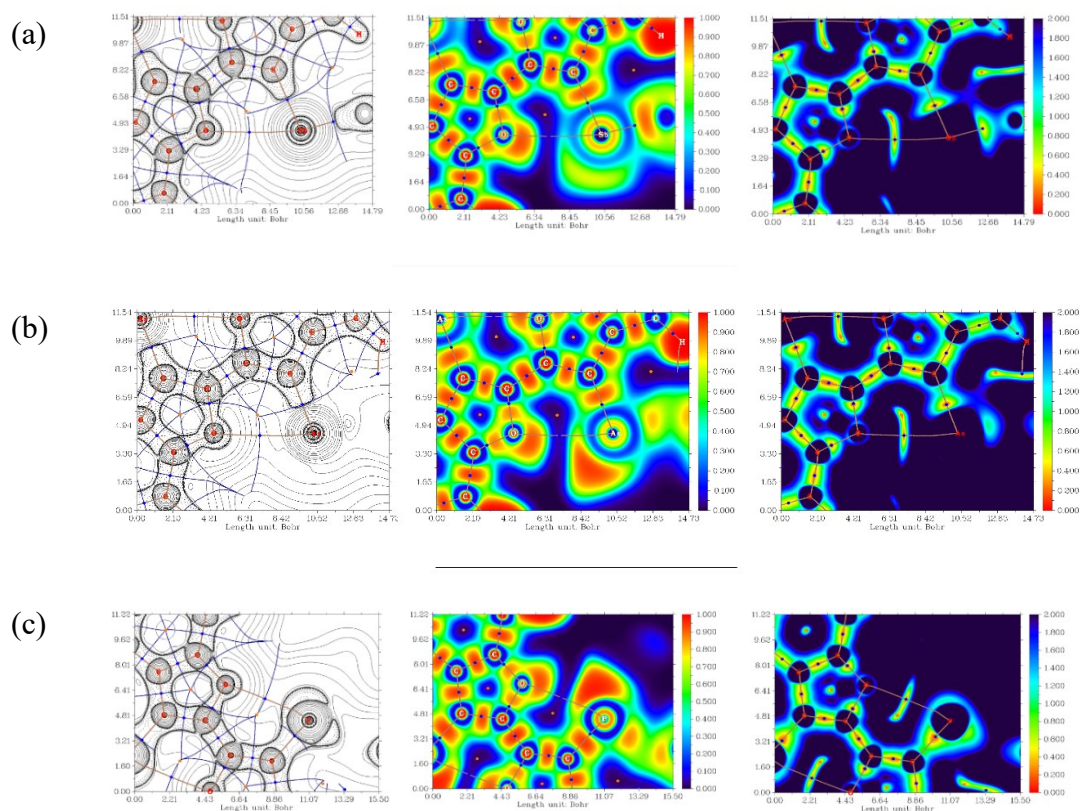


Figure 1.16. Contour line diagram of the Laplacian of electron density distribution $\nabla^2 \rho(r)$, bond paths and selected zero-flux surfaces (left), visualization of ELF (middle), and IRI maps (right) referring to (a) $\text{Sb}\cdots\text{O}$, (b) $\text{As}\cdots\text{O}$, (c) $\text{P}\cdots\text{O}$ noncovalent interactions in BFSb. Bond critical points (3, -1) are shown in blue, nuclear critical points (3, -3) in pale brown, and ring critical points (3, +1) in orange. Bond paths are shown as pale brown lines. Length is given in Å and the color scales for the ELF and IRI maps are in a.u.

NBO theory is valuable for understanding molecular conformation from the viewpoint of local orbital interaction. In the case of BFBi, the $\text{Bi}\cdots\text{O}$ noncovalent interactions can be attributed to the electron delocalization from the filled LP (lone pair) of O49/O36 ‘electron donor’ into unfilled antibonding σ^* orbital of Bi1-C14/Bi50-C51 ‘electron acceptor’ (D-A interaction). This transition showed the stabilization energy of 2.97 kcal/mol. Similarly, $\text{LP} \rightarrow \sigma^*(\text{Sb-C})$ and $\text{LP} \rightarrow \sigma^*(\text{As-C})$ showed stabilization energies of 2.35 and 1.65 kcal/mol, respectively (Table 1.8), corresponding to the weaker D-A interactions than $\text{LP} \rightarrow \sigma^*(\text{Bi-C})$. It is interesting to

note that the obtained results at the NBO basics are in complete agreement with the results obtained from AIM (*vide supra*).

Table 1.8. NBO analysis of donor-acceptor interactions in BFBi, BFSb and BFAs (LP to $\sigma_{Bi/Sb/As-C}^*$) calculated at the BP86/6-31g(d) level for other elements; cc-PVTZ-PP level for Bi/Sb/As.

Comp	NBO	Donor	NBO	Acceptor	$E_a(2)$	$E(j)E(i)$	$F(i,j)$
ound						(a.u.)	(a.u.)
BFBi	61	LP (1) Bi1	173	$\sigma^*(C3-C4)$	0.94	0.87	0.026
	61	LP (1) Bi1	190	$\sigma^*(C14-C23)$	0.82	0.94	0.025
	61	LP (1) Bi1	203	$\sigma^*(C25-C34)$	0.74	0.94	0.024
	62	LP (1) O36	169	$\sigma^*(C2-C3)$	3.21	0.99	0.05
	62	LP (1) O36	172	$\sigma^*(C2-C37)$	0.65	0.93	0.05
	62	LP (1)O36	175	$\sigma^*(C4-C13)$	3.25	0.95	0.05
	62	LP (1) O36	235	$\sigma^*(Bi50-C51)$	2.97	0.52	0.035
	64	LP (1) O49	167	$\sigma^*(Bi1-C14)$	2.97	0.52	0.035
BFSb	62	LP (1)O2	235	$\sigma^*(Sb50-C51)$	2.35	0.55	0.032
	64	LP (1)O37	167	$\sigma^*(Sb1-C15)$	2.35	0.55	0.032
BFAs	62	LP (1)O2	217	$\sigma^*(As37-C47)$	1.65	0.58	0.027
	65	LP (1)O38	167	$\sigma^*(As1-C11)$	1.65	0.58	0.027

E_2 is the energy of hyperconjugative interaction (stabilization energy in kcal mol⁻¹); $E(j)E(i)$ is the energy difference between donor and acceptor i and j NBO orbitals; $F(i;j)$ is the Fock matrix element between i and j NBO orbitals.

The HOMO and LUMO levels of BFBi, BFSb, BFAs, and BFP were similar, resulting in similar HOMO–LUMO energy gaps (Table 1.9). As different basic sets are used for P and Bi/Sb/As, the exact different of the energies are difficult, but rough comparisons seem possible. This clearly indicates that the lower energy absorption

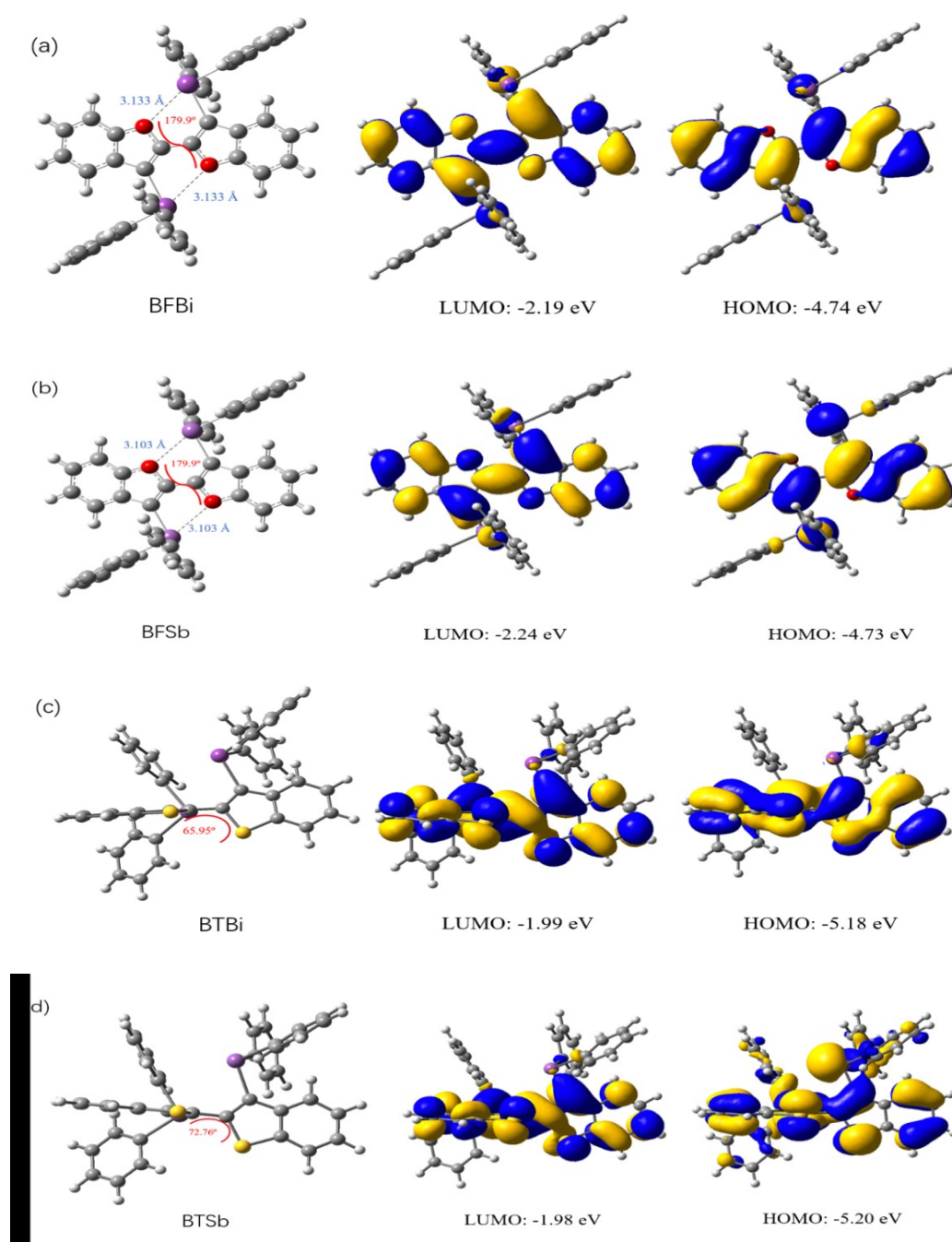
bands of BFBi, BFSb, and BFAs, as compared with that of BFP, are not due to differences in the electronic state, but rather can be explained by the enhanced planarity owing to the stronger noncovalent Bi \cdots O, Sb \cdots O, and As \cdots O interactions than the P \cdots O interaction.

Table 1.9. LUMO and HOMO energy levels of BFBi, BFSb, BFAs, BFP, bibenzofuran (BF) and bibenzothiophene (BT) derived from DFT calculations at the BP86/6-31G(d) level with cc-pVTZ-PP basis set for Bi/Sb/As.

Compound	LUMO/eV	HOMO/eV	E _g /eV	Dihedral Angle/deg	Center bond length/Å	C-C d[O...X]/Å (X=Bi, Sb, P, H)
BFBi	-2.19	-4.74	2.55	-179.99	1.4413	3.133
BFSb	-2.24	-4.73	2.49	179.99	1.4403	3.103
BFAs	-2.31	-4.81	2.50	-180	1.4436	3.071
BTBi	-1.99	-5.18	3.20	65.95	1.4698	-
BTSb	-1.98	-5.20	3.23	72.76	1.4721	-
BFP	-2.38	-4.71	2.33	179.99	1.4431	3.045
BF	-2.20	-4.88	2.68	180	1.4366	-
BT	-2.39	-4.98	2.60	180	1.4478	-

The HOMO–LUMO energy gap of BFBi is slightly larger than that of BFSb, which is in line with the optical data. These calculations indicate that BFBi, BFSb, and BFAs show planar or nearly planar conformations with the Bi \cdots O, Sb \cdots O, and As \cdots O distances being 3.133 Å, 3.103 Å, and 3.071 Å, respectively, which are much shorter than the sums of the van der Waals radii of the respective atoms, as observed in the crystal structures (Table 1.9 and Figure 1.17). The central C–C bond distances of BFBi and BFSb (1.4413 Å and 1.4403 Å) are shorter than those of BTBi and BTSb (1.4698 Å and 1.4721 Å), but slightly longer than that of bibenzofuran (1.4366 Å) by 0.0047 Å and 0.0037 Å, respectively, reproducing well the crystal structures. The

central C-C bond of planar BFBi is much shorter than that of the twisted BFBi with the torsion angle of 90° (1.4689 Å), despite that the twisted conformation should have smaller steric repulsion, clearly indicating that the Bi \cdots O noncovalent interaction shortens the central C-C bond of planar BFBi. It was also found that the bismuth, antimony, arsenic, and phosphorous atoms contributed to the HOMO to elevate the energy levels, agreeing with the results of CVs (Figure 1.17).



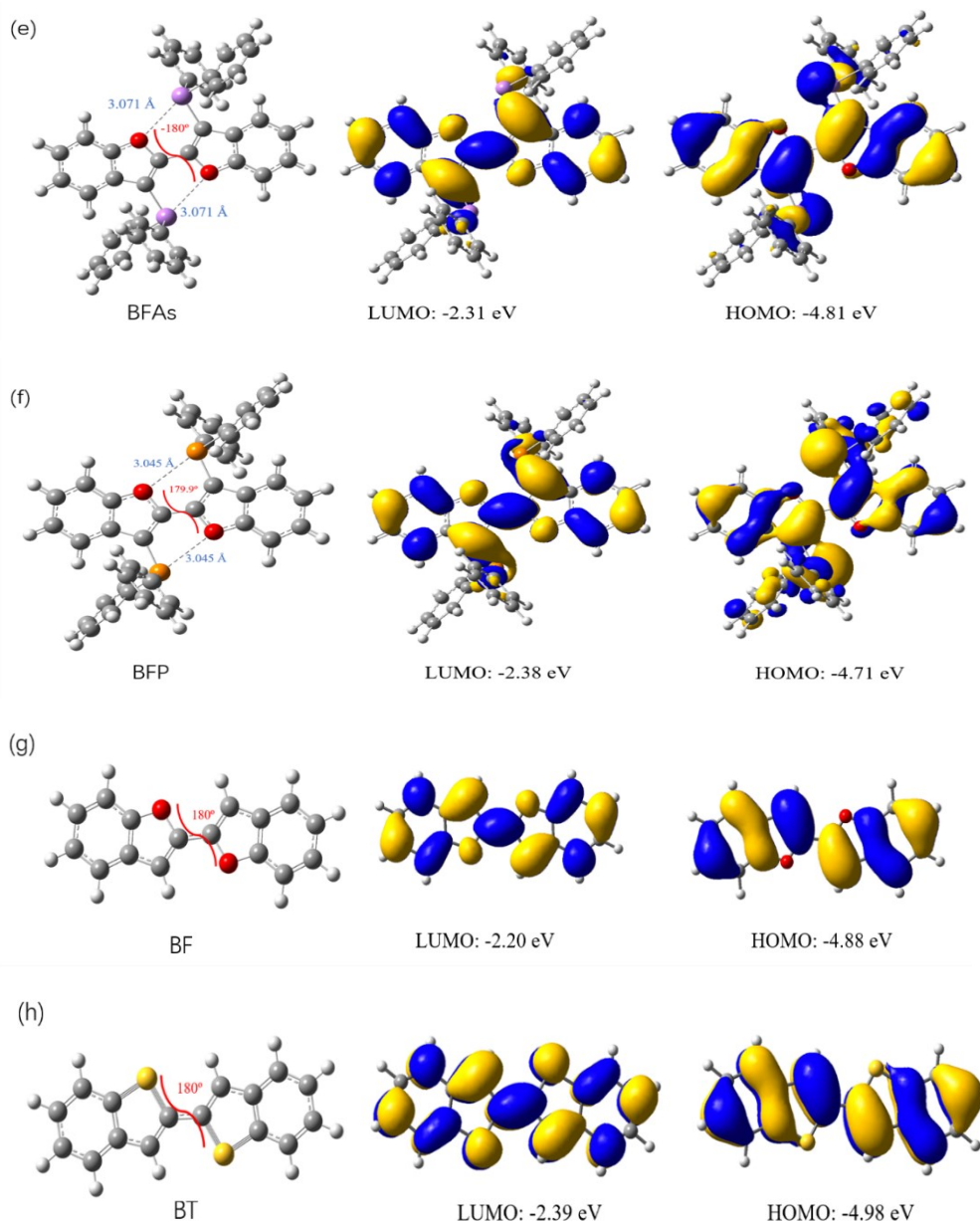


Figure 1.17. Optimized structure, LUMO and HOMO profiles of (a) BFBi, (b) BFSb, (c) BTBi, (d) BTSb, (e) BFAs, (f) BFP, (g) bibenzofuran (BF) and (h) bibenzothiophene (BT).

On the other hand, the optimized geometries of BTBi and BTSb showed twisted structures with torsion angles of 65.95° and 72.76° , respectively, similarly to the crystal structures. The higher degree of twisting in the gas phase than in the crystal phase is possibly due to the packing force and/or intermolecular noncovalent interactions. BFBi and BTBi were computed with different inter-ring torsion angles to

estimate the rotation barrier of the central C–C bonds. In these calculations, the torsion angles were changed by 10°, and other structural parameters were optimized, as shown in Figures 1.18 and 1.19. The data of fully optimized structures are also provided in Figures 1.18 and 1.19. BTBi showed a higher rotation barrier than BFBi. Two types of stable structures (twisted and planar) with torsion angles of $\pm 50^\circ$ and $\pm 180^\circ$ were obtained for BFBi, with the planar structure being much more stable than the twisted structure. Meanwhile, BTBi showed an energy minimum at $\pm 60^\circ$ and $\pm 120^\circ$, which agrees with the experimental observation. The rotation barrier of unsubstituted bibenzofuran was also calculated to be 7.0 kcal/mol (Figure 1.18), which was higher than that between twisted and planar stable structures of BFBi (5.7 kcal/mol). In BFBi, the steric repulsion with respect to the sterically large bismuth substituents offsets the influence of noncovalent Bi \cdots O interactions to an extent to reduce the rotation barrier.

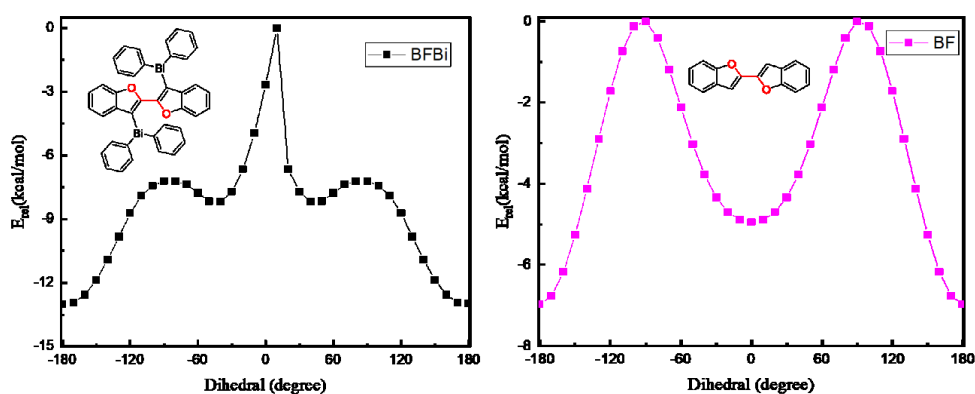


Figure 1.18. Torsional potential for BFBi and bibenzofuran (BF) calculated at BP86/6-31G(d); cc-pVTZ-PP for Bi. Rotatable bond highlighted in red, where the -180° conformer is shown.

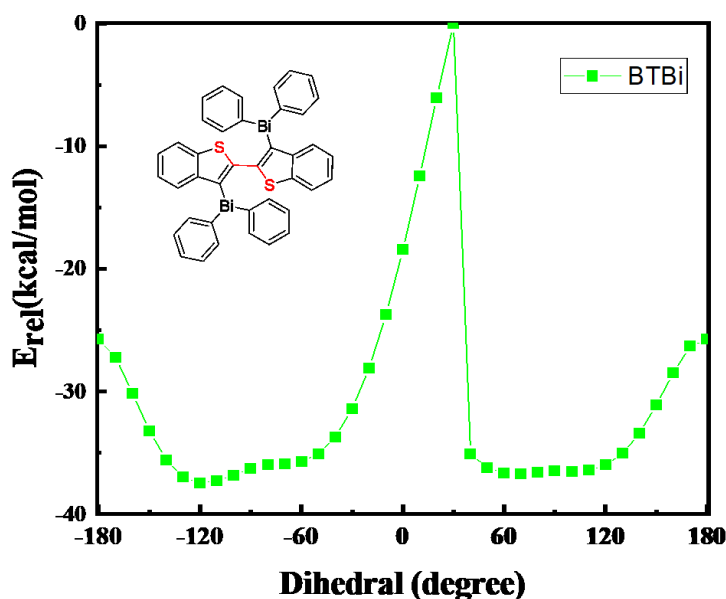


Figure 1.19. Torsional potential for BTBi calculated at BP86/6-31G(d); cc-pVTZ-PP for Bi. Rotatable bond highlighted in red, where the -180° conformer is shown.

Conclusion

In summary, the author synthesized bismuth-, antimony-, and arsenic-substituted bibenzofurans and bibenzothiophenes. The single crystal X-ray diffraction study revealed the presence of attractive intramolecular noncovalent $\text{Bi}\cdots\text{O}$, $\text{Sb}\cdots\text{O}$, and $\text{As}\cdots\text{O}$ interactions, which enhanced the self-planarization and rigidification of the π -conjugated systems. According to theoretical calculations including QTAIM analysis, BCPs were found between $\text{Bi}\cdots\text{O}$, $\text{Sb}\cdots\text{O}$, and $\text{As}\cdots\text{O}$, corresponding to the van der Waals interactions as revealed by IRI. Visual examination of weak interactions was performed using the Multiwfn program. The experimental data and the DFT calculations revealed that the HOMO and LUMO energy levels of bismuth- and antimony-substituted bibenzofurans and bibenzothiophenes were lower than those reported previously for BFP, [8] reflecting the stronger noncovalent interactions. In addition, the absorption spectra were red-shifted as a result of enhanced conjugation due to the higher planarity owing to these interactions. It is noteworthy that bismuth, antimony, and arsenic atoms may provide both intermolecular and intramolecular

interactions when incorporated into other cyclic ether-based π -conjugated backbones, with the potential to afford structural control in the solid state, and ultimately, improved device performance. The author has not yet examined the device fabrication based on these substituted bibenzofurans. However, the good film forming property of BFBi indicated its potential application as a device material.

Experimental section

General.

All reactions were carried out under dry argon atmosphere. Diethyl ether was dried over CaH_2 and distilled and stored over activated molecular sieves until use. 3,3'-Dibromo 2,2'-bi(benzofuran) (BBFBr) and 3,3'-Dibromo 2,2'-bi(benzothiophene) (BTBr) were synthesized according to the previously reported procedures. [34] NMR spectra were recorded on a Varian 400-MR spectrometer. FD-mass spectra were measured on a JMS-T100 GCV spectrometer. UV-vis absorption and PL (photoluminescence) spectra were measured on Shimadzu UV-3600 and HORIBA FluoroMax-4 spectrophotometers, respectively. The PL quantum yields were determined by using a HORIBA FluoroMax-4 spectrophotometer attached to an integrating sphere, using degassed solvents by bubbling argon for solutions. Preparative GPC was performed using Shodex KF001 and KF002 columns connected in a series with RI detection. Toluene was used as eluent. For BFAs, NMR spectra were recorded on a Varian 400 NMR spectrometer using Me_4Si (TMS) as an internal standard; UV-vis absorption and PL (photoluminescence) spectra were recorded on a JASCO spectrophotometer V-670 KNN and FP-8500 instrument (JASCO), respectively. Cyclic voltammograms (CVs) of BFBi, BFSb, BTBi, BTSb and BFAs were obtained using a platinum disk working electrode, a platinum wire counter electrode, and an Ag/AgCl reference electrode at a scan rate of 100 mV/s, the measurements were carried out in acetonitrile containing 0.1 M tetrabutylammonium hexafluorophosphate as an electrolyte, and the Fc/Fc^+ redox couple was used as an external standard having an oxidation potential of +0.48 V vs SCE. For BFAs, acetonitrile was replaced by dichloromethane.

Theoretical Calculation Detail.

All computations were carried out using the Gaussian16 program package, at the BP86 functional. The cc-PVTZ-PP basis set was used for the Bi, Sb and As atoms, as found in the EMSL basis set exchange Web site [38] and 6-31G(d) basis set with polarization functions was used for the rest of the atoms. Geometry optimizations were performed without any symmetry restrictions, using the initial coordinates derived from the X-ray data when available, and frequency analyses were performed to ensure that a minimum structure with no imaginary frequencies was achieved in each case. Torsional PESs were calculated at the same level in the gas phase for BFBi and BTBi. For each dihedral, the defined torsional angle was fixed and the rest of the structure allowed to relax. Total energies were converted to relative energies versus the around 0° conformer to allow comparison of stabilizing effects.

Synthesis of BFBi.

To a solution of 0.471g (1.201 mmol) of 3,3'-dibromo-2,2'-bibenzofuran (BBFBr) in 10 mL of ether was added 1.53 mL of 1.6 M *n*-BuLi in hexane at -78 °C and the mixture was stirred for 1 h at this temperature. After addition of chlorodiphenylbismuthane (ca. 3.0 mmol) prepared from triphenylbismuthane (2.0 mmol) and bismuth (III) chloride (1.0 mmol) in 4 mL of ether, [35] the reaction mixture was stirred for 12 h, during which time the temperature was raised to ambient temperature. After evaporation of the solvent, the residue was diluted with 10 mL of toluene and was hydrolyzed with 10 mL water. The organic layer and the extracts were combined and dried over anhydrous magnesium sulfate. The residue was subjected to silica gel column chromatography eluting with hexane/DCM = 4/1; v/v to give crude solids, which were purified by preparative GPC eluting with toluene. Finally, recrystallization of the resulting solids from ethanol to give 0.183 g (16% yield) of BFBi as colorless solids: mp 250.1-251.1 °C; ¹H NMR (400 MHz, CDCl₃) δ 7.92 (dd, *J* = 8.0 Hz, 1.4 Hz, 8H, phenyl ring protons), 7.48 (d, *J* = 8.0 Hz, 2H, benzofuran ring protons), 7.38 (t, *J* = 8.0 Hz, 8H, phenyl ring protons), 7.32 - 7.28 (m, 4H, phenyl ring protons), 7.17 - 7.13(m, 2H, benzofuran ring protons), 6.86 - 6.82 (m,

2H, benzofuran ring protons), 6.65 (d, $J = 8.0$ Hz, 2H, benzofuran ring protons); ^{13}C NMR (100 MHz, CDCl_3) δ 156.7, 153.6, 138.3, 135.7, 130.6, 128.0, 124.9, 124.5, 122.9, 110.9; High resolution FD MS m/z calcd for $\text{C}_{40}\text{H}_{28}\text{Bi}_2\text{O}_2$ [M^+]: 958.16970, Found: 958.16835.

Synthesis of BTBi.

BTBi was synthesized in a fashion like that of BFBi, by using BBTBr (1.045 mmol) instead of BBFBr and chlorodiphenylbismuthane (ca. 2.1 mmol). Data for BTBi: white solid; 0.181 g (13% yield). mp 224.1-226.1 °C; ^1H NMR (400 MHz, DMSO-d_6) δ 8.02 (d, $J = 8.0$ Hz, 2H, benzothiophene ring protons), 7.77 - 7.73 (m, 8H, phenyl ring protons), 7.32 (t, $J = 8.0$ Hz, 8H, phenyl ring protons), 7.26 - 7.20 (m, 6H, mixture), 7.06 (d, $J = 8.0$ Hz, 2H, benzothiophene ring protons), 6.95 - 6.91 (m, 2H, benzothiophene ring protons); ^{13}C NMR (100 MHz, CDCl_3) δ 153.6, 152.4, 146.4, 144.8, 144.4, 138.1, 130.7, 128.0, 127.9, 125.0, 124.5, 122.1. High resolution FD MS m/z calcd for $\text{C}_{40}\text{H}_{28}\text{Bi}_2\text{S}_2$ [M^+]: 990.12401, Found: 990.12608.

Synthesis of BFSb.

BFSb was synthesized in a fashion like that of BFBi, by using BBFBr (1.15 mmol) and diphenylstibine chloride (ca. 2.3 mmol) that was synthesized according to the previously reported procedure [36] instead of chlorodiphenylbismuthane. Light yellow solids. 0.081 g (9% yield); mp 240.9-241.4 °C; ^1H NMR (400 MHz, CDCl_3) δ 7.61 - 7.57 (m, 8H, phenyl ring protons), 7.41 (d, $J = 8.0$ Hz, 2H, benzofuran ring protons), 7.34 - 7.28 (m, 12H, phenyl ring protons), 7.17 (t, $J = 8.0$ Hz, 2H, benzofuran ring protons), 6.84 (t, $J = 8.0$ Hz, 2H, benzofuran ring protons), 6.56 (d, $J = 8.0$ Hz, 2H, benzofuran ring protons); ^{13}C NMR (100 MHz, CDCl_3) δ 155.6, 153.1, 137.5, 136.4, 136.3, 132.8, 132.8, 129.0, 128.7, 123.0, 112.2, 110.8. High resolution FD MS m/z calcd for $\text{C}_{40}\text{H}_{28}\text{Sb}_2\text{O}_2$ [M^+]: 782.01657, Found: 782.01757.

Synthesis of BTSb.

BTSb was synthesized in a fashion like that of BFSb, by using BBTBr (1.07

mmol) instead of BBFBr and chlorodiphenylbismuthane (ca. 2.1 mmol). Light yellow solid; 0.052 g (6% yield); mp 198.3-200.1 °C; ¹H NMR (400 MHz, CDCl₃) δ 7.82 (d, *J* = 8.0 Hz, 2H, benzothiophene ring protons), 7.45 - 7.43 (m, 8H, phenyl ring protons), 7.30 - 7.27 (m, 4H, benzothiophene protons), 7.25 - 7.21 (m, 12H, phenyl ring protons), 7.01 (t, *J* = 8.0 Hz, 2H, benzothiophene ring protons); ¹³C NMR (100 MHz, CDCl₃) δ 146.0, 143.4, 142.7, 136.8, 136.3, 129.0, 128.6, 128.6, 126.9, 125.0, 124.4, 122.0; High resolution FD MS *m/z* calcd for C₄₀H₂₈Sb₂S₂ [M⁺]: 813.97089, Found: 813.97170.

Synthesis of BFAs.

To a solution of 0.202 g (0.515 mmol) of 3,3'-dibromo-2,2'-bibenzofuran (BBFBr) in 4 mL of ether was added 0.67 mL of 1.6 M *n*-BuLi in hexane at -78 °C and the mixture was stirred for 1 h at this temperature. After addition of neat iododiphenylarsine [37] (0.464 g, 1.30 mmol), the reaction mixture was stirred for 12 h, during which time the temperature was raised to ambient temperature. After evaporation of the solvent, the residue was taken up with 30 mL of dichloromethane and insoluble salts were filtered. The volatiles were removed in vacuo. The residue was recrystallized from hot toluene to give 0.116 g (33% yield) of BFAs as pale yellow solids: mp. 262.5-263.2 °C; ¹H NMR (400 MHz, CDCl₃) δ 7.50 - 7.46 (m, 10H, phenyl ring protons and benzofuran ring protons), 7.31 - 7.27 (m, 12H, phenyl ring protons), 7.24 - 7.22 (m, 2H, benzofuran ring protons), 6.91 (td, *J* = 8.0, 0.8 Hz, 2H, benzofuran ring protons), 6.65 (d, *J* = 7.2 Hz, 2H, benzofuran ring protons); ¹³C NMR (100 MHz, CDCl₃) δ 155.7, 151.4, 138.5, 133.5, 130.7, 128.7, 128.5, 125.3, 123.1, 123.0, 115.5, 111.7; High resolution MS *m/z* calcd for C₄₀H₂₈As₂O₂ [M⁺]: 691.0593995, Found: 691.06012.

Table 1.10. The crystallographic data of all the molecules.

Molecule	BFBi	BFSb	BFAs	BTBi	BTSb
Formula	C ₄₀ H ₂₈ O ₂ Bi ₂	C ₄₀ H ₂₈ O ₂ Sb ₂	C ₄₀ H ₂₈ O ₂ As ₂	C ₄₀ H ₂₈ S ₂ Bi ₂	C ₄₀ H ₂₈ S ₂ Sb ₂
Formula weight	958.58	784.12	690.46	990.70	816.24

Temperature (K)	100.00(10)	100	75	100	100.00(10)
Radiation	MoK α (λ =0.71073)	MoK α (λ =0.71073)	MoK α (λ =0.71073)	MoK α (λ =0.71073)	MoK α (λ =0.71073)
Crystal system	monoclinic	triclinic	triclinic	Monoclinic	monoclinic
Space group	P2 ₁ /n	P -1	P -1	P2 ₁ /n	P2 ₁ /n
a(Å)	15.6929(5)	7.93340(10)	8.222(2)	14.8487(3)	14.7169(2)
b(Å)	5.7363(2)	8.94400(10)	8.836(3)	8.7774(2)	8.81280(10)
c(Å)	18.1211(6)	12.3077(2)	11.806(2)	25.7490(5)	25.6552(4)
α (°)	90	89.3110(10)	88.87(2)	90	90
β (°)	107.694(3)	83.0640(10)	82.78(2)	99.398(2)	99.1180(10)
γ (°)	90	67.7760(10)	66.43(3)	90	90
Volume (Å ³)	1554.08(9)	801.98(2)	779.5(4)	3310.90(12)	3285.36(8)
Z	2	1	1	4	4
μ /(mm ⁻¹)	11.343	1.719	2.179	10.769	1.800
F(000)	900.0	386.0	350	1864.0	1608.0
Crystal size (mm)	0.135 x 0.082 x 0.045	0.112 x 0.087 x 0.048	0.64 x 0.16 x 0.13	0.155 x 0.126 x 0.068	0.15 x 0.12 x 0.1
Theta range for data collection (°)	4.11/59.08	4.924/59.616	5.032/52.74	4.91/59.394	4.894/59.686
Index ranges	-21 \leq h \leq 18; -7 \leq k \leq 6; -24 \leq l \leq 22	-10 \leq h \leq 10; -12 \leq k \leq 11; -17 \leq l \leq 16	-10 \leq h \leq 10; -11 \leq k \leq 10; -14 \leq l \leq 12	-20 \leq h \leq 17; -12 \leq k \leq 10; -31 \leq l \leq 34	-19 \leq h \leq 19; -11 \leq k \leq 12; -35 \leq l \leq 34
Reflections collected	16208	19596	4489	37264	85653
Data / restraints / parameters	3700/ 0 / 199	3842/ 0 / 199	3175/63/175	8007/ 0 /397	8338/ 0 / 397
Independent reflections	3700[R _{int} =0.0346]	3842[R _{int} =0.0257]	3175[R _{int} =0.1445, R _{sigma} =0.3433]	8007[R _{int} =0.0317]	8338[R _{int} =0.0534]
Goodness-of-fit on F ²	1.046	1.093	0.912	1.016	1.043
Final R indices R ₁ and wR ₂ [I > 2 σ (I)]	0.0195/0.0348	0.0199/0.0482	0.0972/0.1718	0.0193/0.0361	0.0247/0.0471
Final R indices (all data) R ₁ and wR ₂	0.0243/0.0357	0.0220/0.0489	0.2133/0.2375	0.0256/0.0372	0.0349/0.0492
Largest diff. peak/hole/ e ⁻ Å ⁻³	0.77/-0.75	0.70/-0.24	1.02/-1.25	1.02/-0.74	0.45/-0.45

REFERENCES

- [1]. Khasbaatar, A.; Xu, Z.; Lee, J.H.; Campillo-Alvarado, G.; Hwang, C.; Onusaitis, B.N.; Diao, Y. *J. Am. Chem. Soc.* **2023**, *123*, 8395-8487.
- [2]. Zhang, W.; Mao, Z.; Huang, J.; Gao, D.; Yu, G. *Macromolecules* **2016**, *49*, 6401-6410.
- [3]. Shi, Y.; Tang, Y.; Yang, K.; Qin, M.; Wang, Y.; Sun, H.; Su, M.; Lu, X.; Zhou, M.; Guo, X. *J. Mater. Chem. C* **2019**, *7*, 11142-11151.
- [4]. Saito, M.; Fukuhara, T.; Kamimura, S.; Ichikawa, H.; Yoshida, H.; Koganezawa, T.; Ie, Y.; Tamai, Y.; Kim, H. D.; Ohkita, H.; Osaka, I. *Adv. Energy Mater.* **2020**, *10*, 1903278.
- [5]. Sun, W.; Wang, C. H.; Lv, S. F.; Jiang, J. X.; Guo, X.; Zhang, F. B. *Org. Electron.* **2020**, *77*, 105548.
- [6]. Chen, X. K.; Bakr, B. W.; Auffray, M.; Tsuchiya, Y.; Sherrill, C. D.; Adachi, C.; Bredas, J. L. *J. Phys. Chem. Lett.* **2019**, *10*, 3260-3268.
- [7]. Yang, M.; Wei, W.; Zhou, X.; Wang, Z.; Duan, C. *Adv. Energy Mater.* **2021**, *1*, 100008.
- [8]. Wang, C. H.; Gao, Z. C.; Sun, W. P.; Guo, X. G.; Zhang, F. B. *Dyes. Pigm.* **2021**, *184*, 108820.
- [9]. Ohshita, J.; Matsui, S.; Yamamoto, R.; Mizumo, T.; Ooyama, Y.; Harima, Y.; Murafuji, T.; Tao, K.; Kuramochi, Y.; Kaikoh, T.; Higashimura, H. *Organometallics* **2010**, *29*, 3239-3241.
- [10]. Toma, O.; Mercier, N.; Allain, M.; Forni, A.; Meinardi, F.; Botta, C. *Dalton. Trans.* **2015**, *44*, 14589-14593.
- [11]. Toma, O.; Allain, M.; Meinardi, F.; Forni, A.; Botta, C.; Mercier, N. *Angew. Chem. Int. Ed. Engl.* **2016**, *55*, 7998-8002.
- [12]. Parke, S. M.; Hupf, E.; Matharu, G. K.; Aguiar, I. D.; Xu, L.; Yu, H. Y.; Boone, M. P.; Souza, G.L.; McDonald, R.; Ferguson, M. J.; He, G.; Brown, A.; Rivard, E. *Angew. Chem. Int. Ed.* **2018**, *57*, 14841-14846.
- [13]. Mantina, M.; Chamberlin, A. C.; Valero, R.; Cramer, C. J.; Truhlar, D. G. *J. Phys.*

Chem. A **2009**, *113*, 5806-5812.

[14]. Bondi, A. *J. Phys. Chem.* **1964**, *68*, 441-451.

[15]. Ionkin, A. S.; Marshall, W. J. *Organometallics* **2004**, *23*, 3276-3283.

[16]. Rasmussen, S. C.; Evenson, S. J.; McCausland, C. B. *Chem. Commun.* **2015**, *51*, 4528-4543.

[17]. Becke, A. D. *Phys. Rev. A* **1988**, *38*, 3098-3100.

[18]. Perdew, J. P. *Phys. Rev. B* **1986**, *33*, 8822-8824.

[19]. Peterson, K. A.; Figgen, D.; Goll, E.; Stoll, H.; Dolg, M. *J. Chem. Phys.* **2003**, *119*, 11113-11123.

[20]. Peterson, K. A.; Puzzarini, C. *Theor. Chem. Acc.* **2005**, *114*, 283-296.

[21]. Figgen, D.; Rauhut, G.; Dolg, M.; Stoll, H. *Chem. Phys.* **2005**, *311*, 227-244.

[22]. Grimme, S.; Antony, J.; Ehrlich, S.; Krieg, H. *J. Chem. Phys.* **2010**, *132*, 154104.

[23]. Peterson, K. A. *J. Chem. Phys.* **2003**, *119*, 11099-11112.

[24]. Lu, T.; Chen, F. W. *J. Comput. Chem.* **2012**, *33*, 580-592.

[25]. Bader, R. F. W. *Acc. Chem. Res.* **1985**, *18*, 9-15.

[26]. Becke, A. D.; Edgecombe, K. E. *J. Chem. Phys.* **1990**, *92*, 5397-5403.

[27]. Savin, A.; Nesper, R.; Wengert, S.; Fässler, T. F. *Angew. Chem. Int. Ed.* **1997**, *36*, 1808-1832.

[28]. (a) Lu, T.; Chen, Q. X. *Chem. Eur. J.* **2021**, *1*, 231-239. (b) Lu, T.; Chen, Q. X. *Comput. Theor. Chem.* **2021**.

[29]. Humphrey, W.; Dalke, A.; Schulten, K. *J. Mol. Graphics* **1996**, *14*, 33-38.

[30]. Koch, U.; Popelier, P. *J. Phys. Chem.* **1995**, *99*, 9747-9754.

[31]. Kumar, P. S. V.; Raghavendra, V.; Subramanian, V. *J. Chem. Sci.* **2016**, *128*, 1527-1536.

[32]. Enrique E.; Ibon, A.; Jose, E.; Elies, M. *J. Chem. Phys.* **2002**, *117*, 5529-5542.

[33]. Jenkins, S.; Morrison, I. *Chem. Phys. Lett.* **2000**, *317*, 97-102.

[34]. Zhang, F. B.; Ooyama, Y.; Ohshita, J. *ChemistrySelect.* **2017**, *2*, 3106-3109.

[35]. Barton, D. H. R.; Bhatnagar, N. Y.; Finet, J. P.; Motherwell, W.B. *Tetrahedron* **1986**, *42*, 3111-3122.

[36]. Nunn, M.; Sowerby, D. B.; Wesolek, D. M. *J. Organomet. Chem.* **1983**, *251*, 45-

46.

[37]. Kato, T.; Tanaka, S.; Naka, K. *Chem. Lett.* **2015**, *44*, 1476-1478.

[38]. Pritchard, B. P.; Altarawy, D.; Didier, B.; Gibson, T. D.; Windus, T. L. *J. Chem. Inf. Model.* **2019**, *59*, 4814-4820.

Chapter 2 Synthesis of Unsymmetrically Condensed Benzo- and Thienotriazolgermoles

Introduction

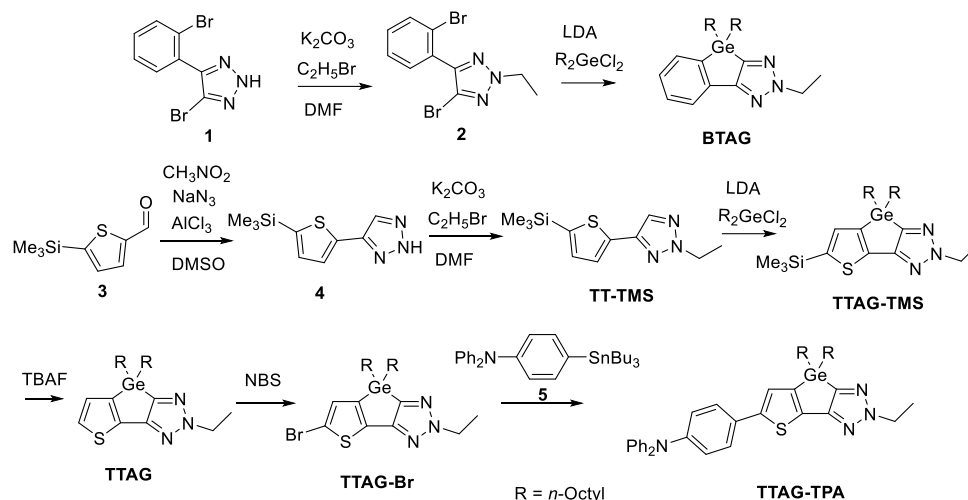
Triazoles are five-membered aromatic ring systems containing two double bonds and three sequentially arranged nitrogen atoms. In addition to their distinctive structural properties such as a high dipole moment, molecular rigidity, and promising photochemical characteristics, their excellent accessibility and ease of modification make triazoles highly appealing. Moreover, triazoles serve as Lewis bases to facilitate intermolecular interactions with Lewis acids. Triazole derivatives, therefore, constitute an important class of heterocycles for applications in pharmaceuticals [1], biologically active agents that can interact with biologically active substances through such interactions as hydrogen bonding [2]. Applications to other functional materials such as mechanochromic, photoluminescent, and fluorosensing materials [3–8] have been demonstrated. They serve also as building blocks for the synthesis of polymers, dendrimers, and other functional materials [9], including materials that can be used for solar cells [10–13], field-effect transistors [14–16], and light-emitting diodes [17–19]. Materials incorporating triazole units have been also developed for gas storage [20], gas separation [21], and optical brightening [22], and the potential utilization of these materials in sensors [23] and catalysts [24] has been explored. Triazole units are regarded as promising electron-acceptors for the construction of donor–acceptor (D–A) compounds.

Si/Ge-condensed compounds, such as siloles and germoles, have received considerable attention in recent decades for their potential applications in organic electronics [25,26]. These structures exhibit a notable phenomenon known as $\sigma^*-\pi^*$ conjugation, which is frequently observed between Si/Ge σ^* -orbitals and endocyclic butadiene π^* -orbitals. This interaction serves to stabilize the lowest unoccupied molecular orbital (LUMO), resulting in an enhanced electron affinity and reduced energy gaps between the highest occupied molecular orbital (HOMO) and LUMO [27–29]. The high planarity of siloles and germoles is also advantageous for their use

as building units of conjugated materials. These characteristics have significant implications on the electronic properties of siloles and germoles. Researchers have explored strategies to fine-tune the functionalities of these compounds to allow for tailored applications in various electronic devices via condensation with aromatic ring systems [30]. Currently, dithienosilole and dithienogermole are used as building units for preparing conjugated functional materials for optoelectronic devices, such as OLEDs [31], organic solar cells [32], and organic transistors [33]. However, most condensed siloles and germoles reported so far possess symmetrical tricyclic systems [34], and studies on unsymmetrical tricyclic systems have been limited to simple cases, such as combinations of benzene–pyridine [35,36], benzene–thiophene [37,38], and thiophene–pyridine ring systems [26]. In this work, the author designed and synthesized two types of germoles unsymmetrically condensed with benzene–triazole and thiophene–triazole units (BTAG and TTAG), with the hope that D–A interactions between benzene/thiophene and triazole units linked by a germole system would allow for the development of building units of conjugated functional materials having finely tuned electronic states. The optical and electrochemical properties of these triazolgermole derivatives were systematically investigated. The author also prepared TTAG bromide as a precursor of various TTAG-containing conjugated materials. Indeed, TTAG bromide underwent the palladium-catalyzed Stille coupling reaction to furnish triphenylamine-substituted TTAG (TTAG-TPA) with the effective extension of conjugation. The electronic states of TTAG-TPA were investigated by optical and electrochemical measurements and density functional theory (DFT) calculations. Although BTAG and TTAG showed no evident intramolecular D–A interaction, TTAG-TPA exhibited solvatochromic properties attributable to the intramolecular D–A interaction between the triphenylamine and triazole units, with a shift of the photoluminescence (PL) band toward lower energies with increasing solvent polarity. These results suggest potential applications of triazolgermole units as building units of conjugated materials.

Results and Discussion

Synthesis



Scheme 2.1. Synthesis of BTAG, TTAG, TTAG-TMS, and TTAG-TPA.

The synthetic strategy is shown in Scheme 2.1. Compound **1** was prepared following a previously reported method [39] and used for the subsequent synthesis of BTAG via compound **2**. TT-TMS was obtained by the ethyl substitution of **4** prepared from **3**. Compound **3** was prepared as previously reported [40]. The dilithiation of TT-TMS using LDA, followed by a ring-forming reaction with dichlorodi(*n*-octyl)germane, resulted in a mixture containing TTAG-TMS, unsubstituted TT-TMS, and numerous unidentified products. From the mixture, TTAG-TMS was isolated in 58% yield by silica gel column chromatography. TTAG-TMS was treated with TBAF to obtain TTAG with a yield of 85%. The bromination of TTAG with NBS gave TTAG-Br, which was further subjected to palladium-catalyzed Stille coupling with **5** to obtain TTAG-TPA.

Optical and Electrochemical Properties

The author examined the optical and electrochemical properties of the prepared triazologermylene derivatives to clarify their electronic states. The UV-vis absorption and PL spectra of BTAG, TTAG, TTAG-TMS, and TTAG-TPA in THF are shown in Figure 2.1, and the corresponding photophysical data are summarized in Table 2.1.

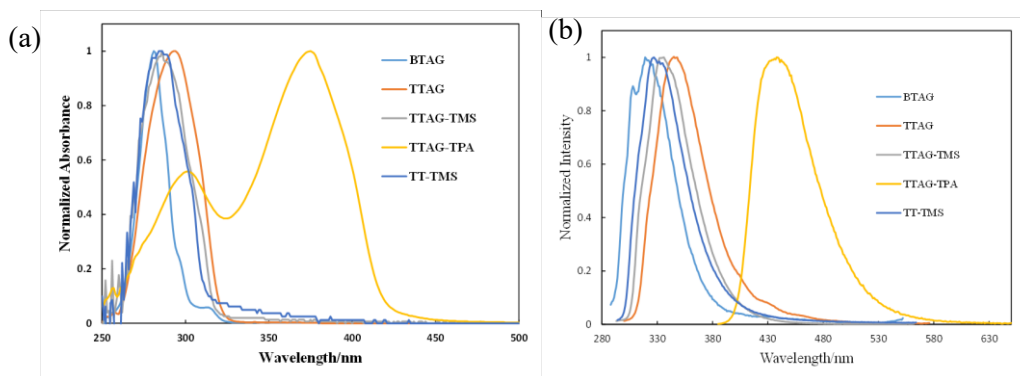


Figure 2.1. UV-vis absorption spectra (a) and PL spectra (b) of triazolgermoles in THF (1.0×10^{-5} M) at room temperature.

Table 2.1. Optical and electrochemical properties of triazolgermoles.

Compound	UV abs. λ_{\max} ^a /nm	PL λ_{\max} ^{a,b} /nm (Φ_f)	HOMO ϵ /eV	LUMO ϵ /eV	LUMO–HOMO/eV
BTAG	281	319 (nd ^c)	–6.12	–1.93	4.19
TTAG	294	348 (nd ^c)	–5.80	–1.91	3.86
TTAG-TMS	286	336 (nd ^c)	–5.84	–1.93	3.91
TTAG-TPA	300, 375	438 (38%)	–5.23	–2.26	2.97
TT-TMS	285	327 (nd ^c)	–6.04	–2.07	3.97

^a In THF at room temperature. ^b Excited at the absorption maximum. ^c Derived from CV anodic onset potential. ^d $E(\text{LUMO}) = E(\text{HOMO}) + E_g$. ^e Too low to determine.

BTAG displayed a maximum absorption at 281 nm in THF with a shoulder at 290 nm. Replacing benzene with thiophene in TTAG caused a bathochromic shift of 13 nm to give an absorption maximum at 294 nm in THF. When compared with thienopyridinogermole, the absorption maximum of TTAG was shifted to the shorter wavelength region by 6 nm, reflecting the less extended conjugation of thienyltriazole than thienylpyridine [26]. In fact, 5-trimethylsilyl-2-thienylpyridine possesses the absorption maximum at 324 nm, redshifted by approximately 40 nm compared to that of TT-TMS [26]. Silyl substitution at the α -position of the thiophene ring in TTAG-TMS shifted the absorption maximum slightly to 286 nm. This finding differed from a previous report on DTS derivatives that found a shift of absorption bands to lower energies because of a similar silyl substitution [41]. Germole condensation in TTAG-

TMS resulted in a red shift of the PL band by 9 nm relative to that of TT-TMS.

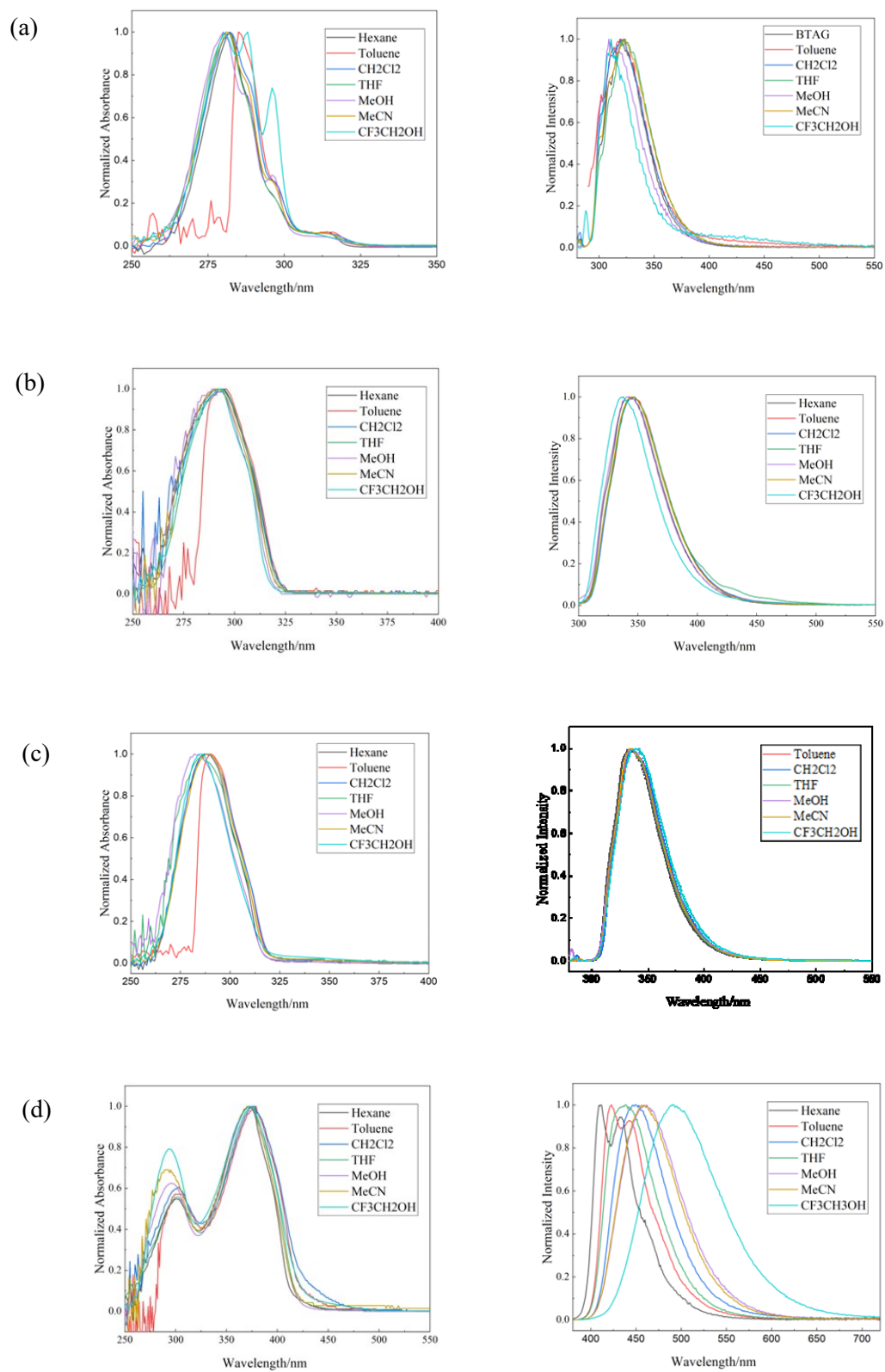


Figure 2.2. UV absorption (left) and PL spectra (right) of BTAG (a), TTAG (b), TTAG-TMS (c), TTAG-TPA (d) in several solvents.

However, despite the author expectation, their UV absorption bands were at nearly the same energies. Compounds BTAG, TTAG, and TTAG-TMS showed weak PL. Figure 2.2a–c shows the absorption spectra of BTAG, TTAG, and TTAG-TMS recorded in different solvents. Only negligible solvatochromic shifts were observed in both the UV–vis and PL spectra of these compounds, indicating the absence of evident D–A interactions. TTAG-TPA exhibited an absorption band and a PL band at 375 nm and 438 nm in THF, respectively, both of which were largely red-shifted compared with those of BTAG, TTAG, and TTAG-TMS. It is likely that the introduction of the triarylamine substituent on the thiophene ring efficiently enhanced conjugation. In the UV–vis absorption spectrum, a band at 300 nm was also observed in THF, which is possibly due to the local excitation regarding the TTAG unit.

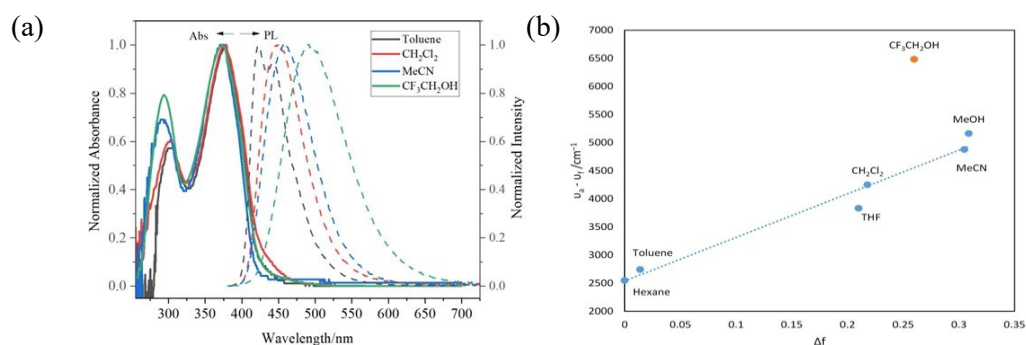


Figure 2.3. UV–vis absorption (solid line) and solvatochromic PL (dotted line) study (a) and the Lippert–Mataga plot (b) of TTAG-TPA. The slope of the fitted line is 7747 cm^{-1} ($R^2 = 0.97$)

The PL bands have intramolecular charge transfer (ICT) characteristics, which can be verified by the solvatochromic effects, as shown in Figure 2.3. For example, the PL band of TTAG-TPA was observed at 423 nm in toluene, which was bathochromically shifted to 456 nm in more polar MeCN. In contrast, the PL spectra of BTAG, TTAG, and TTAG-TMS showed no clear solvatochromism. The red shift of the PL band with increasing solvent polarity clearly indicates that the excited states were more polar than the ground state [42]. In fact, nearly no evident solvatochromic

effects were observed in the UV–vis absorption spectra of TTAG-TPA. To further investigate the ICT characteristics of TTAG-TPA, the Stokes shift ($\nu_a - \nu_f$) in each solvent was plotted as a function of its orientational polarizability Δf to obtain Lippert–Mataga plots [43,44]. A linear relationship between the Stokes shifts and orientational polarizabilities was observed (Figure 2.3 and Table 2.2). Using the slope of the Lippert–Mataga plot, the dipole moment change ($\Delta\mu$) upon photoexcitation was calculated to be 18.4 D (Figure 2.4) [26]. This was smaller than that calculated for thienopyridinogermole with the same substituents (19.9 D), suggesting that fine tuning of the D–A interaction is possible by changing the acceptor unit.

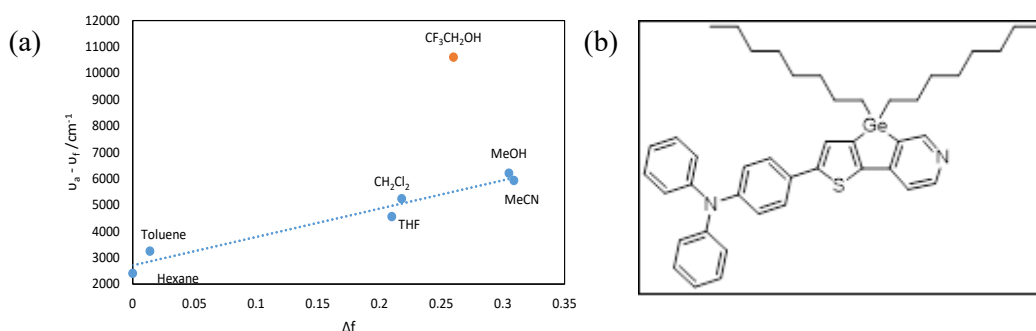


Figure 2.4. Lippert-Mataga plots (a) and the structure (b) of thienopyridinogermole. The slope for the fit is 10746 cm^{-1} ($R^2=0.96$).

Table 2.2. Absorption maxima, emission maxima and Stokes' shift of TTAG-TPA in various solvents.

Solvents	Dielectric constant (ϵ)	Refractive Index (n)	Δf	λ_a /nm	λ_f /nm	Stokes Shift/ cm^{-1}
Hexane	1.88	1.375	0	372	411	2550
Toluene	2.38	1.494	0.014	379	423	2744
CH_2Cl_2	8.93	1.421	0.218	377	449	4253
THF	7.58	1.405	0.210	375	438	3835
MeOH	32.66	1.327	0.309	373	462	5164
MeCN	35.94	1.342	0.305	373	456	4879
TFE ^a	8.55	1.300	0.260	373	492	6484

^a TFE (trifluoroethanol). The parameters from references [47] and [48].

TTAG-TPA had a higher PL quantum yield than the other triazologermole derivatives, likely reflecting the extended conjugation. TTAG-TPA exhibited blue PL in all solvents with maxima in the range of 410–490 nm, except in trifluoroethanol in which green emission was observed (Figure 2.5). Interestingly, the Stokes shift of TTAG-TPA in trifluoroethanol deviated from that predicted from the Lippert–Mataga plot of TTAG-TPA in different solvents, and the largely red-shifted PL band at 492 nm suggested a specific interaction of TTAG-TPA with trifluoroethanol. For instance, hydrogen bonding might have resulted in the complex formation of TTAG-TPA with trifluoroethanol, as previously reported for triphenylamine-substituted thienopyridinogermole [26].



Figure 2.5. Photo of TTAG-TPA in several solvents under irradiation at 365 nm at room temperature.

Anodic cyclic voltammograms (CVs) were examined to investigate the redox characteristics and HOMO energy levels of triazologermole derivatives (Table 2.1 and Figure 2.6). The oxidation peak of TTAG-TMS was found at 1.62 V (vs. Fc⁺/Fc), lower than that of TT-TMS (1.84 eV), indicating that the introduction of the germole unit raised the HOMO energy level. The oxidation peak of BTAG was observed at 1.96 V, higher than that of TTAG (1.57 V), further supporting the less extended conjugation in BTAG. The first oxidation peak (E_{0ox1}) of TTAG-TPA was much lower than that of TTAG, at 1.04 V. The HOMO energy levels determined from the onsets of the first oxidation were –6.12 eV for BTAG, –5.80 eV for TTAG, –5.84 eV

for TTAG-TMS, and -5.23 eV for TTAG-TPA. It should be noted that the introduction of the triphenylamine unit had a significant effect on the elevation of the HOMO energy level. This can be attributed to the contribution of the strong electron-donating triphenylamine group. In contrast, silyl substitution at the α position of the thiophene ring in TTAG-TMS lowered the HOMO energy level.

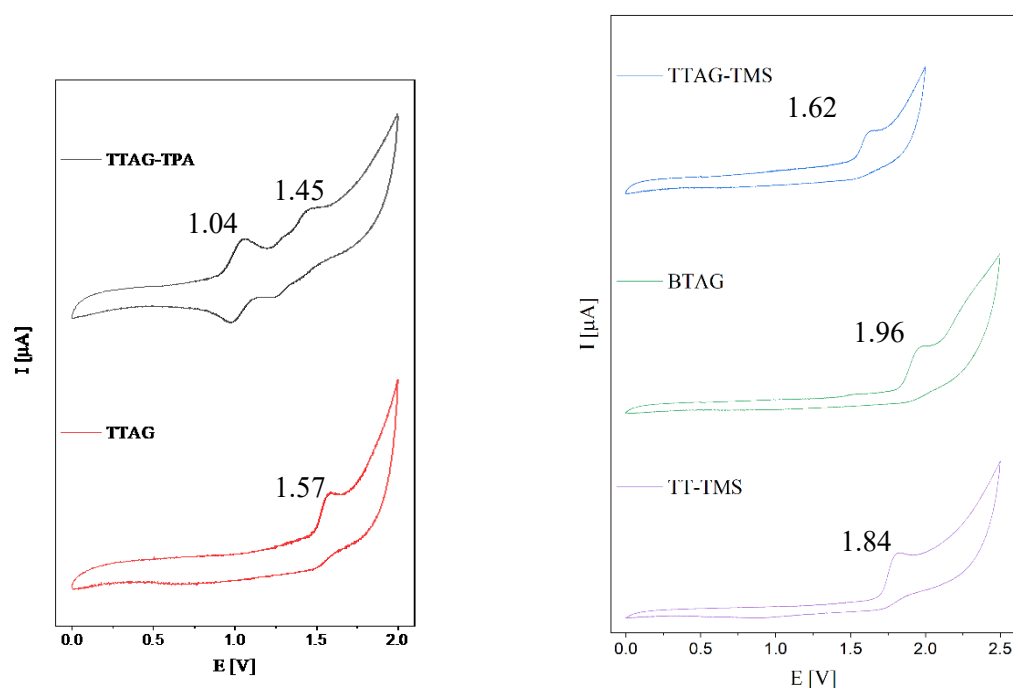


Figure 2.6. Cyclic voltammograms of BTAG, TTAG, TTAG-TMS, TTAG-TPA and TT-TMS in MeCN/TBAHFP (0.1 M), $[c] = 1 \times 10^{-4} \text{ mol L}^{-1}$, 298K, scan rate = 50 mV/ s.

DFT Calculation

To clarify the electronic states of triazolgermole derivatives, the author carried out DFT calculations using the Gaussian 16 suite of quantum chemical simulation programs for condensed germoles. First, structures were optimized in vacuo using DFT calculations at the B3LYP/6-31G(d,p) level [45]. Figure 2.7 shows the results of DFT calculations. The HOMO of BTAG is based on π -conjugation. The higher HOMO of TTAG than that of BTAG by 0.27 eV is likely due to electron donation by the thiophene unit of TTAG, which suggests the higher Lewis basicity of TTAG than BTAG. At the same time, the LUMO is lowered by 0.23 eV relative to that of BTAG.

The LUMOs of triazolgermole derivatives show $\sigma^*-\pi^*$ interaction, particularly between the thiophene β -carbon and the germanium atom. However, orbital overlapping is limited despite the author expectations, with the LUMO of TTAG-TMS being at a higher energy than that of TT-TMS. The reduced HOMO–LUMO energy gap of TTAG-TMS compared with that of TT-TMS appears to be primarily due to the electron-donating properties of the germanium unit, raising the HOMO energy level.

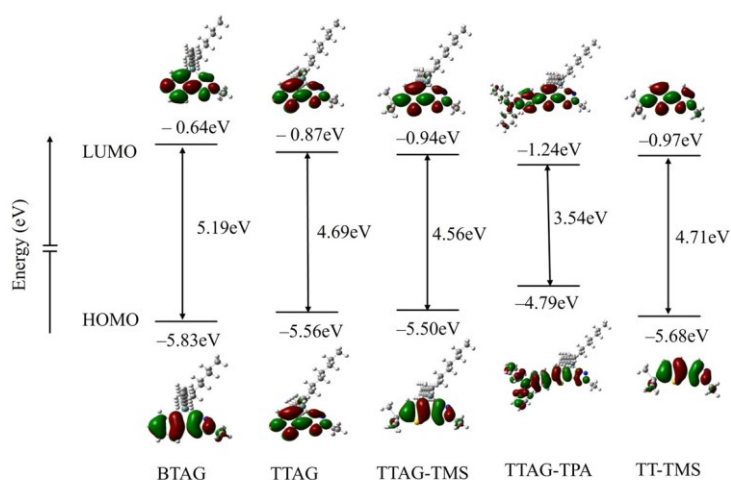


Figure 2.7. Energy levels and profiles of BTAG, TTAG, TTAG-TMS, TTAG-TPA, and TT-TMS derived from DFT calculations at the B3LYP/6-31G(d,p) level of theory in the gas phase.

The HOMO–LUMO energy gaps decreased in the order of BTAG > TT-TMS > TTAG > TTAG-TMS > TTAG-TPA, in accordance with their optical properties, except for TTAG-TMS (TTAG-TMS showed a smaller optical band gap than TTAG). The CVs showed a higher anodic potential for TTAG-TMS than for TTAG, indicating a shallower HOMO energy level. These findings are inconsistent with the results of computation, suggesting the contribution of trimethylsilyl substitution to both the HOMO and LUMO to decrease the energy gap, although the degree of contribution seemed small. Unfortunately, the author has no direct data to explain this discrepancy between the experimental and computational data for TTAG-TMS. The introduction

of the triphenylamine group to the TTAG unit affected the HOMO–LUMO energy gap in TTAG-TPA mainly by raising the HOMO energy level, rather than lowering the LUMO energy level. Indeed, the LUMO of TTAG-TPA was lower only by 0.37 eV than that of TTAG, while the HOMO was higher by 0.77 eV. In TTAG-TPA, the HOMO is mainly on the (diphenylaminophenyl)thiophene unit, whereas the LUMO is distributed more on the triazolgermole unit, suggesting that charge separation may occur in the photoexcited state. However, the separated distribution of the HOMO and LUMO was not observed in BTAG, TTAG, and TTAG-TMS. This finding is in line with the fact that the UV absorption and PL bands of these compounds exhibited no evident solvatochromic effects.

Conclusions

In conclusion, the author has synthesized triazolgermole compounds for the first time and thoroughly investigated their optical and electrochemical behaviors to elucidate the electronic states. The author's findings suggest that replacing the condensed benzene ring of BTAG with a thiophene ring enhances the conjugation, as evidenced by the red-shifted absorption of TTAG relative to that of BTAG. Contrary to the author's expectation, germole condensation raised both HOMO and LUMO energy levels, suggesting that the $\sigma^*-\pi^*$ conjugation does not play an important role in the triazolgermole system and that the germole unit serves as an electron donor, unlike conventional germole compounds such as dithienogermoles and dibenzogermoles. The author also found that bromo-substituted TTAG can be used as a potential precursor of TTAG-based conjugated compounds, and an electron-donating triphenylamine unit was introduced to the TTAG thiophene ring. The resulting TTAG-TPA showed the expected intramolecular D–A interaction, indicating that the TTAG unit can be used as an electron-accepting unit in conjugated D–A systems. Furthermore, TTAG-TPA had sufficient Lewis basicity for complex formation with trifluoroethanol, inducing a clear red shift of the PL band, suggesting potential applications of triazolgermole derivatives as sensor materials. The triazolgermole seems to be useful as an acceptor unit being applicable to donor–

acceptor compounds. Further studies to explore the applications of triazolgermole-based materials are underway.

Experimental section

General

All reactions were carried out under a dry argon atmosphere. *N,N*-dimethylformamide (DMF), dimethyl sulfoxide (DMSO) and tetrahydrofuran (THF) were distilled from CaH₂ and stored over activated molecular sieves in the dark until use as reaction solvents. Compound 5 was prepared as reported in study [46]. Nuclear magnetic resonance (NMR) spectra were recorded on a Varian 400-MR spectrometer (Palo Alto, CA, USA). UV–vis absorption and PL spectra in various solvents were recorded at room temperature using Hitachi U-2910 (Tokyo, Japan) and HORIBA FluoroMax-4 spectrophotometers (Kyoto, Japan), respectively. APCI-mass spectra were obtained with a Thermo Fisher Scientific LTQ Orbitrap XL spectrometer (Waltham, MA, USA) at N-BARD, Hiroshima University. Electrochemical redox potentials were obtained by cyclic voltammetry measurements performed with a computer-controlled Autolab analyzer (Kyoto, Japan) using a typical three-electrode electrochemical cell in a solution of tetrabutylammonium hexafluorophosphate (0.1 M) in anhydrous acetonitrile at a scan rate of 50 mV s⁻¹ at room temperature under nitrogen. A Pt disk was used as the working electrode, a Pt wire as the counter electrode, and an Ag/Ag⁺ electrode as the reference electrode. The potential of the reference electrode was calibrated with ferrocene. DFT calculations were performed using the Gaussian 16 program (Gaussian Inc., Wallingford, CT, USA). Geometrical optimization was carried out in vacuo using the B3LYP functional and the 6-31G(d,p) basis set for all atoms.

Synthesis of compound 2.

The mixture of 1 (0.303 g, 1.00 mmol), K₂CO₃ (0.138 g, 1.00 mmol), and C₂H₅Br (0.164 g, 1.50 mmol) was stirred in 15 mL of DMF at room temperature in air for 5 h. The solvent was evaporated in vacuo and the residue was chromatographed on

silica gel with EtOAc/hexane (1:5) as the eluent to give 2 in 87% yield (0.287 g, 0.87 mmol) as a white solid. ^1H NMR (400 MHz, CDCl_3) δ : 7.70 (d, $J = 8.0$ Hz, 1H), 7.42-7.37 (m, 2H), 7.34-7.28 (m, 1H), 4.51 (q, $J = 7.3$ Hz, 2H), 1.62 (t, $J = 7.3$ Hz, 3H). ^{13}C NMR (100 MHz, CDCl_3) δ : 146.2, 133.3, 132.2, 130.9, 130.5, 127.4, 124.0, 121.9, 51.2, 14.9. HR-MS (APCI) Calcd for $\text{C}_{10}\text{H}_{10}\text{Br}_2\text{N}_3$: $[\text{M} + \text{H}]^+$: 329.92360, Found: 329.92419.

Synthesis of compound 4.

A mixture of 3 (1.20 g, 6.510 mmol), nitromethane (0.596 g, 9.765 mmol), NaN_3 (0.931 g, 14.322 mmol), and AlCl_3 (0.087 g, 0.651 mmol), was stirred in 20 mL DMSO at 80 °C in air overnight. The solution hydrolyzed with brine and extracted with EtOAc. The combined organic layers were dried over anhydrous sodium sulfate, and the solvent was evaporated in vacuo. The residue was chromatographed on silica gel with EtOAc/hexane (1:2) as the eluent to give 4 in 70 % yield (1.017 g, 4.557 mmol) as a brown oil. ^1H NMR (CDCl_3) δ : 7.88 (s, 1H), 7.48 (d, $J = 3.4$ Hz, 1H), 7.23 (d, $J = 3.4$ Hz, 1H), 0.35 (s, 9H). ^{13}C NMR (100 MHz, CDCl_3) δ 141.6, 137.0, 134.8, 129.5, 126.5, 112.2, 0.0. HR-MS (APCI) Calcd for $\text{C}_9\text{H}_{14}\text{N}_3\text{SSi}$: $[\text{M} + \text{H}]^+$: 224.06722, Found: 224.06767.

Synthesis of BTAG

To a solution of 2 (0.507 g, 1.532 mmol) in 20 mL of THF, 1.915 mL of *n*-BuLi (1.6 M) in hexane at -78 °C was added, and the mixture was stirred at this temperature for 2 h. Dichlorodi(*n*-octyl)germane (0.623 g, 1.685 mmol) was added to the mixture at -78 °C. After stirring overnight at room temperature, the solvent was evaporated under reduced pressure, and the residue was directly purified by column chromatography on silica gel with EtOAc/hexane (1:10) as the eluent to give BTAG as a colorless oil in 65% yield (0.490 g, 1.042 mmol). ^1H NMR (400 MHz, CDCl_3) δ 7.79 (d, $J = 7.5$ Hz, 1H), 7.53 (d, $J = 7.1$ Hz, 1H), 7.40 (t, $J = 7.5$ Hz, 1H), 7.28-7.25 (m, 1H), 4.56 (q, $J = 7.3$ Hz, 2H), 1.62 (t, $J = 7.3$ Hz, 3H), 1.47-1.39 (m, 4H), 1.30-1.16 (m, 24H), 0.85 (t, $J = 7.0$ Hz, 6H). ^{13}C NMR (100 MHz, CDCl_3) δ 160.9, 148.6,

143.7, 138.1, 133.9, 129.6, 127.8, 121.9, 50.1, 32.9, 32.0, 29.3, 29.2, 25.4, 22.8, 15.4, 14.3, 14.2. HR-MS (APCI) Calcd for C₂₆H₄₄GeN₃: [M + H]⁺: 472.27415, Found: 472.27499.

Synthesis of TT-TMS

A mixture of 4 (0.510 g, 2.283 mmol), K₂CO₃ (0.316 g, 2.283 mmol), and C₂H₅Br (0.373 g, 3.425 mmol) was stirred in 15 mL of DMF at room temperature in air for 5 h. The solvent was evaporated in vacuo, and the residue was chromatographed on silica gel eluted with EtOAc/hexane (1:5) to give TT-TMS as a yellow oil in 78% yield (0.69 g, 1.41 mmol). ¹H NMR (400 MHz, CDCl₃) δ 7.72 (s, 1H), 7.40 (d, *J* = 3.4 Hz, 1H), 7.20 (d, *J* = 3.4 Hz, 1H), 4.49 (q, *J* = 7.3 Hz, 2H), 1.56 (t, *J* = 7.2 Hz, 3H), 0.34 (s, 9H). ¹³C NMR (100 MHz, CDCl₃) δ 142.8, 140.9, 134.7, 130.6, 125.8, 112.2, 50.2, 15.0, 0.0. HR-MS (APCI) Calcd for C₁₁H₁₈N₃SSi: [M + H]⁺: 252.09852, Found: 252.09856.

Synthesis of TTAG-TMS

TTAG-TMS was synthesized in a similar fashion to that described for BTAG using compound TT-TMS (0.39 g, 1.551 mmol) and lithium diisopropylamide (LDA) (3.179 mmol) instead of 2 and *n*-BuLi, respectively. TTAG-TMS was obtained as a yellow oil in 58% yield (0.494 g, 0.899 mmol). ¹H NMR (400 MHz, CDCl₃) δ 6.98 (s, 1H), 4.50 (q, *J* = 7.3 Hz, 2H), 1.56 (t, *J* = 7.3 Hz, 3H), 1.45–1.38 (m, 4H), 1.37–1.13 (m, 24H), 0.85 (t, *J* = 7.0 Hz, 6H), 0.28 (s, 9H). ¹³C NMR (100 MHz, CDCl₃) δ 148.19, 141.16, 140.68, 138.68, 134.11, 127.23, 49.91, 33.00, 32.04, 29.30, 29.16, 24.87, 22.80, 15.31, 14.26, 13.69, 0.01. HR-MS (APCI) Calcd for C₂₇H₅₀N₃GeSSi: [M + H]⁺: 550.27010, Found: 550.27045.

Synthesis of TTAG

To a solution of TTAG-TMS (0.287 g, 0.522 mmol) in THF (15 mL), a solution of tetra(*n*-butylammonium) fluoride (TBAF) (0.522 mmol, 1 M) in THF at 0 °C was added, and the mixture was stirred for 10 min at this temperature. After the

evaporation of the solvent, the residue was diluted with 10 mL of ether acetate and hydrolyzed with water. The organic layer was separated, washed with 3×10 mL of water, and dried over anhydrous magnesium sulfate. After the evaporation of the solvent, the residue was subjected to silica gel column chromatography with hexane/ CH_2Cl_2 (10:1) as the eluent to give TTAG as a colorless oil in 86% yield (0.214 g, 0.449 mmol). ^1H NMR (400 MHz, CDCl_3) δ 7.36 (d, $J = 4.8$ Hz, 1H), 7.11 (d, $J = 4.7$ Hz, 1H), 4.51 (q, $J = 7.3$ Hz, 2H), 1.59 (t, $J = 7.2$ Hz, 3H), 1.50–1.38 (m, 4H), 1.29–1.17 (m, 24H), 0.86 (t, $J = 7.0$ Hz, 6H). ^{13}C NMR (100 MHz, CDCl_3) δ 156.0, 150.6, 144.8, 140.9, 129.8, 126.9, 77.5, 77.2, 76.8, 49.9, 32.8, 32.0, 29.3, 29.2, 25.4, 22.8, 15.3, 14.5, 14.2. HR-MS (APCI) Calcd for $\text{C}_{24}\text{H}_{42}\text{N}_3\text{GeS}$: $[\text{M} + \text{H}]^+$: 478.23057, Found: 478.23077.

Synthesis of TTAG-Br

A mixture of TTAG (0.182 g, 0.383 mmol) and *N*-bromosuccinimide (NBS) (0.068 g, 0.383 mmol) was stirred in 15 mL of CH_2Cl_2 at room temperature in the dark. After 10 h, the reaction was quenched with water, and the resulting mixture was extracted with CH_2Cl_2 . The extracts were combined and washed with brine (2×10 mL). After drying the organic phase over anhydrous sodium sulfate, the solvent was removed under reduced pressure, and the residue was purified by column chromatography with hexane/ CH_2Cl_2 (10:1) as the eluent to give 3 as a colorless oil in 95% yield (0.202 g, 0.363 mmol). ^1H NMR (400 MHz, CDCl_3) δ 7.06 (s, 1H), 4.50 (d, $J = 7.3$ Hz, 2H), 1.59 (t, $J = 7.3$ Hz, 3H), 1.47–1.38 (m, 4H), 1.30–1.17 (m, 28H), 0.86 (t, $J = 7.0$ Hz, 3H). ^{13}C NMR (100 MHz, CDCl_3) δ : 155.8, 149.5, 145.1, 141.7, 132.5, 113.3, 50.0, 32.7, 31.9, 29.3, 29.2, 25.4, 22.8, 15.3, 14.5, 14.2. HR-MS (APCI) Calcd for $\text{C}_{24}\text{H}_{41}\text{N}_3\text{BrGeS}$: $[\text{M} + \text{H}]^+$: 556.14109, Found: 556.14136.

Synthesis of TTAG-TPA

Compounds TTAG-Br (0.13 g, 0.234 mmol) and 5 (0.084 g, 0.156 mmol) were dissolved in toluene (3 mL) that had been degassed by argon bubbling for approximately 4 h. $\text{Pd}(\text{PPh}_3)_4$ (5.41 mg, 4.68 μmol) was added and the solution was

heated to reflux with stirring for 10 h. After removal of the solvent under reduced pressure, the residue was purified by flash column chromatography (SiO₂) with hexane/CH₂Cl₂ (10:1) as the eluent to afford product TTAG-TPA as an orange oil in 40% yield (0.045 g, 0.062 mmol). ¹H NMR (400 MHz, CDCl₃) δ 7.49 (d, *J* = 8.8 Hz, 1H), 7.29–7.24 (m, 4H), 7.23 (s, 1H), 7.13–7.11 (m, 4H), 7.08–7.02 (m, 4H), 4.51 (q, *J* = 7.3 Hz, 2H), 1.59 (t, *J* = 7.2 Hz, 3H), 1.50–1.38 (m, 4H), 1.29–1.17 (m, 24H), 0.86 (t, *J* = 7.0 Hz, 6H). ¹³C NMR (100 MHz, CDCl₃) δ. 156.2, 150.2, 147.6, 147.4, 146.7, 146.2, 139.2, 129.4, 128.7, 126.7, 125.0, 124.6, 123.9, 123.2, 49.9, 32.8, 32.0, 29.3, 29.2, 25.4, 22.8, 15.3, 14.5, 14.2. HR-MS (APCI) Calcd for C₄₂H₅₅N₃GeS: [M + H]⁺: 721.33537, Found: 721.33685.

References

- [1]. Slavova, K. I.; Todorov, L. T.; Belskaya, N. B.; Palafox, M. A.; Kostova, I. P. *Recent. Pat. Anti-Cancer Drug Discov.* **2020**, *15*, 92–112.
- [2]. Zhao, S.; Liu, J.; Lv, Z.; Zhang, G.; Xu, Z. *Eur. J. Med. Chem.* **2023**, *251*, 115254.
- [3]. Lai, Q.; Liu, Q.; Zhao, K.; Shan, C.; Wojtas, L.; Zheng, Q.; Shi, X.; Song, Z. *Chem. Commun.* **2019**, *55*, 4603–4606.
- [4]. Gavlik, K. D.; Sukhorukova, E. S.; Shafran, Y. M.; Slepukhin, P. A.; Benassi, E.; Belskaya, N. P. *Dyes. Pigm.* **2017**, *136*, 229–242.
- [5]. Safronov, N. E.; Fomin, T. O.; Minin, A. S.; Todorov, L.; Kostova, I.; Benassi, E.; Belskaya, N. P. *Dyes. Pigm.* **2020**, *178*, 108343.
- [6]. Safronov, N. E.; Minin, A. S.; Slepukhin, P. A.; Kostova, I. P.; Benassi, E.; Belskaya, N. P. *Spectrochim. Acta. Part A Mol. Biomol. Spectrosc.* **2023**, *292*, 122419.
- [7]. Bozorov, K.; Zhao, J.; Aisa, H. A. *Bioorg. Med. Chem.* **2019**, *27*, 3511–3531.
- [8]. Kaur, J.; Saxena, M.; Rishi, N. *Bioconjug. Chem.* **2021**, *32*, 1455–1471.
- [9]. Johnson, J. A.; Finn, M. G.; Koberstein, J. T.; Turro, N. J. *Macromol. Rapid Commun.* **2008**, *29*, 1052–1072.
- [10]. Wang, L.; Wang, T.; Oh, J.; Yuan, Z.; Yang, C.; Hu, Y.; Zhao, X.; Chen, Y. *Chem. Eng. J.* **2022**, *442*, 136068.
- [11]. Chen, Y.; Lei, P.; Geng, Y.; Meng, T.; Li, X.; Zeng, Q.; Guo, Q.; Tang, A.; Zhong, Y.; Zhou, E. *Sci. China Chem.* **2023**, *66*, 1190–1200.

- [12]. Li, X.; Duan, X.; Liang, Z.; Yan, L.; Yang, Y.; Qiao, J.; Hao, X.; Zhang, C.; Zhang, J.; Li, Y. *Adv. Energy Mater.* **2022**, *12*, 2103684.
- [13]. Tang, Z.; Xu, X.; Li, R.; Yu, L.; Meng, L.; Wang, Y.; Li, Y.; Peng, Q. *ACS Appl. Mater. Interfaces* **2020**, *12*, 17760–17768.
- [14]. Cao, F.; Hsu, J.; Hung, K.; Cheng, Y. *Polym. J.* **2023**, *55*, 417–426.
- [15]. Torres-Moya, I.; Carrillo, J.R.; Díaz-Ortiz, A. *Chemosensors* **2021**, *9*, 267.
- [16]. Cerda-Pedro, J. E.; Hernández-Ortiz, O. J.; Vázquez- García, R. A.; García-Báez, E. V.; Gómez-Aguilar, R.; Espinosa-Roa, A.; Farfán, N. *Heliyon* **2024**, *10*, e23517.
- [17]. Stanitska, M.; Mahmoudi, M.; Pokhodylo, N.; Lytvyn, R.; Volyniuk, D.; Tomkeviciene, A.; Keruckiene, R.; Obushak, M.; Grazulevicius, J. V. *J. Org. Chem.* **2022**, *87*, 4040–4050.
- [18]. Tomkute-Luksiene, D.; Keruckas, J.; Malinauskas, T.; Simokaitiene, J.; Getautis, V.; Grazulevicius, J.V.; Volyniuk, D.; Cherpak, V.; Stakhira, P.; Yashchuk, V. *Dye. Pigm.* **2013**, *96*, 278–286.
- [19]. Cao, W.; Abdurahman, A.; Zheng, P.; Zhang, M.; Li, F. *J. Mater. Chem. C* **2021**, *9*, 6873–6879.
- [20]. Sarkhel, R.; Sahu, C.; Kumar, R.; Sangwai, J. S. *J. Environ.* **2023**, *11*, 110103.
- [21]. Wang, X.; Zhang, Y.; Chen, X.; Wang, Y.; He, M.; Shan, Y.; Li, Y.; Zhang, F.; Chen, X.; Kita, H. *Membranes* **2022**, *12*, 786.
- [22]. Huo, J.; Hu, Z.; Chen, D.; Luo, S.; Wang, Z.; Gao, Y.; Zhang, M.; Chen, H. *ACS Omega*. **2017**, *2*, 5557–5564.
- [23]. Singh, G.; George, N.; Singh, R.; Singh, G.; Sushma, K.G.; Singh, H.; Singh, J. *Appl. Organomet. Chem.* **2022**, *37*, e6897.
- [24]. Ghosh, D.; Dhibar, S.; Dey, A.; Manna, P.; Mahata, P.; Dey, B. *ChemistrySelect* **2020**, *5*, 75–82.
- [25]. Sun, W.; Adachi, Y.; Ohshita, J. *Dye. Pigm.* **2022**, *203*, 110333.
- [26]. Ohshita, J.; Sugino, M.; Ooyama, Y.; Adachi, Y. *Organometallics* **2019**, *38*, 1606–1613.
- [27]. Tamao, K.; Yamaguchi, S.; Shiozaki, M.; Nakagawa, Y.; Ito, Y. *J. Am. Chem. Soc.* **1992**, *114*, 5867–5869.
- [28]. Yamaguchi, S.; Tamao, K. *J. Chem. Soc. Dalton Trans.* **1998**, *22*, 3693–3702.
- [28]. Yamaguchi, S.; Tamao, K. *Chem. Lett.* **2005**, *34*, 2–7.
- [30]. Shimizu, M. *Main Group Strategies towards Functional Hybrid Materials*; Baumgartner, T., Jäkle, F., Eds.; Wiley: Hoboken, NJ, USA, **2018**; Chapter 7.

- [31]. Cai, Y.; Qin, A.; Tang, B. Z. *J. Mater. Chem. C* **2017**, *5*, 7375–7389.
- [32]. Lee, S.; Song, C. E.; Ryu, D. H.; Kim, J.; Kim, J.; Kang, I. *ACS Appl. Energy Mater.* **2023**, *6*, 12503–12514.
- [33]. Wang, C.; Dong, H.; Hu, W.; Liu, Y.; Zhu, D. *Chem. Rev.* **2012**, *112*, 2208–2267.
- [34]. Ohshita, J. *Org. Photonics Photovolt.* **2016**, *4*, 52–59.
- [35]. Matsuda, T.; Kadowaki, S.; Goya, T.; Murakami, M. *Org. Lett.* **2007**, *9*, 133–136.
- [36]. Shintani, R.; Misawa, N.; Takano, R.; Nozaki, K. *Chem. Eur. J.* **2017**, *23*, 2660–2665.
- [37]. Wei, B.; Zhang, D.; Chen, Y.; Lei, A.; Knochei, P. *Angew. Chem. Int. Ed.* **2019**, *58*, 15631–15635.
- [38]. Mitsudo, K.; Tanaka, S.; Isobuchi, R.; Inada, T.; Mandai, H.; Korenaga, T.; Wakamiya, A.; Murata, Y.; Suga, S. *Org. Lett.* **2017**, *19*, 2564–2567.
- [39]. Hu, Q.; Liu, Y.; Deng, X.; Li, Y.; Chen, Y. *Adv. Synth. Catal.* **2016**, *358*, 1689–1693.
- [40]. Denat, F.; Gaspard-Iloughmane, H.; Dubac, J. *Synthesis* **1992**, *1992*, 954–956.
- [41]. Ohshita, J.; Nodono, M.; Kai, H.; Watanabe, T.; Kunai, A.; Komaguchi, K.; Shiotani, M.; Adachi, A.; Okita, K.; Harima, Y. *Organometallics* **1999**, *18*, 1453–1459.
- [42]. Yao, L.; Zhang, S.; Wang, R.; Li, W.; Shen, F.; Yang, B. *Angew. Chem. Int. Ed.* **2014**, *53*, 2119–2123.
- [43]. Mataga, N.; Kai, Y.; Koizumi, M. *Bull. Chem. Soc. Jpn.* **1956**, *29*, 465–470.
- [44]. Vázquez, M.E.; Blanco, J.B.; Imperiali, B. *J. Am. Chem. Soc.* **2005**, *127*, 1300–1306.
- [45]. Foresman, J.B.; Frisch, A. *Exploring Chemistry with Electronic Structure Methods*, 3rd ed.; Gaussian, Inc.: Wallingford, CT, USA, **2015**.
- [46]. Qian, G.; Dai, B.; Luo, M.; Yu, D.; Zhan, J.; Zhang, Z.; Ma, D.; Wang, Z. *Chem. Mater.* **2008**, *20*, 6208–6216.
- [47]. Lide, D.R. CRC Handbook of Chemistry and Physics, 87th ed Editor-in-Chief: David R. Lide (National Institute of Standards and Technology). *J. Am. Chem. Soc.* **2006**, *129*, 724.
- [48]. Pandey, N.; Tewari, N.; Pant, S.; Mehata, M. S. *Spectrochim. Acta. Part A Mol. Biomol. Spectrosc.* **2022**, *267*, 120498.

Chapter 3 Preparation of Dithieno[3,2-*b*:4,5-*c'*]germole and Its Application as a Donor Unit in Conjugated D-A Oligomers

Introduction

Functional organic π -conjugated molecules have garnered significant attention because of their wide range of applications, including the use in optoelectronic devices. Group 14 metalloles have been extensively studied as core structures of conjugated functional materials. [1] For example, conjugated oligomers and polymers containing silole units, such as poly(silole)s, are anticipated to exhibit effective conjugation, making them suitable for both n- and p-type semiconductor materials depending on the substituents. [2] This is explained by the low-lying LUMO energy levels due to σ^* - π^* orbital interactions and high planarity of the silole system. Dithienosilole is a typical silole-containing building block that is used for the development of conjugated organic materials. [3-6] However, most research activities have focused on symmetrically condensed dithienosiloles, and less is known for unsymmetrical dithienosiloles. [7-9] H. Wang and coworkers have prepared dithieno[2,3-*b*:4,5-*c'*]silole derivatives and prepared conjugated polymers using them as the monomers (Chart 3.1a). [8,9] In this unsymmetrical unit, one thiophene ring can be incorporated into conjugated oligomeric and polymeric systems and the introduction of a functional group (R) on the other thiophene ring enables fine-tuning of the electronic state of the dithienosilole unit. Meanwhile, within the same family as silicon, germanium-based congeners known as dithienogermoles are relatively underexplored despite exhibiting properties that are comparable to or even superior to those of their Si analogs, arising from their relatively strong intermolecular interactions. [10-13]. Furthermore, dithienogermoles generally demonstrate higher stability than dithienosiloles. [14] Therefore, the exploration of unsymmetrical dithienogermoles as a promising building block for the development of functional organic optoelectronic device materials would facilitate the efficient construction of germole-containing conjugated oligomers and polymers and have significant implications.

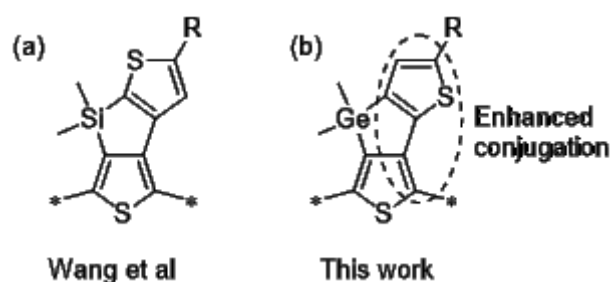
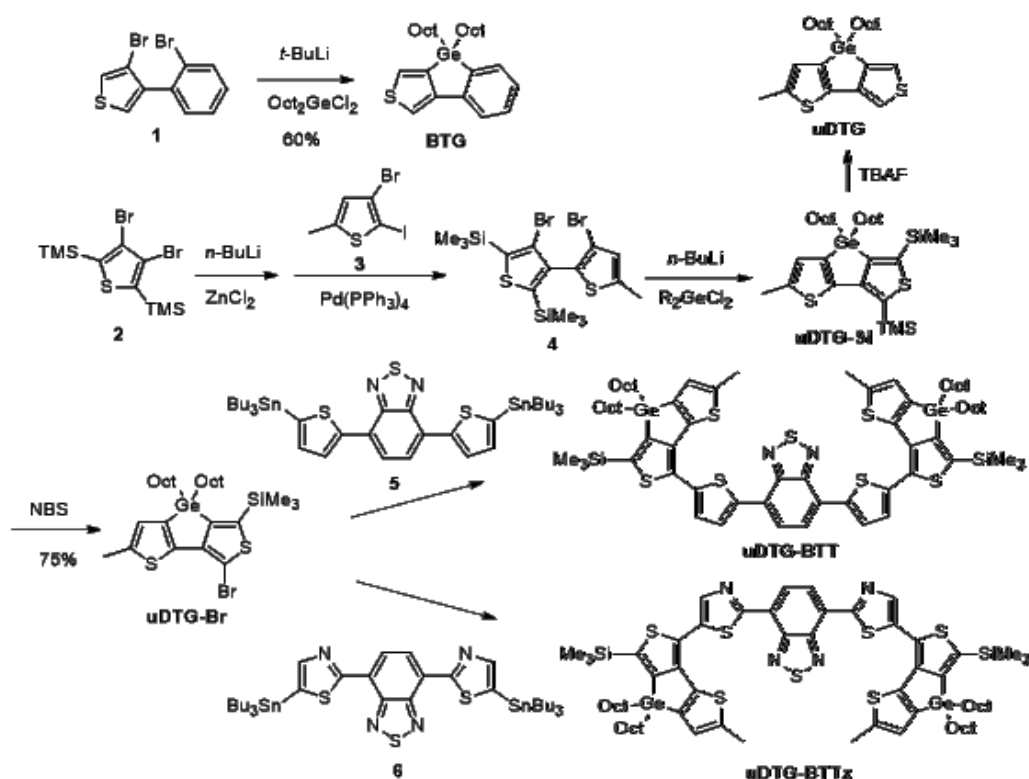


Chart 3.1. Structures of dithieno[2,3-b:4,5-c']silole (a) and dithieno[3,2-b:4,5-c']germole (b) where asterisks indicate potential junctions to conjugated systems.

In the course of the author's studies concerning unsymmetrically condensed metalloles, [15,16] the author prepared dithieno[3,2-b:4,5-c']germole (uDTG) as the first example of group 14 dithieno[3,2-b:4,5-c']metalloles. The author anticipates that uDTG would show enhanced conjugation compared with the dithieno[2,3-b:4,5-c']siloles (Chart 3.1), hereby paving the way for the development of building units of conjugated functional materials having finely tuned electronic states. The author also prepared benzo[4,5]thieno[2,3-c]germole (BTG). The optical and electrochemical properties of these thiophene-condensed unsymmetrical germole derivatives were investigated and discussed with the help of quantum chemical calculations. To explore the usefulness of uDTG as the building unit of conjugated oligomers and polymers, the author synthesized two donor-acceptor (D-A) oligomers possessing uDTG as the donor and benzo(2,1,3)thiadiazole (BT) as the acceptor, which were linked by thiophene or thiazole units. These oligomers showed clear solvatochromic behavior arising from their intramolecular D-A interaction, and their photoluminescence (PL) bands shifted to lower energies as the solvent polarity increased. The compounds described herein are expected to shed light on the design and application of new building blocks of conjugated oligomers and polymers.

Results and Discussion

Synthesis



Scheme 3.1. Synthesis of unsymmetrically condensed thienogermoles.

The synthetic strategy for unsymmetrically condensed benzothieno- and dithienogermoles is presented in Scheme 3.1. Compound 1 that was prepared following the previously reported method [17] was used for the synthesis of BTG. For the formation of uDTG derivatives, compound 4 was first obtained by a Negishi cross-coupling reaction of compounds 2 and 3 in 50 % yield. [18, 19] Dilithiation of 4 by *n*-BuLi, followed by a ring-forming reaction with dichlorodi(*n*-octyl)germane, furnished a mixture from which uDTG-Si was isolated in 65% yield by preparative gel permeation chromatography (GPC). uDTG-Si was then treated with tetrabutylammonium fluoride (TBAF) to give desilylation product uDTG in 85% yield. Bromination of uDTG-Si with NBS gave uDTG-Br in 75% yield. This compound was further subjected to palladium-catalyzed Stille coupling with 5 and 6

to provide uDTG-BTT and uDTG-BTTz as dark red solids in 30% and 20% yields, respectively. The low yields of these compounds were due to the low reactivity of the starting materials and difficulty in purification. The author found that the starting materials remained in the reaction mixtures by NMR spectral analysis.

Optical and Electrochemical Measurements

The author examined the optical and electrochemical properties of this prepared BTG and uDTS derivatives to clarify their electronic states. The UV-vis absorption spectra of BTG, uDTG, uDTG-Si, uDTG-BTT, and uDTG-BTTz in dichloromethane are shown in Figure 3.1a, and the corresponding photophysical data are summarized in Table 3.1.

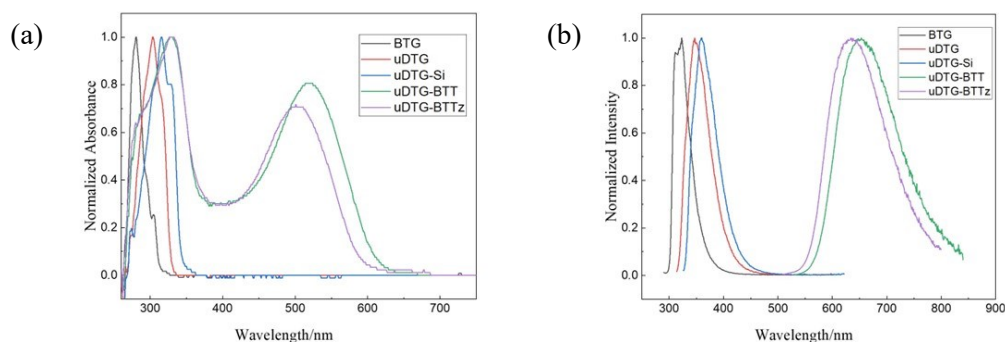


Figure 3.1. UV-vis absorption spectra (a) and PL spectra (b) of unsymmetrically condensed thienogermoles in dichloromethane (1.0×10^{-5} M) at room temperature.

As shown in Figure 3.1a, BTG displayed an absorption maximum at 280 nm. Upon replacing the condensed benzene ring of BTG with a thiophene ring, an absorption maximum appeared at 303 nm with a bathochromic shift of 23 nm for uDTG. A further bathochromic shift was observed for uDTG-Si, giving an absorption maximum at 315 nm. Their PL spectra showed similar bathochromic shifts as presented in Figure 3.1b, and Table 3.1. These bathochromic shift from BDG to uDTG is in agreement with that observed for symmetrically condensed dibenzo and dithienosiloles (DBG and DTG in Chart 3.2). [20,21] However, the fact that the absorption band of uDTG-Si appeared at higher energy than that of uDTG differed

from a previous report on DTG derivatives that showed a bathochromic shift of absorption band by similar silyl substitution (DTG-Si in Chart 3.2), [22] although the reason remains unknown. Hypsochromic shifts of the absorption bands of uDTG derivatives relative to those of the symmetrically condensed DTG analogs [20-22] are likely due to the less extended π -conjugation of α,β -linked bithiophene units in uDTG and uDTG-Si compared with the α,α -linked bithiophene unit in DTG and DTG-Si.

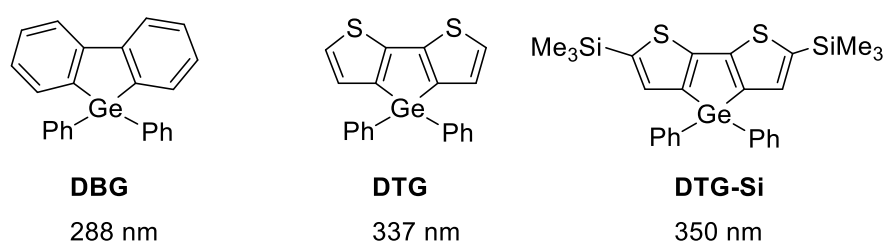


Chart 3.2. UV-vis absorption maxima for symmetrically condensed germoles in the literature.

Table 3.1. Optical and electrochemical properties of thiophene germoles.

Compound	UV abs. $\lambda_{\max}^a/\text{nm}$	PL $\lambda_{\max}^{a,b}/\text{nm}$ (Φ_f)	HOMO ^c /eV	LUMO ^d /eV	LUMO- HOMO ^e /eV
BTG	280	323 (< 2%)	-6.27	-2.31	3.96
uDTG	303	347 (3.8%)	-5.50	-1.73	3.77
uDTG-Si	315	360 (< 2%)	-5.52	-1.90	3.62
uDTG-BTT	329, 520	653 (33%)	-5.08	-3.04	2.04
uDTG-BTTz	331, 501	634 (41%)	-5.16	-3.05	2.11

^a In dichloromethane at room temperature. ^b Excited at the absorption maximum.

^c Derived from CV anodic onset potential. ^d $E(\text{LUMO}) = E(\text{HOMO}) + E_g$. ^e Optical band gap (E_g).

D–A interaction was noted in uDTG-BTT and uDTG-BTTz, which are composed of uDTG and BT units as the donor and acceptor units, respectively, linked by thiophene or thiazole units. The UV-vis absorption spectra of these compounds

showed two $\pi-\pi^*$ transition bands around 330 nm and 500 nm. The former is ascribable to the local excitation, whereas the latter is likely based on the D–A interaction that leads to photoexcited intramolecular charge transfer (ICT). The maximal absorption peaks in the low energy region were observed at 520 nm and 501 nm for uDTG-BTT and uDTG-BTTz, respectively. The blue-shifted absorption maximum of uDTG-BTTz from that of uDTG-BTT is explained by less extended conjugation of thiazole than thiophene. [23, 24] The optical band gaps of the unsymmetrically condensed thienogermoles were estimated from the absorption edges, decreasing in the order of BTG > uDTG-Si > uDTG > uDTG-BTTz > uDTG-BTT as shown in Table 3.1

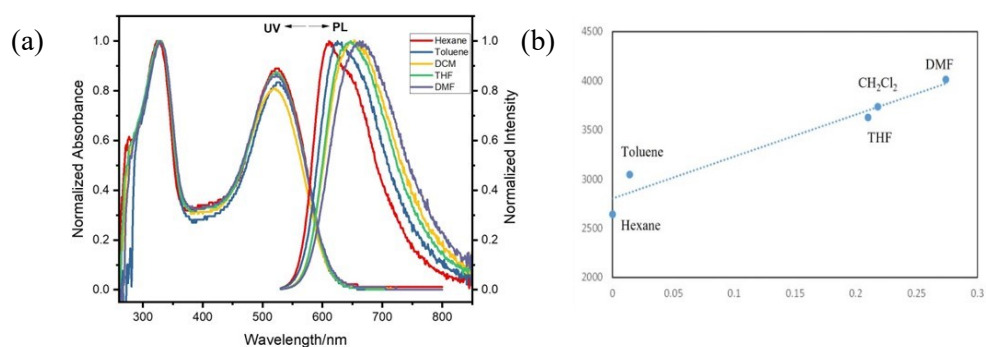


Figure 3.2. UV absorption (solid line) and PL spectra (dotted line) in different solvents (a) and the Lippert-Mataga plots (b) of uDTG-BTT. The slope of the fitted line with a slope of 4266 cm^{-1} ($R^2 = 0.95$).

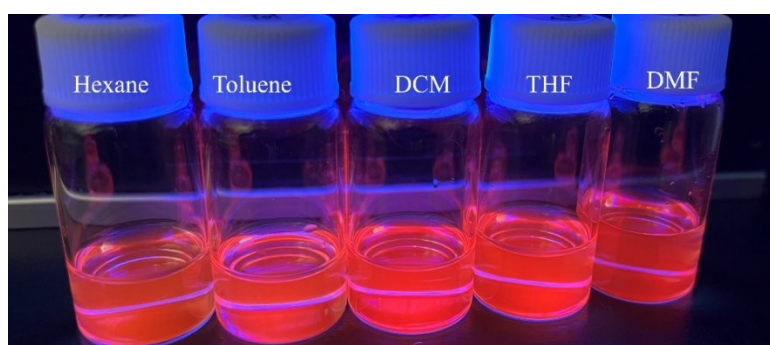


Figure 3.3. Photo of uDTG-BTT in several solvents under 365 nm at room temperature.

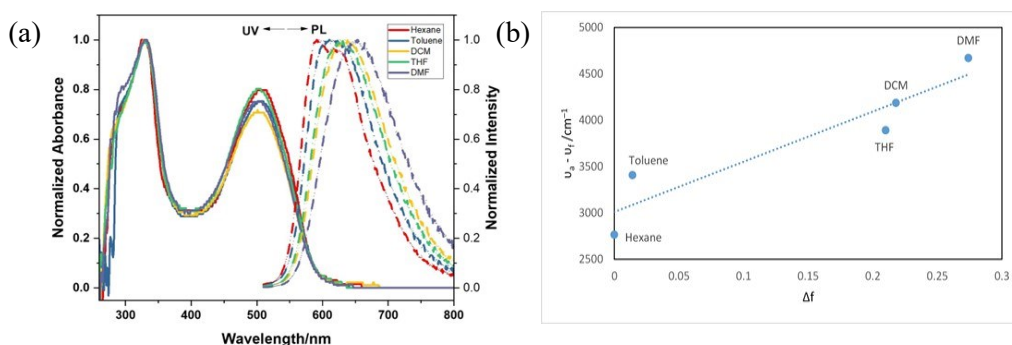


Figure 3.4. UV absorption (solid line) and PL spectra (dotted line) study (a) and the Lippert-Mataga plot (b) of uDTG- BTTz. The slope of the fitted line is 5405 cm^{-1} ($R^2=0.87$).

Table 3.2. Absorption maxima, emission maxima and Stokes' shift of uDTG-BTT and uDTG-BTTz in various solvents.

Solvents	Δf	uDTG-BTT			uDTG-BTTz		
		λ_a /nm	λ_f /nm	Stokes Shift/cm ⁻¹	λ_a /nm	λ_f /nm	Stokes Shift/cm ⁻¹
Hexane	0	526	611	2644	508	591	2764
Toluene	0.014	525	625	3047	505	610	3408
CH ₂ Cl ₂	0.218	521	647	3737	501	634	4187
THF	0.210	524	647	3628	504	627	3892
DMF	0.309	523	662	4014	501	654	4670

Monomeric compounds BTG, uDTG, and uDTG-Si showed the PL bands at 323-360 nm with low PL efficiencies. In contrast, oligomers uDTG-BTT and uDTG-BTTz exhibited strong PL bands at 653 nm and 634 nm, respectively. To understand the ICT behaviors of uDTG-BTTz and uDTG-BTT, the PL spectra were measured in different solvents and the results are shown in Figures 3.2, 3.3, and 3.4, and Table 3.2. The PL band shifted to the longer wavelength region with increasing solvent polarity, clearly indicating that the photoexcited states of uDTG-BTT and uDTG-BTTz were more polar than their respective ground states, reflecting the ICT behavior. From the slope of the Lippert-Mataga plot, the dipole moment changes ($\Delta\mu$) were estimated to be 13.03

D and 15.57 D for uDTG-BTT and uDTG-BTTz, respectively.

HOMO and LUMO energy levels of conjugated materials are important parameters for their electronic applications. Cyclic voltammograms (CV) were performed in a typical three-electrode electrochemical cell with Pt as the working electrodes in water-free acetonitrile with a scan rate of 50 mV s^{-1} (Figure 3.5) to determine the energy levels. The HOMO energy levels determined from the onsets of the first oxidation peaks are -6.27 eV for BTG, -5.50 eV for uDTG, and -5.52 eV for uDTG-Si. uDTG-BTTz possessed a lower HOMO energy level than uDTG-BTT owing to the more electron-deficient nature of thiazole than thiophene. [23, 24] The LUMO energy levels of the compounds were calculated from the anodic onsets and optical band gaps as listed in Table 3.1. The HOMO and LUMO of uDTG-BTT are at -5.08 eV and -3.04 eV , whereas those of uDTG-BTTz are at -5.16 eV and -3.05 eV , providing similar bandgaps of 2.04 and 2.11 eV, respectively.

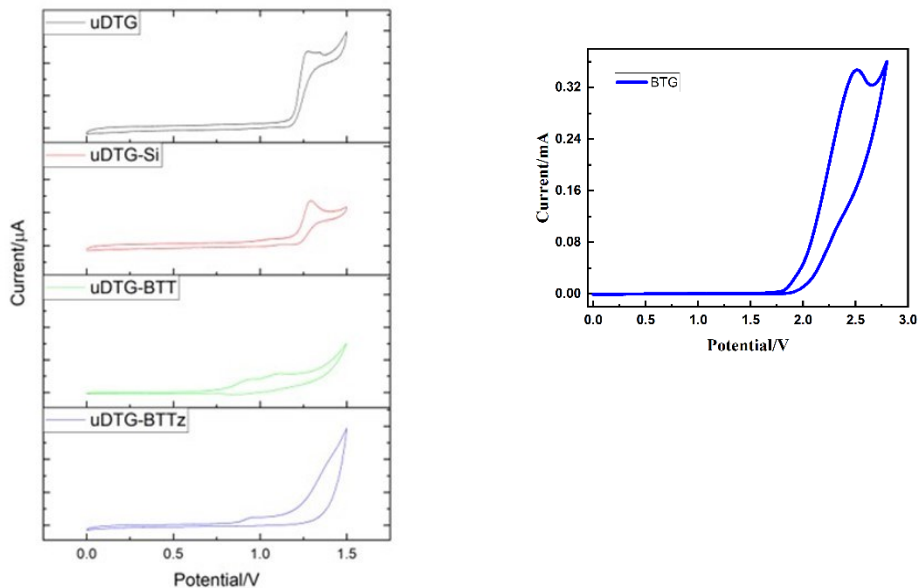


Figure 3.5. Cyclic voltammograms of BTG, uDTG, uDTG-Si, uDTG-BTT, and uDTG-BTTz in DCM/TBAHFP (0.1 M), $[c] = 1 \times 10^{-4} \text{ mol L}^{-1}$, 298K, scan rate = 50 mV s^{-1} .

Quantum Chemical Calculations

To obtain further insight into the effects of molecular structure and electron distribution on the spectroscopic and electrochemical properties of these compounds, their electronic structures were investigated with Gaussian 16 suite of quantum chemical simulation programs. The structures were optimized in vacuo using DFT calculations at the B3LYP/6-31G(d,p) level of theory. The visualized HOMO and LUMO distributions and the calculated their energy levels are shown in Figure 3.6. During the calculations, the compounds were optimized, where octyl chains on the germanium atom were replaced with methyl groups to simplify the calculations.

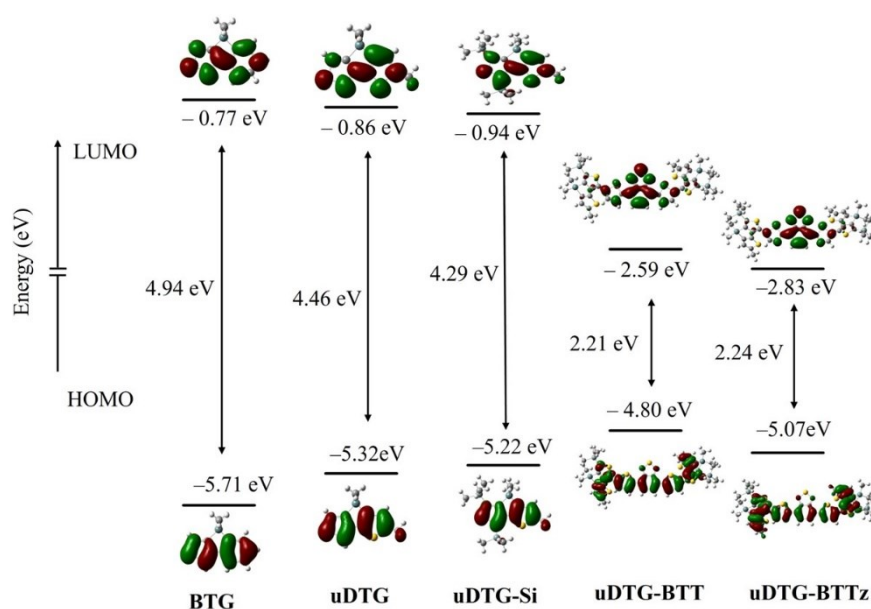


Figure 3.6. Energy levels and profiles of BTG, uDTG, uDTG-Si, uDTG-BTT, and uDTG-BTTz derived from DFT calculation at B3LYP/6-31G(d,p) level of theory in the gas phase, with alkyl chains replaced by methyl groups to simplify the calculations.

The orbital levels of the small molecules were in good agreement with the experimental data, except that calculations predicted a higher HOMO energy level and a smaller HOMO–LUMO gap for uDTG-Si than for uDTG. These differ from the

experimental data that uDTG-Si showed the anodic onset at a higher potential and the absorption band at a higher energy than uDTG, although the difference was not large. The LUMO/HOMO energy levels of DTG-containing oligomers uDTG-BTT and uDTG-BTTz were estimated to be $-2.59/-4.80$ and $-2.83/-5.07$, respectively. Both the HOMO and LUMO of uDTG-BTT lie at the higher levels than those of uDTG-BTTz, agreeing with the experimental data. The LUMOs of these oligomers are mainly found in the acceptor BT units, whereas the HOMOs are distributed in the uDTG fragments, as shown in Figure 3.6. This result indicates that ICT occurs from the uDTG donor to the BT acceptor upon photoexcitation. It is interesting to see that the thiophene and thiazole linkers also affect the HOMO and LUMO energy levels to make their fine-tuning possible.

Conclusion

The author has synthesized unsymmetrically condensed benzothienogermole BTG and dithienogermole uDTG and thoroughly investigated their optical and electrochemical properties. DFT calculations have been also carried out. Replacing the benzene ring in BTG with a thiophene ring changes the electronic states to enhance conjugation in uDTG derivatives. We have also explored the potential application of uDTG as a donor unit in conjugated D–A materials by synthesizing D–A oligomers uDTG-BTT and uDTG-BTTz featuring the combination with a benzothiadiazole acceptor unit. uDTG-BTT and uDTG-BTTz exhibited extended conjugation and clear solvatochromic behavior arising from their intramolecular D–A interaction. These results indicate the potential application of the dithieno[3,2-b:4,5-c']germole unit as an electron donor in D–A systems. Studies on the preparation of D–A materials based on the uDTG system including conjugated polymers are in progress, the results of which will be reported elsewhere.

Experimental section

General

All reactions were carried out under dry argon atmosphere. Tetrahydrofuran

(THF) and diethyl ether that were used as the reaction solvents were distilled from CaH₂ and stored over activated molecular sieves in the dark until use. Compounds 1, 2, 3, 5 and 6 were prepared as reported in the literature [17-19, 25, 26]. All other chemicals employed were commercially available and were used as received. Nuclear magnetic resonance (NMR) spectra were recorded on a Varian 400-MR spectrometer. UV-vis absorption and PL (photoluminescence) spectra were measured on Hitachi U-2910 and HORIBA FluoroMax-4 spectrophotometers, respectively. APCI-mass spectra were obtained by a Thermo Fisher Scientific LTQ Orbitrap XL spectrometer at N-BARD, Hiroshima University. Electrochemical redox potentials were obtained by cyclic voltammetry (CV) measurements, which were performed with a computer-controlled Autolab analyzer using a typical three-electrode electrochemical cell in a solution of tetrabutylammonium hexafluorophosphate (0.1 M) in anhydrous acetonitrile at a scan rate of 50 mV s⁻¹ at room temperature under nitrogen. Pt disk was used as the working electrode, a Pt wire as the counter electrode, and an Ag/Ag⁺ electrode as the reference electrode. The potential of the reference electrode was calibrated with ferrocene. DFT calculations have been performed using the Gaussian 16 program (Gaussian Inc.). [27] Geometrical optimization was carried out in vacuo using the B3LYP functional and standard 6-31G (d,p) basic set for all atoms.

Synthesis of BTG.

To a solution of 1 (0.416 g, 1.308 mmol) in diethyl ether (10 mL) was added *t*-BuLi (1.6 M in pentane, 3.27 mL, 5.232 mmol) at -78 °C. After the solution was stirred at this temperature for 2 h, dichlorodi(*n*-octyl)germane (0.508g 1.373 mmol) dissolved in 5 mL of ether was added dropwise. The reaction mixture was then stirred at room temperature overnight. After being quenched with H₂O (20 mL), the reaction mixture was extracted with CHCl₃ (3 × 20 mL) and the extract was dried over anhydrous magnesium sulfate. After evaporation of the solvent, the residue was subjected to preparative GPC eluting with toluene to give 0.388 g (65% yield) of BTG as a colorless oil. ¹H NMR (400 MHz, CDCl₃) δ 7.68 (d, *J* = 8.0 Hz, 1H), 7.53 (d, *J* = 7.2 Hz, 1H), 7.48 (d, *J* = 2.2 Hz, 1H), 7.37 –7.32 (m, 1H), 7.33 (d, *J* = 2.2 Hz, 1H),

7.22 – 7.17 (m, 1H), 1.47 – 1.43 (m, 4H), 1.28 – 1.19 (m, 24H), 0.86 (t, $J = 7.2$ Hz, 6H). ^{13}C NMR (100 MHz, CDCl_3) δ : 152.8, 144.8, 143.2, 141.4, 134.0, 129.3, 128.6, 126.7, 122.3, 115.0, 33.1, 32.0, 29.4, 29.3, 25.5, 22.8, 14.9, 14.3. HR-MS (APCI) Calcd for $\text{C}_{26}\text{H}_{41}\text{Ges}$: $[\text{M} + \text{H}]^+$: 459.21353, Found: 459.21353.

Synthesis of compound 4.

To a solution of 2 (0.775 g, 2.006 mmol) in 20 mL of THF was added 1.25 mL of *n*-BuLi (1.6M, 2.006 mmol) in hexane at -78 °C, and the mixture was stirred in this temperature for 1 hours. Zinc chloride (2.4 mL, 2.407 mmol, 1M,) was added to the reaction solution and further stirred at -78 °C for 1h. Then, the reaction mixture was warmed to room temperature. After 1h stirring, 3 (0.607g, 2.006mmol) and $\text{Pd}(\text{PPh}_3)_4$ (0.116g, 0.1003mmol) were added and the mixture was heated at 80 °C overnight. The solvent was evaporated under reduced pressure and the residue was directly purified by column chromatograph on silica gel with hexane as the eluent to give 4 in 65% yield (0.629 g, 1.304 mmol) as white solid, mp $89.6 - 90.8$ °C. ^1H NMR (400 MHz, CDCl_3) δ 6.73 (s, 1H), 2.50 (s, 3H), 0.42 (s, 9H), 0.17 (s, 9H). ^{13}C NMR (100 MHz, CDCl_3) δ 146.77, 142.49, 141.28, 140.88, 139.60, 128.13, 122.70, 111.91, 15.67, -0.10, -0.68. HR-MS (APCI) Calcd for $\text{C}_{15}\text{H}_{22}\text{Br}_2\text{S}_2\text{Si}_2$: $[\text{M}]^+$: 479.90682, Found: 479.90671.

Synthesis of uDTG-Si.

To a solution of 4 (0.500 g, 1.036 mmol) in 20 mL of THF was added of *n*-BuLi (1.6 M in hexane, 1.328 mL, 2.124 mmol) at -78 °C, and the mixture was stirred at this temperature for 2 h. Dichlorodi(*n*-octyl)germane (0.421 g, 1.139 mmol) was added to the mixture at -78 °C. After stirring the mixture overnight at room temperature, the solvent was evaporated under reduced pressure and the residue was directly purified by preparative GPCeluting with toluene to give uDTG-Si in 65% yield (0.249 g, 0.673 mmol) as a colorless oil. ^1H NMR (400 MHz, CDCl_3) δ 6.71 (s, 1H), 2.54 (s, 3H), 1.41 – 1.33 (m, 4H), 1.25 – 1.18 (m, 24H), 0.86 (t, $J = 7.2$ Hz, 6H), 0.48 (s, 9H), 0.33 (s, 9H). ^{13}C NMR (100 MHz, CDCl_3) δ 154.77, 154.56, 147.72,

147.06, 146.09, 140.98, 131.40, 128.02, 33.08, 31.97, 29.37, 29.23, 25.76, 22.81, 16.16, 15.59, 14.25, 0.81, 0.35. HR-MS (APCI) Calcd for $C_{31}H_{57}GeS_2Si_2$: $[M + H]^+$: 623.26465, Found: 623.26624.

Synthesis of uDTG.

To a solution of uDTG-Si (0.287 g, 0.642 mmol) in THF (15 mL) was added a solution of TBAF (0.642 mmol, 1 M) in THF at 0 °C and the mixture was stirred for 10 min at this temperature. After evaporation of the solvent, the residue was diluted with 10 mL of ether acetate and was hydrolyzed with 3×10 mL water. The organic layer and the extracts were combined and dried over anhydrous magnesium sulfate. The residue was subjected to preparative GPC to give uDTG as a colorless oil (0.275 g, 0.578 mmol). 1H NMR (400 MHz, $CDCl_3$) δ 7.21 (d, $J = 2.2$ Hz, 1H), 7.04 (d, $J = 2.2$ Hz, 1H), 6.70 (s, 1H), 2.52 (s, 3H), 1.47 – 1.41 (m, 4H), 1.33 – 1.20 (m, 20H), 1.17 – 1.10 (m, 4H), 0.87 (t, $J = 7.0$ Hz, 6H). ^{13}C NMR (100 MHz, $CDCl_3$). δ 146.72, 146.26, 145.83, 143.85, 141.02, 128.10, 127.97, 112.08, 32.95, 32.02, 29.37, 29.30, 25.56, 22.81, 15.65, 15.20, 14.22. HR-MS (APCI) Calcd for $C_{25}H_{41}GeS_2$: $[M + H]^+$: 479.18560, Found: 479.18591.

Synthesis of uDTG-Br.

A mixture of uDTG-Si (0.425 g, 0.683 mmol) and NBS (0.122 g, 0.683 mmol) in 15 mL THF was stirred at 0 °C in dark. After 4h, the reaction was quenched with water, and extracted with CH_2Cl_2 . The organic layer and the extract were combined and washed with a saturated NaCl aqueous solution (2×10 mL). After organic phase was dried over anhydrous sodium sulfate and the solvent was removed under reduced pressure, the residue was purified by silica gel column chromatography with hexane as the eluent to give uDTG-Br as yellow oil in 95% yield (0.228 g, 0.363 mmol). 1H NMR (400 MHz, $CDCl_3$) δ 6.75 (s 1H), 2.54 (s, 3H), 1.38 – 1.33 (m, 4H), 1.27 – 1.16 (m, 24H), 0.87 (t, $J = 7.0$ Hz, 6H), 0.31 (s, 9H). ^{13}C NMR (100 MHz, $CDCl_3$) δ 152.76, 147.66, 146.55, 146.33, 144.37, 142.47, 127.81, 104.57, 33.00, 31.96, 29.86, 29.34, 25.58, 22.65, 16.37, 15.65, 14.25, 0.43. HR-MS (APCI) Calcd for

$C_{28}H_{48}BrGeS_2Si$: $[M + H]^+$:627.13564, Found: 629.13599.

Synthesis of uDTG-BTT.

uDTG-Br (14.5 mg, 0.023mmol) and 5 (10.14 mg, 0.016 mmol) were dissolved in toluene (4 mL) that had been degassed by argon bubbling for approximately 4 h. $Pd_2(dba)_3$ (0.42 mg, 0.46 μ mol) and $P(o\text{-tolyl})_3$ (0.56 mg, 1.84 μ mol) were added to the solution and the solution was heated to reflux with stirring for 3 days. After removal of the solvent under reduced pressure, the crude product was purified by GPC to afford product uDTG-BTT (6.7 mg, 0.048 mmol, 30%) as dark red solid. 1H NMR (400 MHz, $CDCl_3$) δ 8.20 (d, $J = 3.9$ Hz, 2H), 7.92 (s, 2H), 7.49 (d, $J = 3.9$ Hz, 2H), 6.71 (s, 2H), 2.46 (s, 6H), 1.44 – 1.37 (m, 8H), 1.32 – 1.11 (m, 48H), 0.87 (t, $J = 7.0$ Hz, 12H), 0.36 (s, 18H). ^{13}C NMR (100 MHz, $CDCl_3$) δ 152.82, 148.40, 147.65, 146.54, 146.33, 145.17, 144.37, 142.47, 139.52, 136.62, 128.85, 128.67, 127.84, 126.01, 104.57, 32.99, 31.95, 29.84, 29.33, 25.56, 22.63, 16.37, 15.65, 14.25, 0.42. HR-MS (FD) Calcd for $C_{70}H_{100}Ge_2N_2S_7Si_2$: $[M]^+$: 1396.38881, Found: 1396.38577.

Synthesis of uDTG-BTTz.

uDTG-BTTz was synthesized in a similar fashion to that described for uDTG-BTT above, using compound 6 (29.93 mg, 0.034 mmol) instead of compound 5. uDTG-BTTz was obtained as dark red solid in 20% yield (0.95 mg, 0.68 μ mol). 1H NMR (400 MHz, $CDCl_3$) δ 8.85 (s, 2H), 8.29 (s, 2H), 6.72 (s, 2H), 2.54 (s, 6H), 1.41 – 1.35 (m, 8H), 1.28 – 1.19 (m, 48H), 0.86 (t, $J = 7.0$ Hz, 12H), 0.34 (s, 18H). ^{13}C NMR (100 MHz, $CDCl_3$) δ 167.27, 154.24, 152.76, 150.20, 147.66, 146.55, 146.33, 144.38, 143.53, 142.47, 132.97, 127.70, 122.29, 104.57, 33.00, 31.96, 29.34, 29.20, 25.58, 22.81, 16.37, 15.65, 14.25, 0.44. HR-MS (FD) Calcd for $C_{68}H_{98}Ge_2N_4S_7Si_2$: $[M]^+$: 1398.37930, Found: 1398.37938.

References

[1] Main group strategies towards functional hybrid materials. T. Baumgartner, T.; Jäkle, F. John Wiley & Sons. **2018**.

- [2] Salzner, U.; Lagowski, J. B.; Pickup, P. G.; Poirier, R. A. *Synth. Met.* **1998**, *96*, 177-189.
- [3] Ohshita, J. *Macromol. Chem. Phys.* **2009**, *210*, 1360-1370.
- [4] Zhang, Z.; Zhu, X. *J. Mater. Chem. A* **2018**, *6*, 4266-4270.
- [5] Zając, D.; Honisz, D.; Łapkowski, M.; Sołoducho, J. *Molecules* **2019**, *24*, 2259.
- [6] Cai, Y.; Qin, A.; Tang, B. Z. *J. Mater. Chem. C* **2017**, *5*, 7375-7389.
- [7] Zhao, J.; Qiu, D.; Shi, J.; Wang, H. *J. Org. Chem* **2012**, *77*, 2929-2934.
- [8] Liu, L.; Song, J.; Lu, H.; Wang, H.; Bo, Z. *Polym. Chem.* **2016**, *7*, 319-329.
- [9] Li, M.; Liu, L.; Zhao, C.; Zhou, Y.; Guo, Y.; Song, J.; Wang, H. *Dyes Pigm.* **2016**, *134*, 480-486.
- [10] Guo, X.; Zhou, N.; Lou, S. J.; Hennek, J. W.; Ponce Ortiz, R.; Butler, M. R.; Marks, T. J. *J. Am. Chem. Soc.* **2012**, *134*, 18427-18439.
- [11] Amb, C. M.; Chen, S.; Graham, K. R.; Subbiah, J.; Small, C. E.; So, F.; Reynolds, J. R. *J. Am. Chem. Soc.* **2011**, *133*, 10062-10065.
- [12] Ohshita, J.; Hwang, Y. M.; Mizumo, T.; Yoshida, H.; Ooyama, Y.; Harima, Y.; Kunugi, Y. *Organometallics* **2011**, *30*, 3233-3236.
- [13] Adachi, Y.; Nabeya, T.; Nomura, T.; Kondo, K.; Kawakami, K.; Ooyama, Y.; Ohshita, J. *Dalton Trans.* **2019**, *48*, 16671-16678.
- [14] Adachi, Y.; Ooyama, Y.; Shibayama, N.; Ohshita, J. *Dalton Trans.* **2016**, *45*, 13817-13826.
- [15] Ohshita, J.; Sugino, M.; Ooyama, Y.; Adachi, Y. *Organometallics* **2019**, *38*, 1606-1613.
- [16] Wang, C. H.; Adachi, Y.; Ohshita, J. *Molecules* **2024**, *29*, 2684.
- [17] Pham, N. N.; Parpart, S.; Grigoryan, S.; Ngo, T. N.; Dang, T. T.; Ghochikyan, T. V.; Langer, P. *Eur. J. Org. Chem.* **2017**, *2017*, 538-550.
- [18] Ding, L.; Wang, Z. Y.; Yao, Z. F.; Liu, N. F.; Wang, X. Y.; Zhou, Y. Y.; Pei, J. *Macromolecules* **2021**, *54*, 5815-5824.
- [19] Lin, Y.; Jiang, C.; Hu, F.; Yin, J.; Yu, G. A.; Liu, S. H. *Dyes Pigm.* **2013**, *99*, 995-1003.
- [20] Yabusaki, Y.; Ohshima, N.; Kondo, H.; Kusamoto, T.; Yamanoi, Y.; Nishihara, H.

Chem. Eur. J **2010**, *19*, 5581-5585.

[21] Ohshita, J.; Nakamura, M.; Ooyama, Y. *Organometallics* **2015**, *34*, 5609-5614.

[22] Lee, K. H.; Ohshita, J.; Tanaka, D.; Tominaga, Y.; Kunai, A. *J. Organomet. Chem.* **2012**, *710*, 53-58.

[23] Barłóg, M.; Zhang, X.; Kulai, I.; Yang, D. S.; Sredojevic, D. N.; Sil, A.; Ji, X.; Salih, K. S. M.; Bazzi, H. S.; Bronstein, H.; Fang, L.; Kim, J.; Marks, T. J.; Guo, X.; Al-Hashimi, M. *Chem. Mater.* **2019**, *31*, 9488-9496.

[24] Sun, W.; Adachi, Y.; Ohshita, J. *Dyes Pigm.* **2022**, *203*, 110333.

[25] Ong, K. H.; Lim, S. L.; Tan, H. S.; Wong, H. K.; Li, J.; Ma, Z.; Chen, Z. K. *Adv. Mater.* **2011**, *11*, 1409-1413.

[26] Cao, Y.; Lei, T.; Yuan, J.; Wang, J. Y.; Pei, J. *Polym. Chem.* **2013**, *4*, 5228-5236.

[27] Frisch, M. J.; Trucks, G. W.; Schlegel, H. B.; Scuseria, G. E.; Robb, M. A.; Cheeseman, J. R.; Scalmani, G.; Barone, V.; Petersson, G. A.; Nakatsuji, H.; Li, X.; Caricato, M.; Marenich, A. V.; Bloino, J.; Janesko, B. G.; Gomperts, R.; Mennucci, B.; Hratchian, H. P.; Ortiz, J. V.; Izmaylov, A. F.; Sonnenberg, J. L.; Williams-Young, D.; Ding, F.; Lipparini, F.; Egidi, F.; Goings, J.; Peng, B.; Petrone, A.; Henderson, T.; Ranasinghe, D.; Zakrzewski, V. G.; Gao, J.; Rega, N.; Zheng, G.; Liang, W.; Hada, M.; Ehara, M.; Toyota, K.; Fukuda, R.; Hasegawa, J.; Ishida, M.; Nakajima, T.; Honda, Y.; Kitao, O.; Nakai, H.; Vreven, T.; Throssell, K.; Montgomery, J. A., Jr.; Peralta, J. E.; Ogliaro, F.; Bearpark, M. J.; Heyd, J. J.; Brothers, E. N.; Kudin, K. N.; Staroverov, V. N.; Keith, T. A.; Kobayashi, R.; Normand, J.; Raghavachari, K.; Rendell, A. P.; Burant, J. C.; Iyengar, S. S.; Tomasi, J.; Cossi, M.; Millam, J. M.; Klene, M.; Adamo, C.; Cammi, R.; Ochterski, J. W.; Martin, R. L.; Morokuma, K.; Farkas, O.; Foresman, J. B.; Fox, D. J. Gaussian 16, revision C.01; Gaussian, Inc.: Wallingford, CT, 2019.

[28] Foresman, J. B.; Frisch, A. *Exploring Chemistry with Electronic Structure Methods*, 3rd ed.; Gaussian, Inc.: Wallingford, CT, USA, **2015**.

Conclusions

Throughout this work, the author synthesized new conjugated compounds based on new ideas of molecular design. By introducing non-covalent interaction such as $\text{Bi}\cdots\text{O}$, the author succeeded in fine control of the molecular planarity of bibenzofuran, thereby indicating their potential application as device materials. The author also developed triazolgermole compounds for the first time. The introduction of triphenylamine substituent to triazolgermole provided a D-A conjugated compound that showed chromic properties, suggesting potential applications of the triazolgermole derivatives as sensor materials. In addition, the author synthesized new unsymmetrical benzothienogermole and dithienogermole and indicated their application for preparing new D-A materials.

In Chapter 1, the author successfully synthesized bismuth-, antimony-, and arsenic-substituted bibenzofurans and bibenzothiophenes. The single crystal X-ray diffraction study revealed the presence of attractive intramolecular noncovalent $\text{Bi}\cdots\text{O}$, $\text{Sb}\cdots\text{O}$, and $\text{As}\cdots\text{O}$ interactions, which enhanced the self-planarization and rigidification of the π -conjugated systems. According to theoretical calculations including QTAIM analysis, BCPs were found between $\text{Bi}\cdots\text{O}$, $\text{Sb}\cdots\text{O}$, and $\text{As}\cdots\text{O}$, corresponding to the van der Waals interactions as revealed by IRI. The experimental data and the DFT calculations revealed that the HOMO and LUMO energy levels of bismuth- and antimony-substituted bibenzofurans and bibenzothiophenes were lower than those reported previously for phosphorous substituted bibenzofuran, reflecting the stronger noncovalent interactions. In addition, the absorption spectra were red-shifted as a result of enhanced conjugation due to the higher planarity owing to these interactions. Such interactions as $\text{Bi}\cdots\text{O}$, $\text{Sb}\cdots\text{O}$, and $\text{As}\cdots\text{O}$ are anticipated to generally operate in other cyclic ether systems. It may be possible that bismuth, antimony, and arsenic substituents on other cyclic ether-based π -conjugated systems provide both intermolecular and intramolecular interactions, making potential structural control possible in the solid state, and ultimately, improving the device performance. The author has not yet examined the device fabrication based on these substituted bibenzofurans. However, the good film forming property of bismuth-

substituted bibenzofuran indicated its potential application as a device material.

In Chapter 2, the author synthesized triazolgermole compounds for the first time and thoroughly investigated their optical and electrochemical behaviors to elucidate the electronic states. The author's findings suggest that replacing the condensed benzene ring of benzotriazolgermole with a thiophene ring enhances the conjugation, as evidenced by the red-shifted absorption of thienotriazolgermole relative to that of benzotriazolgermole. Contrary to the author's expectation, germole condensation raised both HOMO and LUMO energy levels, suggesting that the $\sigma^*-\pi^*$ conjugation does not play an important role in the triazolgermole system and that the germole unit serves as an electron donor, unlike conventional germole compounds such as dithienogermoles and dibenzogermoles. The author also found that bromo-substituted thienotriazolgermole can be used as a potential precursor of a variety of thienotriazolgermole-based conjugated compounds, and an electron-donating triphenylamine unit was introduced to the thiophene ring of thienotriazolgermole. The resulting triphenylamine-thienotriazolgermole showed the expected intramolecular D–A interaction, indicating that the triphenylamine unit can be used as an electron-accepting unit in conjugated D–A systems. Furthermore, triphenylamine-thienotriazolgermole had sufficient Lewis basicity for complex formation with trifluoroethanol, inducing a clear red shift of the PL band, suggesting potential applications of triazolgermole derivatives as sensor materials. The triazolgermole seems to be useful as an acceptor unit being applicable to donor–acceptor compounds.

In Chapter 3, the author has successfully synthesized new unsymmetrically condensed benzothienogermole and dithieno[3,2-*b*:4,5-*c'*]germole. These unsymmetrical germoles were thoroughly investigated with respect to their optical and electrochemical properties and DFT calculations and it was found that replacing the benzene ring in benzothienogermole with a thiophene ring can change the electronic states enhancing the conjugation in unsymmetrical dithienogermole derivatives. The author also explored the potential application of unsymmetrical dithienogermole as the donor unit of D-A conjugated materials by forming D-A oligomers. The D-A oligomers thus obtained exhibited extended conjugation and clear

solvatochromic properties arising from their intramolecular D-A interaction. These results clearly indicate the potential applications of the dithieno[3,2-*b*:4,5-*c'*]germole unit as an electron donor of D-A systems.

List of Publications

Chapter 1.

Group 15 Element (As, Sb, Bi)-substituted Bibenzofurans with Noncovalent Conformational Locks for Enhanced Planarity.

Cong-Huan Wang, Akifumi Sumida, Yohei Adachi, Hiroaki Imoto, Kensuke Naka, and Joji Ohshita*

Organometallics, **2024**, 2(23), 3397-3404.

Chapter 2.

Synthesis of Unsymmetrically Condensed Benzo- and Thienotriazolgermoles.

Cong-Huan Wang, Yohei Adachi, and Joji Ohshita*

Molecules, **2024**, 29(11), 2684.

Chapter 3.

Preparation of Dithieno[3,2-*b*:4,5-*c'*]germole and Its Application as a Donor Unit in Conjugated D-A Compounds.

Cong-Huan Wang, Yohei Adachi, and Joji Ohshita*

Molecules, in press

Other papers not included in this thesis

Ultrathin nanosheet-assembled nickel-based metal–organic framework microflowers for supercapacitor applications.

Cong-Huan Wang, Da-Wei Zhang, Shude Liu, Yusuke Yamauchi, Fei-Bao Zhang and Yusuf Valentino Kaneti

Chemical Communications, **2022**, 58(7), 1009-1012.

P=O noncovalent conformational locks for constructing highly planar Bis (diphenylphosphanyl) Bi(benzofurano).

Cong-Huan Wang, Zhan-Chen Gao, Weipeng Sun, Xugang Guo, Fei-Bao Zhang

Dyes and Pigments, **2021**, 184, 108820.

Progress on Silicone Resins modified by Polyhedral Oligomeric Silsesquioxane.

Cong-Huan Wang, Su-Fang Lv, Jian-Xiong Jiang, Lian-Bin Wu, Fei-Bao Zhang

Silicone Material, **2021**,35(1), 66-70.

Bis(benzofurano)pyrrole and Hybrid thienopyrrole Derivatives for Organic Thin-Film Transistors

Weipeng Sun, **Cong-Huan Wang**, Su-Fang Lv, Jian-Xiong Jiang, Xugang Guo and Fei-Bao Zhang

Organic Electronics, 2020, 105548.

Acknowledgements

This thesis is a summary of my studies from 2021 to 2024 under the direction of Professor Joji Ohshita at Hiroshima University.

I wish to extend my heartfelt appreciation to Professor Joji Ohshita, my supervisor, for granting me the invaluable opportunity to pursue a Ph.D. in his research group and for providing me with valuable guidance and unwavering support. I also would like to thank Assistant Professor Yohei Adachi and Dr. Weipeng Sun for their useful advice and help. Furthermore, I am grateful to a scholarship from the China Scholarship Council (CSC) to support my living expenses.

I would like to thank, Mr. Kohei Yamada, Mr. Lin Zhixin, Mr. Kosuke Tsutsui, Mr. Shota Terao, Mr. Ryuji Matsuura, Mr. Ryuto Miyazaki, Mr. Toshiki Kaneko, Ms. Kanaka Sasaki, Mr. Yuto Hattori, Mr. Kazuki Hara, Mr. Atsuya Ota, Mr. Hiroki Tobita, Mr. Tetsunosuke Nara, Mr. Takuma Matsumaru for their kindness and collaboration.